

LIGHT SCATTERING PROBLEM AND ITS APPLICATION  
IN ATMOSPHERIC SCIENCE

A Thesis  
by  
ZHAOKAI MENG

Submitted to the Office of Graduate Studies of  
Texas A&M University  
in partial fulfillment of the requirements for the degree of  
MASTER OF SCIENCE

December 2010

Major Subject: Physics

LIGHT SCATTERING PROBLEM AND ITS APPLICATION  
IN ATMOSPHERIC SCIENCE

A Thesis  
by  
ZHAOKAI MENG

Submitted to the Office of Graduate Studies of  
Texas A&M University  
in partial fulfillment of the requirements for the degree of  
MASTER OF SCIENCE

Approved by:

Co-Chairs of Committee:	George W. Kattawar Ping Yang
Committee Member, Department Head,	Edward Fry Edward Fry

December 2010

Major Subject: Physics

## ABSTRACT

Light Scattering Problem and its Application in Atmospheric Science.

(December 2010)

Zhaokai Meng, B.S., Wuhan University

Co-Chairs of Advisory Committee: Dr. George W. Kattawar  
Dr. Ping Yang

The light scattering problem and its application in atmospheric science is studied in this thesis. In the first part of this thesis, light scattering theory of single irregular particles is investigated. We first introduce the basic concepts of the light scattering problem. T-matrix ansatz, as well as the null-field technique, are introduced in the following sections. Three geometries, including sphere, cylinder and hexagonal column, are defined subsequently. Corresponding light scattering properties (i.e., T-matrix and Mueller Matrix) of those models with arbitrary sizes are simulated via the T-matrix method.

In order to improve the efficiency for the algorithms of single-light scattering, we present a user-friendly database software package of the single-scattering properties of individual dust-like aerosol particles. The second part of this thesis describes this database in detail. Its application to radiative transfer calculations in a spectral region from ultraviolet (UV) to far-infrared (far-IR) is introduced as well. To expand the degree of morphological freedom of the commonly used spheroidal and spherical models, tri-axial ellipsoids were assumed to be the overall shape of dust-like aerosol particles. The software package allows for the derivation of the bulk optical properties for a given

distribution of particle microphysical parameters (i.e., refractive index, size parameter and two aspect ratios). The array-oriented single-scattering property data sets are stored in the NetCDF format.

The third part of this thesis examines the applicability of the tri-axial ellipsoidal dust model. In this part, the newly built database is equipped in the study. The pre-computed optical properties of tri-axial models are imported to a polarized adding-doubling radiative transfer (RT) model. The radiative transfer property of a well-defined atmosphere layer is consequently simulated. Furthermore, several trial retrieval procedures are taken based on a combination of intensity and polarization in the results of RT simulation. The retrieval results show a high precision and indicate a further application in realistic studies.



## ACKNOWLEDGEMENTS

First of all, I thank Dr. George W. Kattawar. His comprehensive knowledge and innovative ideas constantly guided my research in the last two years. Besides, he also encouraged me to apply my knowledge into real life. The natural phenomenon and rules have never been so clear to me.

I would like to thank Dr. Ping Yang. He is my co-advisor in the last two years. He has led me into such a wonderful area. Many of my research ideas originated from his suggestions.

I would like to thank Dr. Torsten Siebert, one of my committee members. His suggestions helped me a lot. I would like to thank Dr. Edward S. Fry, for his substitution of Dr. Siebert's position in my defense. Dr. Fry for his suggestions also benefited me.

I would like to thank Mr. Lei Bi, Dr. Yu You, Mr. Xin Huang, Mr. Meng Gao, Mr. Benjamin Stryker, Dr. Yu Xie, Dr. Qian Feng, Mr. Yue Li, Mr. Guanglin Tang, Dr. Shouguo Ding, Mr. Bingqi Yi, Mr. Kai Lv and all other members in my group. Working with this group was a memorable experience. Thank you for sharing your ideas and experiences.

I would like to thank all my good friends, Yang Liu, Wei Zhao, Jialiang Wang and many others. They have brought me a joyful life in College Station.

Finally, I would like to thank my family, my parents and grandparents. Their love and support enabled me to finish my studies and obtain this degree.

## TABLE OF CONTENTS

	Page
ABSTRACT.....	iii
ACKNOWLEDGEMENTS.....	v
TABLE OF CONTENTS.....	vi
LIST OF TABLES.....	viii
LIST OF FIGURES.....	ix
 CHAPTER	
I INTRODUCTION AND BACKGROUND.....	1
A Radiative Transfer Equation.....	1
B Light Scattering Theory.....	5
C Radiative Transfer Equation with Polarization.....	11
II THE T-MATRIX TREATMENT FOR SINGLE-SCATTERING PROBLEMS.....	13
A Introduction to Light Scattering Problems.....	13
B The T-matrix Ansatz.....	17
C The Null-field Method on Solving T-matrix.....	21
D Results and Discussion.....	26
E Summary.....	33
III A DATABASE FOR OPTICAL PROPERTIES OF NONSPHERICAL MINERAL DUST AEROSOLS.....	34
A Introduction.....	34
B Dust Particle Model.....	37
C Computational Methods.....	42
D Database Design and User Interface.....	44
E Results and Discussion.....	49
F Summary.....	59
IV RADIATIVE TRANSFER (RT) APPLICATION OF NONSPHERICAL AEROSOL MODELS.....	60
A Introduction.....	60

CHAPTER	Page
B Model Selection and Methodology .....	61
C Results and Discussion .....	66
D Summary .....	84
V CONCLUSION.....	85
REFERENCES .....	86
VITA .....	94

## LIST OF TABLES

TABLE	Page
1 The selected aspect ratios and refractive indices for the present scattering simulations .....	41
2 The size parameters selected for simulations. Blank cells indicate that simulations were not conducted for the computation method.....	41

## LIST OF FIGURES

FIGURE		Page
1	Geometric configuration of radiative transfer over a thin atmosphere layer .....	3
2	Illustration of a classical light scattering problem. ....	6
3	Polarization configuration of scattering problem. ....	7
4	Scattering plane $OP_1P_2$ with respect to the meridian plane $OP_1Z$ and $OP_2Z$ .....	12
5	Illustration of the boundary condition problem.....	16
6	The light scattering problem .....	23
7	The light scattering problem with a null-field inside the particle and equivalent currents on the particle surface .....	23
8	The light scattering problem after nullification of the internal field and removal of the external sources .....	23
9	Geometries selected in this study .....	27
10	Q matrices and T-matrix of a spherical particle with size parameter equals to 7. ....	29
11	Q matrices and T-matrix of a cylinder particle with size parameter equals to 7.....	29
12	Q matrices and T-matrix of a hexagonal column with size parameter equals to 7.....	30
13	Geometry for light scattering problems shown in Fig. 14 and 15. ....	31
14	Phase function (P11) in (a) and P12 in (b) for a hexagonal column with size parameter $kL=20$ and aspect ratio $L/2a=1.0$ . The geometry is shown in Fig. 13.....	31
15	Phase function (P11) in (a) and P12 in (b) for a hexagonal column with size parameter $kL=30$ and aspect ratio $L/2a=1.0$ . The geometry is shown in Fig. 13.....	31
16	Geometry for light scattering problems shown in Fig. 17 and 18. ....	32

FIGURE	Page
17	Phase function (P11) in (a) and P12 in (b) for a hexagonal column with size parameter $kL=20$ and aspect ratio $L/2a=1.0$ . The geometry is shown in Fig. 16..... 32
18	Phase function (P11) in (a) and P12 in (b) for a hexagonal column with size parameter $kL=30$ and aspect ratio $L/2a=1.0$ . The geometry is shown in Fig. 13. .... 32
19	The geometry of a tri-axial ellipsoid..... 38
20	The morphology of ellipsoids in 2-D aspect-ratio space. .... 39
21	Complex refractive indices of dust and the simulation domain (the area between two dashed lines). .... 40
22	The basic logic flow of this database..... 46
23	The structure of a single NetCDF file..... 48
24	Comparison of the six elements of the phase matrix computed from the T-matrix and the ADDA. The size parameter used is $x=26$ . The axis ratio is given by $a:b:c=0.48:1:1$ . The complex refractive index $m$ is $1.5+0.1i$ . .... 49
25	Comparison of the six elements of the phase matrix computed from the T-matrix and the ADDA. The size parameter used is $x=26$ . The axis ratio is given by $a:b:c=0.48:1:1$ . The complex refractive index $m$ is $1.5+0.0005i$ ..... 50
26	Comparison of the phase matrix computed from the ADDA and the IGOM..... 51
27	Comparison of the six elements in the phase matrix computed from the ADDA and the IGOM. .... 53
28	Comparison between interpolated and simulation results. The two aspect ratios are $\epsilon_{c/a}=0.40$ , $\epsilon_{c/b}=0.64$ . The complex refractive index is $m=1.55+i0.0916$ and size parameter is 21..... 53
29	Comparison between interpolated and simulation results. The two aspect ratios are $\epsilon_{c/a}=0.40$ and $\epsilon_{c/b}=0.64$ . The complex refractive index $m$ is $1.53+i0.008$ and size parameter is 21..... 54
30	Extinction efficiency $Q_{\text{ext}}$ , single-scattering albedo $\omega$ and asymmetry factor $g$ as functions of size parameter for various shapes at two refractive indices. .... 54

FIGURE	Page
31	Extinction efficiency $Q_{\text{ext}}$ , single-scattering albedo $\omega$ and asymmetry factor $g$ as functions of the incident wavelength. ....56
32	Contours of the extinction efficiency, single-scattering albedo and asymmetry factor of three ellipsoidal models as functions of wavelength and maximum particle dimension .....56
33	Comparison between the measured phase matrix (Volten et al. 2006) and the simulated phase matrix for an ensemble of ellipsoids and for sampled Feldspar aerosols at a wavelength of $0.6328 \mu\text{m}$ . ....58
34	The configuration of the atmosphere layer, incident beam, ground surface and aerosol particles considered in this study .....62
35	Geometry of coated tri-axial ellipsoidal particles .....64
36	The Mueller matrix of a tri-axial ellipsoidal model.....67
37	The reflectance Stokes vector of an atmosphere layer illuminated by a beam. ....69
38	Similar as Fig. 37 except a tri-axial ellipsoid model is applied .....69
39	Similar as Fig. 37 except the aerosol optical thickness is set as 0.5 .....70
40	Similar as Fig. 38 except the aerosol optical thickness is set as 0.5.....70
41	The Stokes parameter of the reflectance of an atmosphere layer versus the aerosol optical thickness and the effective radius of the aerosol model. ....72
42	Similar as Fig. 40, except the viewing angle has $\phi-\phi_0=-60^\circ$ .....72
43	Similar as Fig. 40, except the viewing angle has $\phi-\phi_0=60^\circ$ .....73
44	Similar as Fig. 40, except the viewing angle has $\phi-\phi_0=120^\circ$ .....73
45	Modeling of aerosol optical thickness and effective radius retrievals using both intensity and polarization criteria. Four standard models with $\tau=0.2$ and $r_{\text{eff}}=(a) 0.3\mu\text{m}$ (b) $0.5\mu\text{m}$ (c) $0.7\mu\text{m}$ and (d) $0.9\mu\text{m}$ . The aerosol refractive index is assumed to be known beforehand ( $m=1.53+i0.008$ ). The illumination and viewing geometry are specified as $\mu_0=0.8$ , $\mu=0.6$ and $\phi-\phi_0=0^\circ$ . ....76
46	Similar as Fig. 44 except for $\phi-\phi_0=60^\circ$ .....76

FIGURE	Page
47	The Stokes parameter of the reflectance of an atmosphere layer versus the aerosol optical thickness and refractive index (real part) of the aerosol model. The incident zenith angle is $\mu_0=0.8$ , the viewing angle is $\mu=0.6$ and $\phi-\phi_0=0^\circ$ .....77
48	Similar as Fig. 46, except the viewing angle has $\phi-\phi_0=120^\circ$ . ....78
49	Modeling of aerosol optical thickness and refractive index (real part) retrievals using both intensity and polarization criteria.....78
50	Similar as Fig. 48 except for $\phi-\phi_0=60^\circ$ .....79
51	Similar as Fig. 48 except for aerosol optical thickness of standard models $\tau=0.4$ .....79
52	The Stokes parameter of the reflectance of an atmosphere layer versus the aerosol optical thickness and refractive index (real part) of the aerosol model. ....80
53	Similar as Fig. 51 except for $\phi-\phi_0=120^\circ$ .....80
54	Modeling of aerosol optical thickness and refractive index (imaginary part) retrievals using both intensity and polarization criteria. ....81
55	Similar as Fig. 53 except for $\phi-\phi_0=120^\circ$ .....81
56	The relation between effective refractive index and the volume fraction of the inclusion.....82
57	The Stokes parameter of the reflectance of an atmosphere layer versus the aerosol optical thickness and volume fraction of the inclusion in the aerosol model.....83



## CHAPTER I

### INTRODUCTION AND BACKGROUND

The earth's atmosphere contains various types of particulates including aerosols, water droplets, ice crystals and hailstones (Liou, 2002). Those atmospheric particulates, especially aerosols and cloud particles, play an important role in impacting earth's climate system, both directly and indirectly (Chylek & Coakley, 1974; Chuang et al., 2003; Ramanathan et al., 2001). However, the quantitative knowledge of the radiative impact of the particulate is poorly known. This is partly due to their uncertain physical properties. The physical properties, including the morphology and constitution of the particles, are fundamental to quantifying the radiative forcing of the particulates. For this reason, numerous laboratory and *in situ* studies are carried out to study the physical properties of the atmospheric particulates (e.g., Munoz et al., 2004, 2006; Nousiainen et al., 2006; Warren et al., 1994; Volten et al., 2001). Although those studies brought favorable results, they are lack of generality and a global coverage. Recently, remote-sensing techniques are widely applied in atmosphere description. The corresponding retrieval techniques are invented to extract useful information from satellite or ground based observations (e.g., Dubovik et al., 2004, 2006). The remote-sensing observations are aimed to collect the atmospheric radiance that contains the information of the particulates. Radiative Transfer (RT) models (e.g., Discrete-Ordinates Method (DISORT, Stamnes et al., 1988) and Adding-Doubling Method (de Hann et al., 1987)) play an

---

The journal model is *Journal of Aerosol Science*.

important role in the retrieval procedure. Previous studies have substantially enriched the knowledge on the optical properties of the various models for dust-like aerosols. Further investigation of their impact on the Radiative Transfer (RT) properties is presented in this chapter. A polarized adding-doubling RT model (de Hann et al., 1987) is applied to simulate the atmospheric radiance and polarization configuration observed by the satellite. Various model size, morphology, composition and inhomogeneity are applied in the RT model.

## A. RADIATIVE TRANSFER EQUATION

The radiative transfer theory studies the processes of the electromagnetic radiation in medium. The analysis of a radiation field often requires us to consider the amount of the radiant energy. The specific intensity, or the radiance, is defined as the radiant energy crosses area  $dA$ , confined in the solid angle  $d\Omega$ , and oriented to the angle  $\theta$  to the normal direction of  $dA$ , in the time interval  $dt$ , and wavelength interval  $d\lambda$ .

$$I_{\lambda} = \frac{dE_{\lambda}}{\cos\theta d\Omega d\lambda dt dA}$$

In this thesis, we consider the monochromatic field only. The radiance is a space invariant if no extinction emerged during the transfer process. It is independent from the distance between the radiative source and the detector. For example, if a point source is considered, the energy  $E$  passing through unit area with a distance  $r$  away from the source is inversely proportional to  $r^2$ . However, the solid angle  $\Omega$  extended by the unit

area to the radiative source is inversely proportional to  $r^2$ , either. Thus the quantity  $\frac{E}{\Omega}$  that is proportional to the radiance is a constant under this situation.

The flux density is subsequently defined by integrating radiance over a solid angle:

$$F_\lambda = \int_{\Omega} I_\lambda \cos \theta d\Omega$$

The physical meaning of flux density is the monochromatic power that has been received or radiated by a unit area. The flux density is also called as “irradiance” if the considered area is receiving energy. If the area is a radiative source, flux density is usually called as “radiative emittance” instead. Therefore, “irradiance” is only used when talking about the detector (instrument receiving power, or energy). Different from radiance, the irradiance is not a constant over the space even there is no extinction procedures during radiative transfer. For the point source, the power received by a detector with unit area (as the definition of irradiance) is inversely proportional to  $r^2$ .

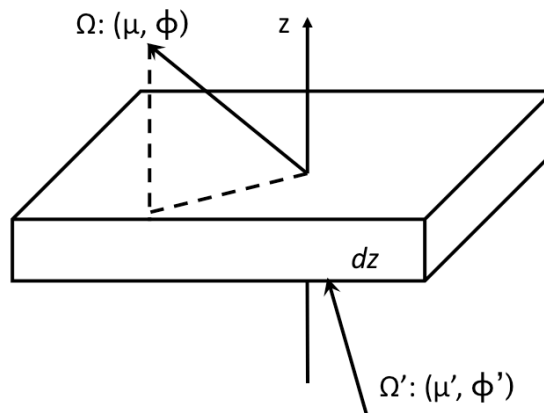


**Fig. 1** Geometric configuration of radiative transfer over a thin atmosphere layer.

If extinction emerges during the radiative transfer, the radiance varies according to the following rule:

$$dI_\lambda = -I_\lambda \beta_e ds + j_\lambda \beta_e ds$$

where

$$ds = dz / \mu.$$

Corresponding geometry configuration is shown in Fig. 1. The first term denotes the radiance weakened by the medium.  $\beta_\lambda$  is the extinction coefficient with definition:

$$\beta_e = \int_{\Delta s} \sigma_e(s) n(s) ds / \Delta s$$

which represents the total extinction cross section in a unit length. This expression follows the Bouguer-Lambert-Beer's law.  $j_\lambda$  is a phenomenological term which represents the emittance ability of the medium. The atmospheric emittance may due to scattering and thermal emission. In this thesis we consider radiance in visible spectrum only. The thermal emission is negligible in this spectrum regime. The atmosphere can thus be regarded as a scattering atmosphere.

Define phase function  $P(\Omega, \Omega')$  represents the ability of the medium to redirect the energy from solid angle  $\Omega'$  to solid angle  $\Omega$ . If we integrate over the all the incoming directions, factor  $\beta_\lambda j_\lambda$  can be expressed as:

$$\beta_\lambda j_\lambda = \frac{\beta_s}{4\pi} \int P(\Omega, \Omega') I(z, \Omega') d\Omega'$$

Therefore, the equation of radiative transfer can be written as:

$$\frac{dI(s, \Omega)}{-\beta_e ds} = I(z, \Omega) - \frac{1}{4\pi} \frac{\beta_s}{\beta_e} \int P(\Omega, \Omega') I(z, \Omega') d\Omega'$$

Define optical thickness  $d\tau = -\beta_e ds$ , scattering albedo  $\omega = \frac{\beta_s}{\beta_e}$  and  $\mu$  is the cosine of

the zenith angle for outgoing wave. We can further simplify RT equation:

$$\mu \frac{dI(\tau, \Omega)}{d\tau} = I(\tau, \Omega) - \frac{\omega}{4\pi} \int P(\Omega, \Omega') I(\tau, \Omega') d\Omega' \quad (1.1)$$

Here optical thickness takes place of the distance. Giving appropriate boundary conditions and source function can solve this differential-integral equation.

## B. LIGHT SCATTERING THEORY

The phase function as defined in Eqn. 1.1 is mainly due to the light scattering effects of the particulates in the medium. The light scattering theory is aimed to solve the phase function for given scatterers. Fig. 2 shows a classical light scattering problem. The incident field (i.e., its incident direction, frequency, intensity and polarization state) and the physical properties of the particle (i.e., its morphology, size and optical constants such as the electric permittivity and the magnetic permeability) are given. The scattered field is the unknown quantity. The electric component and the magnetic component are interdependent for free electromagnetic fields. Thus only one of them needs to be calculated. Conventionally, people choose the electric field. In this thesis we choose  $\mathbf{E}^{inc}$  to denote the electric component of the incident fields, and  $\mathbf{E}^{sca}$  for the counterpart of the scattered field. The two fields are linked by a scattering amplitude tensor  $\mathbf{A}$  (Doicu et al., 2006):

$$\mathbf{E}^{sca}(\hat{e}_r) \Big|_{r \rightarrow \infty} = \frac{e^{ikr}}{kr} \mathbf{A}(\hat{e}_r, \hat{e}_k) \cdot \mathbf{E}^{inc}(\hat{e}_k)$$

Here  $\hat{e}_k$  and  $\hat{e}_r$  are the unit vectors along the direction of the incident beam and the scattered beam, respectively. The condition  $r \rightarrow \infty$  is added since only the scattered wave at far-field region is interested. Note that in the far-field region, the amplitude of the scattered field weakens with the factor  $\frac{1}{kr}$  due to the spherical wave assumption.

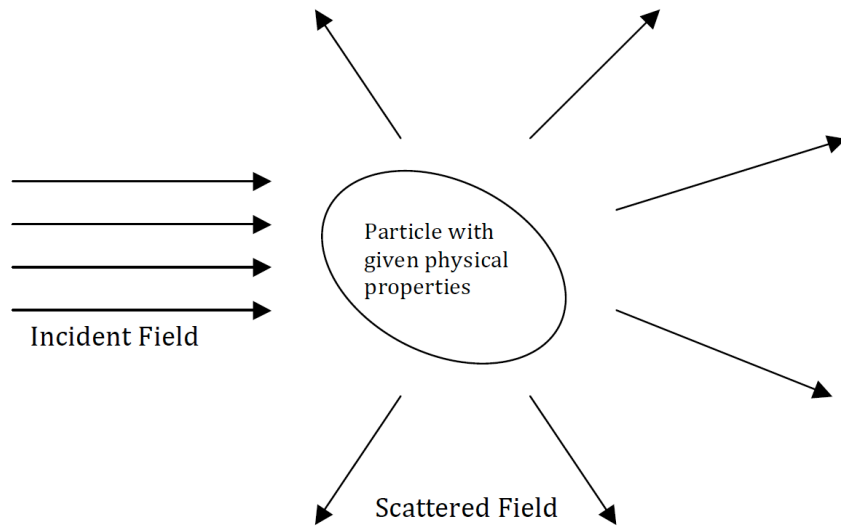


**Fig. 2** Illustration of a classical light scattering problem. In this problem, the incident field and the physical properties of the particle are given, and the scattered field is unknown.

The scattering tensor can be expressed as a matrix if we represent the incident and scattered field in a vector form. For example, if we choose basis vector  $\hat{e}_\alpha$  and  $\hat{e}_\beta$  for the incident field (i.e.,  $\mathbf{E}^{inc} = E_\alpha^{inc} \hat{e}_\alpha + E_\beta^{inc} \hat{e}_\beta$ ), and  $\hat{e}_\theta$  and  $\hat{e}_\phi$  for the scattered field (i.e.,  $\mathbf{E}^{sca} = E_\theta^{sca} \hat{e}_\theta + E_\phi^{sca} \hat{e}_\phi$ ), then the amplitude matrix is given by:

$$\begin{bmatrix} E_\theta^{sca} \\ E_\phi^{sca} \end{bmatrix}_{r \rightarrow \infty} = \frac{e^{ikr}}{kr} \mathbf{S}(\hat{e}_r, \hat{e}_k) \begin{bmatrix} E_\alpha^{inc} \\ E_\beta^{inc} \end{bmatrix} = \frac{e^{ikr}}{kr} \begin{bmatrix} S_{\theta\beta} & S_{\theta\alpha} \\ S_{\phi\beta} & S_{\phi\alpha} \end{bmatrix} \begin{bmatrix} E_\beta^{inc} \\ E_\alpha^{inc} \end{bmatrix}$$

with components in the matrix  $\mathbf{S}$  are expressed as follows:

$$\begin{aligned} S_{\theta\beta} &= \hat{e}_\theta \cdot \mathbf{A} \cdot \hat{e}_\beta, & S_{\theta\alpha} &= \hat{e}_\theta \cdot \mathbf{A} \cdot \hat{e}_\alpha, \\ S_{\phi\beta} &= \hat{e}_\phi \cdot \mathbf{A} \cdot \hat{e}_\beta, & S_{\phi\alpha} &= \hat{e}_\phi \cdot \mathbf{A} \cdot \hat{e}_\alpha. \end{aligned}$$

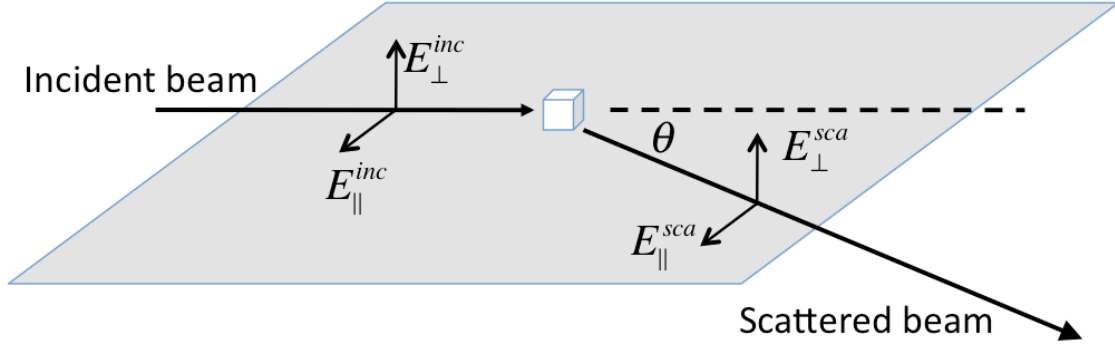


**Fig. 3** Polarization configuration of scattering problem.

Conventionally, the scatter plane is selected as the reference plane for decomposing electric fields of the incident and scattered beams. The scattered plane is determined by the incident and scattered beams, as shown in Fig. 3. Therefore the fields can be decomposed as  $\mathbf{E}^{inc} = E_{\parallel}^{inc} \hat{e}_{\parallel}^{inc} + E_{\perp}^{inc} \hat{e}_{\perp}$  for incident beam and  $\mathbf{E}^{sca} = E_{\parallel}^{sca} \hat{e}_{\parallel}^{sca} + E_{\perp}^{sca} \hat{e}_{\perp}$  for scattered beam. The unit vector  $\hat{e}_{\perp}$  is the same for both expressions. The corresponding amplitude matrix can be written as:

$$\begin{bmatrix} E_{\perp}^{sca} \\ E_{\parallel}^{sca} \end{bmatrix}_{r \rightarrow \infty} = \frac{e^{ikr}}{kr} \begin{bmatrix} S_2 & S_3 \\ S_4 & S_1 \end{bmatrix} \begin{bmatrix} E_{\perp}^{inc} \\ E_{\parallel}^{inc} \end{bmatrix}$$

Following the convention of van der Hulst (1953) and Chandrasekhar (1950), the Stokes Vectors are selected to describe the polarization state of the light beams. The Stokes vector contains four parameters defined as follow:

$$I = \langle E_\alpha E_\alpha^* + E_\beta E_\beta^* \rangle$$

$$Q = \langle E_\alpha E_\alpha^* - E_\beta E_\beta^* \rangle$$

$$U = \langle E_\alpha E_\beta^* + E_\beta E_\alpha^* \rangle$$

$$V = \langle i(E_\alpha E_\beta^* - E_\beta E_\alpha^*) \rangle$$

if the electric component of this field can be expressed as  $\mathbf{E} = E_\alpha \hat{e}_\alpha + E_\beta \hat{e}_\beta$ . Here both  $E_\alpha$  and  $E_\beta$  are complex, oscillating functions with a definite frequency.  $E_\alpha^*$  denotes the complex conjugate of function  $E_\alpha$ .  $\langle \dots \rangle$  denotes the temporal average. The Stokes vector is defined as  $(I, Q, U, V)$  (van der Hulst, 1953). Since the electric field is a function of the detector location, the Stokes Vector is a function dependent on the location, either. The component “I” is proportional with the power radiated on a unit area centered at the point where the field is measured. Note that due to the spherical wave assumption of the scattered wave, the “I” component is inversely proportional with  $k^2 r^2$ . Here  $r$  refers to the distance between the source and the detector. The Stokes parameters have the unit of irradiance.

Transformation matrix  $\mathbf{F}$  links the Stokes vectors of the incident and the scattered fields:

$$(I, Q, U, V) = \frac{1}{k^2 r^2} \mathbf{F} \cdot (I_0, Q_0, U_0, V_0)$$

where  $(I, Q, U, V)$  is the Stokes vector of the scattered field, and  $(I_0, Q_0, U_0, V_0)$  is for the incident field. The phase matrix is tight related with the amplitude matrix. The explicit expression reads as:



$$\begin{aligned}
F_{11} &= \frac{1}{2} \left( |S_{\theta\beta}|^2 + |S_{\theta\alpha}|^2 + |S_{\phi\beta}|^2 + |S_{\phi\alpha}|^2 \right) & F_{12} &= \frac{1}{2} \left( |S_{\theta\beta}|^2 - |S_{\theta\alpha}|^2 + |S_{\phi\beta}|^2 - |S_{\phi\alpha}|^2 \right) \\
F_{13} &= -\operatorname{Re} \left\{ S_{\theta\beta} S_{\theta\alpha}^* + S_{\phi\alpha} S_{\phi\beta}^* \right\} & F_{14} &= -\operatorname{Im} \left\{ S_{\theta\beta} S_{\theta\alpha}^* - S_{\phi\alpha} S_{\phi\beta}^* \right\} \\
F_{21} &= \frac{1}{2} \left( |S_{\theta\beta}|^2 + |S_{\theta\alpha}|^2 - |S_{\phi\beta}|^2 - |S_{\phi\alpha}|^2 \right) & F_{22} &= \frac{1}{2} \left( |S_{\theta\beta}|^2 - |S_{\theta\alpha}|^2 - |S_{\phi\beta}|^2 + |S_{\phi\alpha}|^2 \right) \\
F_{23} &= -\operatorname{Re} \left\{ S_{\theta\beta} S_{\theta\alpha}^* - S_{\phi\alpha} S_{\phi\beta}^* \right\} & F_{24} &= -\operatorname{Im} \left\{ S_{\theta\beta} S_{\theta\alpha}^* + S_{\phi\alpha} S_{\phi\beta}^* \right\} \\
F_{31} &= -\operatorname{Re} \left\{ S_{\theta\beta} S_{\phi\beta}^* + S_{\phi\alpha} S_{\theta\alpha}^* \right\} & F_{32} &= -\operatorname{Re} \left\{ S_{\theta\beta} S_{\phi\beta}^* - S_{\phi\alpha} S_{\theta\alpha}^* \right\} \\
F_{33} &= \operatorname{Re} \left\{ S_{\theta\beta} S_{\phi\alpha}^* + S_{\theta\alpha} S_{\phi\beta}^* \right\} & F_{34} &= \operatorname{Im} \left\{ S_{\theta\beta} S_{\phi\alpha}^* + S_{\theta\alpha} S_{\phi\beta}^* \right\} \\
F_{41} &= -\operatorname{Im} \left\{ S_{\phi\beta} S_{\theta\beta}^* + S_{\phi\alpha} S_{\theta\alpha}^* \right\} & F_{42} &= -\operatorname{Im} \left\{ S_{\phi\beta} S_{\theta\beta}^* - S_{\phi\alpha} S_{\theta\alpha}^* \right\} \\
F_{43} &= \operatorname{Im} \left\{ S_{\phi\alpha} S_{\theta\beta}^* - S_{\theta\alpha} S_{\phi\beta}^* \right\} & F_{44} &= \operatorname{Re} \left\{ S_{\phi\alpha} S_{\theta\beta}^* - S_{\theta\alpha} S_{\phi\beta}^* \right\}
\end{aligned}$$

If the incident beam is natural light with unit intensity, the power being scattered can be written as:

$$\frac{dE_{sca}}{dt} = \int_{4\pi} \frac{1}{k^2 r^2} F_{11}(\Omega) r^2 d\Omega$$

Here a sphere centered at the particle, and with radius  $r$  is used to receive the power. On the other hand,  $\frac{dE_{sca}}{dt}$  is the power being illuminated on area  $\frac{dE_{sca}}{dt}$  by the incident beam (with unit intensity). Area  $\frac{dE_{sca}}{dt}$  is called as scattering cross section later, and is denoted as  $\sigma_{sca}$  in the rest part of this thesis.

Conventionally, the transformation matrix is normalized according to the rule:

$$\frac{C}{4\pi} \int_{4\pi} F_{11}(\Omega) d\Omega = 1$$

here  $C$  is a normalization constant. According to the definition of scattering cross section, we have:

$$C = \frac{4\pi}{\sigma_{sca} k^2}$$

and

$$\frac{\sigma_{sca}}{4\pi r^2} \mathbf{P} = \frac{1}{k^2 r^2} \mathbf{F}$$

Here  $\mathbf{P}$  is the normalized transformation matrix, or called as “phase matrix”.

Formula

$$(I, Q, U, V) = \frac{\sigma_{sca}}{4\pi r^2} \mathbf{P} \cdot (I_0, Q_0, U_0, V_0) \quad (1.2)$$

represents the relation of the irradiance (as well as polarization) on the particle and detector. The irradiance of the incident beam on the particle is received and transformed into the scattered field by the scattering procedure. The irradiance of the scattered field is received by a detector located in the far-field region. If we put  $1/r^2$  in the left hand side:

$$\frac{(I, Q, U, V)}{1/r^2} = \frac{\sigma_{sca}}{4\pi} \mathbf{P} \cdot (I_0, Q_0, U_0, V_0)$$

The physical meaning is clearer than before. The left-hand side of this equation is the radiance of the particle radiation. The Stokes vector in the right-hand side is the irradiance on the particle. The operator  $\frac{\sigma_{sca}}{4\pi} \mathbf{P}$  transforms the irradiance on the particle to the radiance of the scattering radiation.

According to the light scattering studies in previous discussions,  $\frac{\sigma_{sca}}{4\pi} \mathbf{P}_{11}(\Omega, \Omega')$  represents the ability of a particle to redirect the energy from solid angle  $\Omega'$  to solid angle  $\Omega$ . Term  $\frac{\sigma_{sca}}{4\pi} P(\Omega, \Omega') I(s, \Omega') d\Omega'$  represents the radiance being radiated by the particle due to the (on particle) irradiance  $I(s, \Omega') d\Omega'$ . Therefore,  $\mathbf{P}_{11}(\Omega, \Omega')$  is the phase

function as shown in Eqn. 1.1. Note that the medium contains a set of different particulates, thus the phase function in Eqn. (1.1) is actually an averaged effect.

### C. RADIATIVE TRANSFER EQUATION WITH POLARIZATION

Following Liou (2002), the scalar quantities in Eqn. 1.1 can be replaced by its vector counterpart:

$$\mu \frac{d\mathbf{I}(\tau, \Omega)}{d\tau} = \mathbf{I}(\tau, \Omega) - \frac{\omega}{4\pi} \int \mathbf{Z}(\Omega, \Omega') \mathbf{I}(\tau, \Omega') d\Omega'$$

Here  $\mathbf{I}$  is the Stokes vector in its radiance version. The previous discussions show that Stokes parameters have unit of irradiance. However, the equation of radiative transfer requires  $\mathbf{I}$  to be in the unit of radiance. For spherical waves, the Stokes parameters have to be multiplied by  $r^2$  in order to get its radiance.

The reference planes for Stokes parameters are selected as their local meridians for both incoming and outgoing waves (planes  $OP_1Z$  and  $OP_2Z$  in Fig. 4). The scattering plane  $OP_1P_2$  have angle  $i_1$  and  $i_2$  respect to plane  $OP_1Z$  and  $OP_2Z$ , respectively. Thus, the relation between  $\mathbf{Z}(\Omega, \Omega')$  and the phase matrix can be written as:

$$\mathbf{Z}(\Omega, \Omega') = \mathbf{L}(\pi - i_2) \mathbf{P}(\Theta) \mathbf{L}(-i_1)$$

where

$$\mathbf{L}(\chi) = \begin{pmatrix} 1 & 0 & 0 & 0 \\ 0 & \cos 2\chi & \sin 2\chi & 0 \\ 0 & -\sin 2\chi & \cos 2\chi & 0 \\ 0 & 0 & 0 & 1 \end{pmatrix}$$

denotes the rotation of Stokes vector.  $\mathbf{P}(\Theta)$  is the phase matrix as derived in Eqn. 1.2.

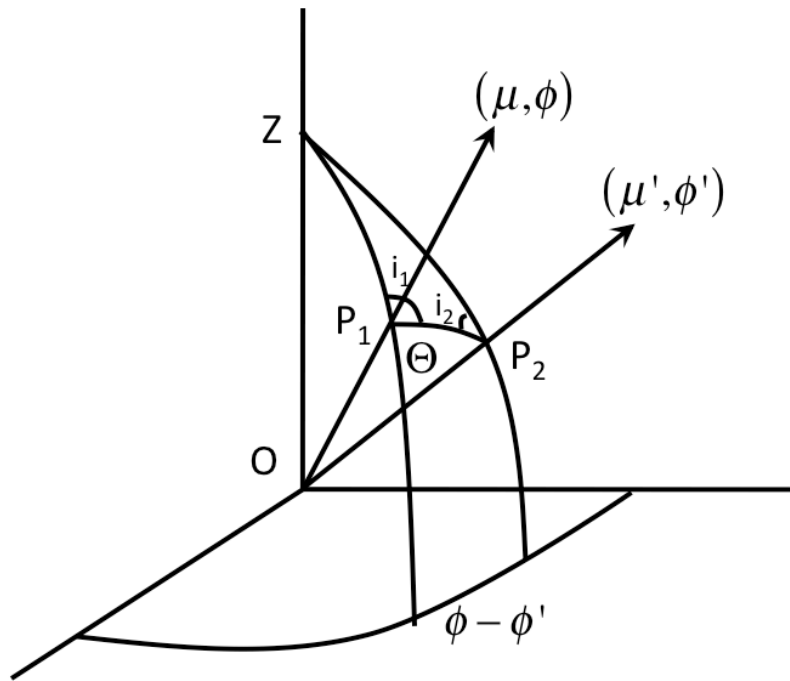


**Fig. 4** Scattering plane  $OP_1P_2$  with respect to the meridian plane  $OP_1Z$  and  $OP_2Z$ .

## CHAPTER II

### THE T-MATRIX TREATMENT FOR SINGLE-SCATTERING PROBLEMS

#### A. INTRODUCTION TO LIGHT SCATTERING PROBLEMS

Light scattering theory is critical in variety disciplines, including atmospheric science, astrophysics, applied physics and optics, as well as various engineering disciplines. The theory is aimed to derive the scattered field, including the intensity and state of polarization, for a characterized particle under a given beam. Since the pioneer paper by Mie (1908), light scattering problems has been consistently investigated for nearly one century. Mie was interested in the scattering properties of suspensions of noble metal spheres. However, most particles encountered in light scattering problems nowadays are no longer simple. They can be nonspherical, inhomogeneous, coated or even anisotropic. Correspondingly, various techniques, including Discrete Dipole Approximation (DDA, Purcell and Pennypacker, 1973), Finite Difference Time Domain (FDTD, Yee, 1966), T-matrix Method (Waterman, 1965) and Geometric Optics Method (GOM, Yang and Liou, 1996), were developed to solve the problem in both numerical and analytical ways. Most of those methods are based on solving the Maxwell's equations, which governs the light scattering procedure.

The light scattering theory is aimed to derive the relation between the incident field and the scattered field (e.g., the scattering amplitude matrix and phase matrix as

aforementioned) based on the given conditions and the basic rules that govern the electromagnetic fields (i.e., Maxwell's equations). The applications of Maxwell's equations are discussed in the following paragraphs.

Equations 2.1 show the Maxwell equations that govern the behavior of light scattering procedure. The behavior of macroscopic field at interior points in the media reads as:

$$\begin{aligned}\nabla \times \mathbf{E} &= i\omega\mathbf{B}, & \nabla \times \mathbf{H} &= \mathbf{J} - i\omega\mathbf{D}, \\ \nabla \cdot \mathbf{D} &= \rho, & \nabla \cdot \mathbf{B} &= 0.\end{aligned}\quad (2.1)$$

Here  $t$  is the time,  $\mathbf{E}$  is the electric field,  $\mathbf{H}$  is the magnetic field,  $\mathbf{B}$  is the magnetic induction,  $\mathbf{D}$  is the electric displacement,  $\rho$  and  $\mathbf{J}$  are the electric charge density and current density, respectively. All the fields are assumed as time harmonic. For example, with  $\omega$  being the angular frequency and  $i = \sqrt{-1}$ , the electric field can be expressed as:

$$\mathbf{E}(\mathbf{r}, t) = \text{Re}\{\mathbf{E}(\mathbf{r})\exp(-i\omega t)\}$$

In this study, we will focus on the "free" media, which implies that there are no free charge and current in the particle. Thus,  $\rho$  and  $\mathbf{J}$  can be both set as 0.

The magnetic induction  $\mathbf{B}$  and the electric displacement  $\mathbf{D}$  can be linked with the vector fields  $\mathbf{E}$  and  $\mathbf{H}$ , with the given characteristics of the media. For isotropic media, the relations read as:

$$\mathbf{D} = \varepsilon\mathbf{E}, \quad \mathbf{B} = \mu\mathbf{H}.$$

Here  $\varepsilon$  and  $\mu$  are the electric permittivity and the magnetic permeability of the media, respectively. Both  $\varepsilon$  and  $\mu$  are scalars.  $\varepsilon$  and  $\mu$  can be tensors in case the media is anisotropic. However, we will focus on the isotropic media in this study so that the

electric permittivity and the magnetic permeability are both treated as scalars throughout this thesis. Furthermore, the magnetic permeability is close to 1 for most paramagnetic materials. For regular particles involved in the light scattering problems, we can make the simplification  $\mu = 1$  without inducing much error.

The Maxwell's equations can be thus simplified with the aforementioned relations and simplifications:

$$\begin{aligned}\nabla \times \mathbf{E} &= i\omega\mathbf{H}, & \nabla \times \mathbf{H} &= -i\omega\epsilon\mathbf{E}, \\ \nabla \cdot \mathbf{E} &= 0, & \nabla \cdot \mathbf{H} &= 0.\end{aligned}\quad (2.2)$$

The latter two equations are redundant since we can make gradient of the former two equations:

$$\nabla \cdot (\nabla \times \mathbf{E}) = i\omega(\nabla \cdot \mathbf{H}) = 0, \quad \nabla \cdot (\nabla \times \mathbf{H}) = -i\omega\epsilon(\nabla \cdot \mathbf{E}) = 0,$$

and thus derive the relations  $\nabla \cdot \mathbf{E} = 0$  and  $\nabla \cdot \mathbf{H} = 0$ . Therefore we can take only the former two equations into our consideration. A more symmetric form can be derived by taking curl of the both sides of those two equations:

$$\nabla \times \nabla \times \mathbf{E} = \omega^2\epsilon\mathbf{E}, \quad \nabla \times \nabla \times \mathbf{H} = \omega^2\epsilon\mathbf{H}. \quad (2.3)$$

Therefore the equation governing the electric field is absolute the same as its counterpart of the magnetic field.

The similar equations can be derived via the same procedure. The corresponding equations read as:

$$\nabla \times \nabla \times \mathbf{E} = \omega^2\epsilon_0\mathbf{E}, \quad \nabla \times \nabla \times \mathbf{H} = \omega^2\epsilon_0\mathbf{H} \quad (2.4)$$

Eqns. 2.4 are almost the same as Eqns. 2.3 except the electric permittivity  $\epsilon$  is replaced by  $\epsilon_0$ , which is of the air (or the vacuum).

Since the electromagnetic fields inside and outside the particle obey different equations, it is necessary to treat them separately. In this thesis, the fields inside the

particle are called as internal fields with a superscript “int”, and the fields outside the particle are named as external fields with a superscript “ext”. The boundary conditions link internal and external fields.

Fig. 5 shows a general interface between two mediums. In this circumstances, the boundary conditions read as:

$$\begin{aligned}\mathbf{n}_1 \times (\mathbf{E}_2 - \mathbf{E}_1) &= 0 \\ \mathbf{n}_1 \times (\mathbf{H}_2 - \mathbf{H}_1) &= \mathbf{J}_s\end{aligned}\quad (2.5)$$

Here  $\mathbf{E}_1$  and  $\mathbf{H}_1$  are fields in medium 1,  $\mathbf{E}_2$  and  $\mathbf{H}_2$  are fields in medium 2,  $\mathbf{J}_s$  is the surface electric current on the interface of medium 1 and 2, and  $\mathbf{n}_1$  is the normal vector of the surface pointing into medium 2. Equations 2.5 give the relationship between the fields in two mediums. Note that the surface magnetic current, which has not been discovered in the real world, has not been considered in Eqn. 2.5. However, the magnetic current is sometimes a powerful tool in light scattering theory. The boundary conditions read as:

$$\begin{aligned}\mathbf{n}_1 \times (\mathbf{E}_2 - \mathbf{E}_1) &= \mathbf{M}_s \\ \mathbf{n}_1 \times (\mathbf{H}_2 - \mathbf{H}_1) &= \mathbf{J}_s\end{aligned}\quad (2.6)$$

if the surface magnetic current is taken into consideration. Here  $\mathbf{M}_s$  is the surface magnetic current.

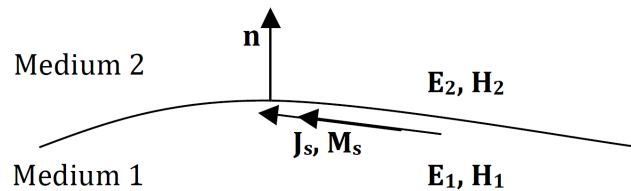


**Fig. 5** Illustration of the boundary condition problem. The curve refers to the interface between medium 1 and 2.  $\mathbf{E}_1$ ,  $\mathbf{E}_2$ ,  $\mathbf{H}_1$ ,  $\mathbf{H}_2$  are corresponding electromagnetic fields, and  $\mathbf{J}_s$ ,  $\mathbf{M}_s$  are the surface electric and magnetic currents, respectively.



## B. THE T-MATRIX ANSATZ

The equations employed in describing the light scattering problems have the form:

$$\nabla \times \nabla \times \mathbf{X} - k^2 \mathbf{X} = 0 \quad (2.7)$$

Here  $\mathbf{X}$  stands for the electric field  $\mathbf{E}$  or the magnetic field  $\mathbf{H}$ .  $k$  is the wave number and has the relation  $k = \omega\sqrt{\epsilon}$  as in eqns. 2.3. If we define the refractive index of the media as  $m = \sqrt{\epsilon / \epsilon_0}$ , then we have  $k = k_0 m$  where  $k_0 = \omega\sqrt{\epsilon_0}$ .

In the spherical coordinate system, the solutions of equation 1.7 can be expressed as a superposition of a set of “vector spherical wave functions”. The regular vector spherical wave functions are defined as:

$$\begin{aligned} \text{Rg}\mathbf{M}_{mn}(kr, \theta, \phi) &= \frac{1}{\sqrt{2n(n+1)}} j_n(kr) \left( \frac{im}{\sin\theta} P_n^m(\cos\theta) \hat{\theta} - \frac{dP_n^m(\cos\theta)}{d\theta} \hat{\phi} \right) e^{im\phi} \\ \text{Rg}\mathbf{N}_{mn}(kr, \theta, \phi) &= \sqrt{\frac{n(n+1)}{2}} \frac{j_n(kr)}{kr} P_n^m(\cos\theta) e^{im\phi} \hat{r} \\ &\quad + \frac{1}{\sqrt{2n(n+1)}} \frac{(krj_n(kr))'}{kr} \left( \frac{dP_n^m(\cos\theta)}{d\theta} \hat{\theta} + \frac{im}{\sin\theta} P_n^m(\cos\theta) \hat{\phi} \right) e^{im\phi} \end{aligned}$$

Here function  $j_n(kr)$  is regular spherical Bessel function,  $P_n^m(\cos\theta)$  is the normalized associated Legendre function.

Irregular vector spherical wave functions are defined in a similar way except the regular spherical Bessel function  $j_n(kr)$  is replaced by spherical Hankel function of the first kind  $h_n^{(1)}(kr)$ . Correspondingly, the irregular wave functions are noted as  $\mathbf{M}_{mn}(kr, \theta, \phi)$  and  $\mathbf{N}_{mn}(kr, \theta, \phi)$ , with a removal of the prefix “Rg”.  $h_n^{(1)}(kr)$  goes to

infinity at origin (i.e.,  $r=0$ ), thus it is called as “irregular”. On the contrary, regular vector wave functions have finite value at the origin.

According to their definition, the vector spherical wave functions have relationship:

$$(Rg)\mathbf{N}_{mn}(kr, \theta, \phi) = \frac{1}{k} \nabla \times (Rg)\mathbf{M}_{mn}(kr, \theta, \phi).$$

Additionally, all the vector spherical wave functions, regardless of their subscripts, satisfy the equation 2.7. Furthermore, Morse et al. (1953) proved the completeness of the set of the vector spherical wave functions. It implies that regular and irregular spherical wave functions can be equipped as sets of base functions to describe the electromagnetic fields that satisfy equation 2.7.

There are three electromagnetic fields involved in the light scattering problems, including the incident field, scattered field and the internal field inside the particle. The external field is a combination of the incident field and the scattered field. Both the internal field and the external field are governed by the Maxwell’s equation in free media (i.e., eqn. 2.7). Furthermore, the incident field obeys eqn. 2.7, either, cause it can exist regardless of the existence of the particle. Thus the scattered field has to satisfy eqn. 2.7. However, the source of the scattered field exist inside of the particle, which resulted the field goes to infinity when approaching to the origin. Therefore the scattered field can only be expanded by the irregular base functions.

The incident and scattered fields can be expanded by vector spherical wave functions after aforementioned discussion:

$$\vec{E}^{inc}(\vec{r}) = \sum_{m,n} \left[ a_{mn}^{i(M)} Rg\mathbf{M}_{mn}(kr, \theta, \phi) + a_{mn}^{i(N)} Rg\mathbf{N}_{mn}(kr, \theta, \phi) \right]$$

$$\vec{E}^{sca}(\vec{r}) = \sum_{m,n} \left[ a_{mn}^{s(M)} \mathbf{M}_{mn}(kr, \theta, \phi) + a_{mn}^{s(N)} \mathbf{N}_{mn}(kr, \theta, \phi) \right]$$

Here  $a_{mn}^{i(M)}$ ,  $a_{mn}^{i(N)}$ ,  $a_{mn}^{s(M)}$  and  $a_{mn}^{s(N)}$  are expansion coefficients. The coefficients  $a_{mn}^{i(M)}$  and  $a_{mn}^{i(N)}$  can be derived based on the given incident field. For example, for plane wave incident,

$$a_{mn}^{i(M)} = \frac{-4i^n}{\sqrt{2n(n+1)}} \hat{e}_{pol} \cdot \left[ im\hat{e}_\theta \frac{P_n^m(\cos\theta_0)}{\sin\theta_0} + \hat{e}_\phi \frac{d}{d\theta} P_n^m(\cos\theta) \Big|_{\theta=\theta_0} \right] e^{-im\phi_0}$$

$$a_{mn}^{i(N)} = \frac{-4i^{n+1}}{\sqrt{2n(n+1)}} \hat{e}_{pol} \cdot \left[ \frac{d}{d\theta} P_n^m(\cos\theta) \Big|_{\theta=\theta_0} \hat{e}_\theta - im\hat{e}_\phi \frac{P_n^m(\cos\theta_0)}{\sin\theta_0} \right] e^{-im\phi_0}$$

Here  $\hat{e}_{pol}$  is the unit vector along the polarization direction of the incident field,  $\theta_0$  and  $\phi_0$  correspond to the incident direction. The coefficients  $a_{mn}^{s(M)}$  and  $a_{mn}^{s(N)}$  of the scattered field are unknown. The aim of the light scattering problem is to derive these coefficients.

The T-matrix Ansatz states the relation between the expansion coefficients of the incident field and the scattered field. The T-matrix Ansatz reads as:

$$a_{mn}^{s(M)} = \sum_{m'n'} \left[ T_{mnm'n'}^{(11)} a_{m'n'}^{i(M)} + T_{mnm'n'}^{(12)} a_{m'n'}^{i(N)} \right], \text{ and}$$

$$a_{mn}^{s(N)} = \sum_{m'n'} \left[ T_{mnm'n'}^{(21)} a_{m'n'}^{i(M)} + T_{mnm'n'}^{(22)} a_{m'n'}^{i(N)} \right].$$

The ansatz gives a linear relationship between two coefficient sets. The existence of this linear relationship is “postulated” by the T-matrix Ansatz and is a consequence of the linearity of the Maxwell’s equations. The above-mentioned relation can be written in a compact form if we choose a combined index  $l = n(n+1) + m$ . Thus,  $l$  has a maximum

$L_{\max} = N_{\max}(N_{\max} + 2)$ . Here  $N_{\max}$  is the largest value of  $n$  considered in the problem.

Hence, letting  $\vec{a}^{s(M)}$  and  $\vec{a}^{s(N)}$  denotes column arrays  $a_i^{s(M)}$  and  $a_i^{s(N)}$ , and  $\vec{a}^{i(M)}$  and  $\vec{a}^{i(N)}$  denotes column arrays  $a_i^{i(M)}$  and  $a_i^{i(N)}$ , respectively, we have the matrix relation:

$$\begin{bmatrix} \vec{a}^{s(M)} \\ \vec{a}^{s(N)} \end{bmatrix} = \begin{bmatrix} \vec{T}^{(11)} & \vec{T}^{(12)} \\ \vec{T}^{(21)} & \vec{T}^{(22)} \end{bmatrix} \begin{bmatrix} \vec{a}^{i(M)} \\ \vec{a}^{i(N)} \end{bmatrix} \quad (2.8)$$

where  $\vec{T}^{(11)}$ ,  $\vec{T}^{(12)}$ ,  $\vec{T}^{(21)}$  and  $\vec{T}^{(22)}$  are matrices of dimension  $L_{\max} \times L_{\max}$  representing the T-matrix coefficients  $T_{ll'}^{(11)}$ ,  $T_{ll'}^{(12)}$ ,  $T_{ll'}^{(21)}$  and  $T_{ll'}^{(22)}$ , respectively.

The T-matrix is a powerful tool as it completely solves the light scattering problem once it is derived. For example, the elements of the amplitude matrix is given by

$$\begin{aligned} S_{pq}(\hat{e}_r, \hat{e}_k) = & \frac{4}{k} \sum_{n,m} \sum_{n',m'} (-i)^{n+1} i^{m_1} \{ [T_{mm_1n_1}^{11} m_{m_1n_1,q}^*(\hat{e}_k) \\ & - iT_{mm_1n_1}^{12} n_{m_1n_1,q}^*(\hat{e}_k)] m_{mn,p}(\hat{e}_r) \\ & + i[T_{mm_1n_1}^{21} m_{m_1n_1,q}^*(\hat{e}_k) \\ & - iT_{mm_1n_1}^{22} n_{m_1n_1,q}^*(\hat{e}_k)] n_{mn,p}(\hat{e}_r) \} \end{aligned}$$

Here  $p = \theta, \phi$  and  $q = \beta, \alpha$ , and functions  $m$  and  $n$  are defined as:

$$\begin{aligned} m_{mn}(\theta, \phi) &= \frac{1}{\sqrt{2n(n+1)}} \left[ im \frac{P_n^m(\cos\theta)}{\sin\theta} \hat{e}_\theta - \frac{d}{d\theta} P_n^m(\cos\theta) \hat{e}_\phi \right] e^{im\phi} \\ n_{mn}(\theta, \phi) &= \frac{1}{\sqrt{2n(n+1)}} \left[ \frac{d}{d\theta} P_n^m(\cos\theta) \hat{e}_\theta + im \frac{P_n^m(\cos\theta)}{\sin\theta} \hat{e}_\phi \right] e^{im\phi}. \end{aligned}$$

Correspondingly, the phase matrix can be derived from the amplitude matrix.

### C. THE NULL-FIELD METHOD ON SOLVING T-MATRIX

Null-field method is the standard scheme for T-matrix computation. The null-field method is introduced by Waterman (1965) as a technique for solving electromagnetic scattering by perfectly conducting particles. Later Bates (1968) extended the theory to dielectrics (Waterman, 1969a, 1971) and to acoustic studies (Waterman, 1969b). The null-field has been later extended to multiple scattering problems and multilayered and composite particles (Peterson et al., 1974, 1975). Recently, the null-field method is widely applied in the electromagnetic, acoustic and elastodynamic scattering by single and aggregated particles (Mishchenko et al., 2000, 2002; Tsang et al., 1985, 2000).

Fig. 6 shows a classical light scattering problem. The electric permittivity and magnetic permeability are denoted as  $\mu_0, \epsilon_0$  outside the particle and  $\mu, \epsilon$  inside the particle, respectively. Following previous discussion, the incident and scattered fields are denoted as  $\mathbf{E}^{inc}, \mathbf{H}^{inc}$  and  $\mathbf{E}^{sca}, \mathbf{H}^{sca}$ , respectively. The internal fields are denoted as  $\mathbf{E}^{int}, \mathbf{H}^{int}$ . The notations  $\mathbf{J}_i, \mathbf{M}_i$  refer to the source that induced the incident field.  $\mathbf{J}_i, \mathbf{M}_i$  should be far away from the particle. The outward unit normal vector of the particle surface is denoted as  $\hat{n}$ . The letter  $S$  stands for the surface of the particle, which is given beforehand.

The first step of the null-field method is to nullify the internal field of the particle. The goal can be achieved by applying the equivalence theorem. The theorem states that, as far as the external fields are concerned, the internal field can be effectively replaced by a set of surface currents over  $S$  without affecting the overall fields in the external region.

The equivalence current can be expressed in term of the tangential component of the surface fields.

$$\begin{aligned}\mathbf{J}_+ &= \hat{n} \times \mathbf{H}_+ \\ \mathbf{M}_+ &= \mathbf{E}_+ \times \hat{n}\end{aligned}$$

Here  $\mathbf{J}_+$  and  $\mathbf{M}_+$  refer to the equivalent electric and magnetic surface current, respectively. The magnetic current is resulted by magnetic monopoles, which is imaginary tool assisting us to solve the problem more conveniently. The free magnetic monopoles have not been discovered in our real world yet. Fig. 7 shows the situation when internal field is nullified.

The second step of the null-field method is to remove the source of the incident field from the system (i.e.,  $\mathbf{J}_i, \mathbf{M}_i$ ). This operation results a pure incident field with a negative sign to appear inside the particle, and a pure scattered field in the external region.

Fig. 8 shows the situation after the two-steps operation aforementioned.  $\mathbf{J}_+$  and  $\mathbf{M}_+$  become the only sources in this situation. Both internal and external fields can be regarded as induced by  $\mathbf{J}_+$  and  $\mathbf{M}_+$ . The relation of the source and the field can be built up via the dyadic Green's function (Barber, 1975; Morse, 1953):

$$\left. \begin{array}{l} \text{outside } S: \quad \mathbf{E}^{sca} \\ \text{inside } S: \quad -\mathbf{E}^{inc} \end{array} \right\} = -\nabla \times \int_S \mathbf{M}_+ \cdot \vec{G}(kR) dS - \nabla \times \nabla \times \int_S \frac{1}{i\omega\epsilon_0} \mathbf{J}_+ \cdot \vec{G}(kR) dS \quad (2.9)$$

Here  $\vec{G}(kR)$  is the dyadic Green's function with the definition

$$\vec{G}(kR) = \left( \vec{I} + \frac{1}{k_s} \nabla \nabla \right) \frac{\exp(ikR)}{4\pi R}, \text{ and } R = |\mathbf{r} - \mathbf{r}'|, \text{ where } \mathbf{r} \text{ and } \mathbf{r}' \text{ are position vectors}$$

with field  $-\mathbf{E}^{inc}$ . However, we need to know that it is just a technique for T-matrix

solving. The internal field is NOT  $-\mathbf{E}^{inc}$  but being represented by the surface current instead. Since only the tangential component of the internal field affects the external

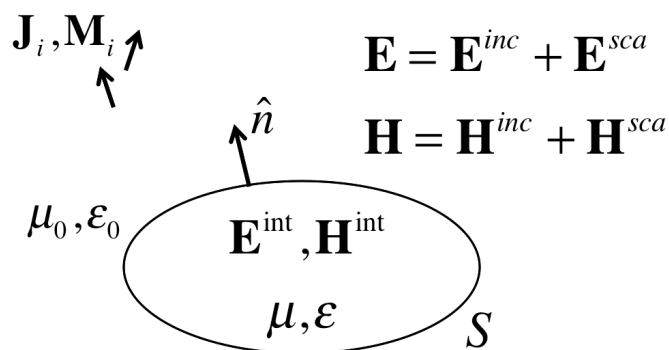


**Fig. 6** The light scattering problem

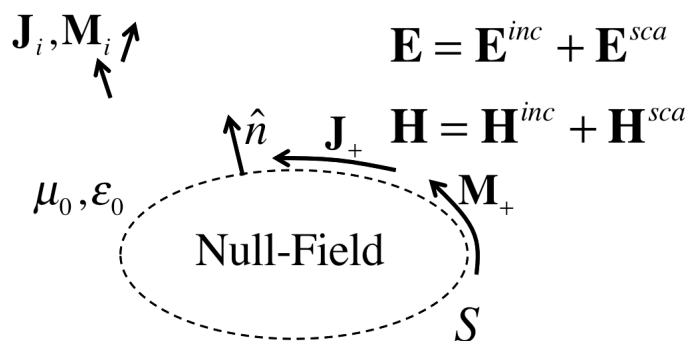


**Fig. 7** The light scattering problem with a null-field inside the particle and equivalent currents on the particle surface.

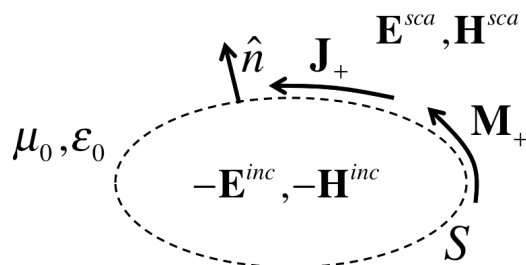


**Fig. 8** The light scattering problem after nullification of the internal field and removal of the external sources.

from an interior origin to source and field points, respectively. The dyadic Green's function is a second order tensor. The internal region of the particle is now totally filled fields, the equivalent surface current is an adequate representation. Further T-matrix investigations of the internal field can be found in Doicu et al (2006) based on a recursive method. Additionally, finite difference time domain and discrete dipole approximation can both give the internal field of a particle. However, in atmosphere science, the internal fields do not attract too much interest. We restrict ourselves in the external fields in the following studies in this thesis.

Eqn. 2.8 contains two parts: inside  $S$  (the internal case) and outside  $S$  (the external case). It should be noted that the so-called "internal case" is a consequence of the nullification procedure, and thus is not related internal field in as shown in Fig. 6. The internal region is now occupied by  $-\mathbf{E}^{inc}$  and  $-\mathbf{H}^{inc}$ . Using the vector spherical wave functions introduced in Section 2.2, the incident field is given by:

$$\vec{E}^{inc}(\vec{r}) = \sum_{m,n} \left[ a_{mn}^{i(M)} Rg\mathbf{M}_{mn}(kr, \theta, \phi) + a_{mn}^{i(N)} Rg\mathbf{N}_{mn}(kr, \theta, \phi) \right]$$

Furthermore, the Green's function, as well as the surface fields, can be expanded in terms of the same base functions (Morse, 1953):

$$\vec{G}_0(\vec{r}, \vec{r}') = ik \sum_{mn} (-1)^m \begin{cases} \mathbf{M}_{-mn}(kr, \theta, \phi) Rg\mathbf{M}_{mn}(kr', \theta', \phi') \\ \quad + \mathbf{N}_{-mn}(kr, \theta, \phi) Rg\mathbf{N}_{mn}(kr', \theta', \phi') & \text{for } r' < r \\ Rg\mathbf{M}_{-mn}(kr, \theta, \phi) \mathbf{M}_{mn}(kr', \theta', \phi') \\ \quad + Rg\mathbf{N}_{-mn}(kr, \theta, \phi) \mathbf{N}_{mn}(kr', \theta', \phi') & \text{for } r' > r \end{cases}$$

and

$$\hat{n} \times \mathbf{E}_+ = \sum_{m,n} \left[ c_{m,n} \hat{n} \times Rg\mathbf{M}_{m,n}(k_s r, \theta, \phi) + d_{m,n} \hat{n} \times Rg\mathbf{N}_{m,n}(k r, \theta, \phi) \right]$$



$$\hat{n} \times \mathbf{H}_+ = \sum_{m,n} \left[ d_{m,n} \hat{n} \times \text{RgM}_{m,n}(k_s r, \theta, \phi) + c_{m,n} \hat{n} \times \text{RgN}_{m,n}(k_s r, \theta, \phi) \right]$$

Therefore, if we define the quantities:

$$\begin{aligned} P_{mmm'n'} &= -ikk_s J_{mmm'n'}^{(21)} - ik^2 J_{mmm'n'}^{(12)} \\ R_{mmm'n'} &= -ikk_s J_{mmm'n'}^{(11)} - ik^2 J_{mmm'n'}^{(22)} \\ S_{mmm'n'} &= -ikk_s J_{mmm'n'}^{(22)} - ik^2 J_{mmm'n'}^{(11)} \\ U_{mmm'n'} &= -ikk_s J_{mmm'n'}^{(12)} - ik^2 J_{mmm'n'}^{(21)} \end{aligned}$$

and

$$\begin{aligned} \text{Rg}P_{mmm'n'} &= -ikk_s \text{Rg}J_{mmm'n'}^{(21)} - ik^2 \text{Rg}J_{mmm'n'}^{(12)} \\ \text{Rg}R_{mmm'n'} &= -ikk_s \text{Rg}J_{mmm'n'}^{(11)} - ik^2 \text{Rg}J_{mmm'n'}^{(22)} \\ \text{Rg}S_{mmm'n'} &= -ikk_s \text{Rg}J_{mmm'n'}^{(22)} - ik^2 \text{Rg}J_{mmm'n'}^{(11)} \\ \text{Rg}U_{mmm'n'} &= -ikk_s \text{Rg}J_{mmm'n'}^{(12)} - ik^2 \text{Rg}J_{mmm'n'}^{(21)} \end{aligned}$$

where

$$\begin{bmatrix} J_{mmm'n'}^{(11)} \\ J_{mmm'n'}^{(12)} \\ J_{mmm'n'}^{(21)} \\ J_{mmm'n'}^{(22)} \end{bmatrix} = (-1)^m \int_S dS \hat{n}(\vec{r}) \cdot \begin{bmatrix} \text{Rg}\vec{M}_{m'n'}(k_s, \theta, \phi) \times \vec{M}_{-mn}(kr, \theta, \phi) \\ \text{Rg}\vec{M}_{m'n'}(k_s, \theta, \phi) \times \vec{N}_{-mn}(kr, \theta, \phi) \\ \text{Rg}\vec{N}_{m'n'}(k_s, \theta, \phi) \times \vec{M}_{-mn}(kr, \theta, \phi) \\ \text{Rg}\vec{N}_{m'n'}(k_s, \theta, \phi) \times \vec{N}_{-mn}(kr, \theta, \phi) \end{bmatrix}$$

and

$$\begin{bmatrix} \text{Rg}J_{mmm'n'}^{(11)} \\ \text{Rg}J_{mmm'n'}^{(12)} \\ \text{Rg}J_{mmm'n'}^{(21)} \\ \text{Rg}J_{mmm'n'}^{(22)} \end{bmatrix} = (-1)^m \int_S dS \hat{n}(\vec{r}) \cdot \begin{bmatrix} \vec{M}_{m'n'}(k_s, \theta, \phi) \times \text{Rg}\vec{M}_{-mn}(kr, \theta, \phi) \\ \vec{M}_{m'n'}(k_s, \theta, \phi) \times \text{Rg}\vec{N}_{-mn}(kr, \theta, \phi) \\ \vec{N}_{m'n'}(k_s, \theta, \phi) \times \text{Rg}\vec{M}_{-mn}(kr, \theta, \phi) \\ \vec{N}_{m'n'}(k_s, \theta, \phi) \times \text{Rg}\vec{N}_{-mn}(kr, \theta, \phi) \end{bmatrix}$$

The surface integral is taken on the surface of the particle.

The T-matrix can be expressed as in the form:

$$\vec{T} = - \begin{bmatrix} Rg\vec{P} & Rg\vec{R} \\ Rg\vec{S} & Rg\vec{U} \end{bmatrix} \cdot \begin{bmatrix} \vec{P} & \vec{R} \\ \vec{S} & \vec{U} \end{bmatrix}^{-1}$$

Utilized by this formula, we can derive the T-matrix for any type of homogeneous particles once we know its morphology and composition.

#### D. RESULTS AND DISCUSSIONS

Fig. 9 shows the geometry of particles considered in this study. Sphere, cylinder and hexagonal column are applied. Fig. 9 (a) shows the geometry of a spherical particle, the symbol  $a$  is applied to denote the radius. Thus the maximum dimension of spherical particles can be expressed as  $2a$ . Fig. 9 (b) shows the geometry of a cylinder particle has its radius equals to  $a$  and height equals to  $L$ . Fig. 9 (c) shows the geometry of a hexagonal column with its side length equals to  $a$  and height equals to  $L$ . The three geometries show different degree of symmetry. For example, sphere is the most symmetrical shape cause it will not change under any rotation operations. Cylinders are worse than spheres but maintain unchanged if the rotation is originated along its rotational axis of symmetry. Following previous *in situ* studies, hexagonal columns are selected to model of ice crystals (Heymsfield and Knollenberg, 1972). The T-matrix has not been widely applied to the studies of non-axis-symmetric models (Mishchenko et al., 1997). In this study we are aimed to investigate the single-scattering properties of arbitrary shaped particles. The size parameter is  $x = ka$  for spheres, and

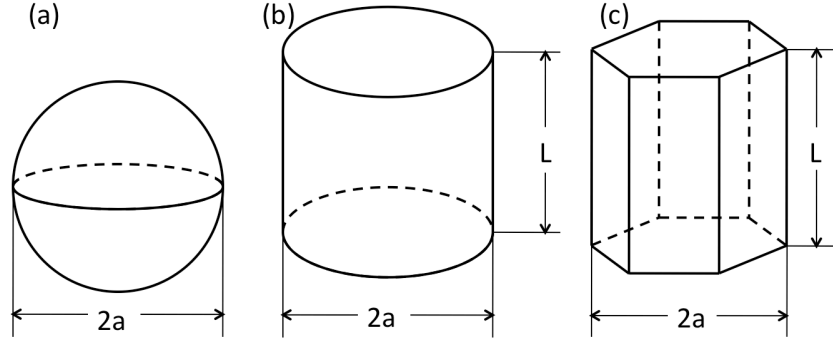


**Fig. 9** Geometries selected in this study.

$x = kL$  for cylinders and hexagonal columns, respectively. Here  $k$  is the wave number for the incident beam,  $k = \frac{2\pi}{\lambda}$ , and  $\lambda$  is the wavelength. The aspect ratio  $ASP = \frac{L}{2a}$  is another derivative parameter on model description.

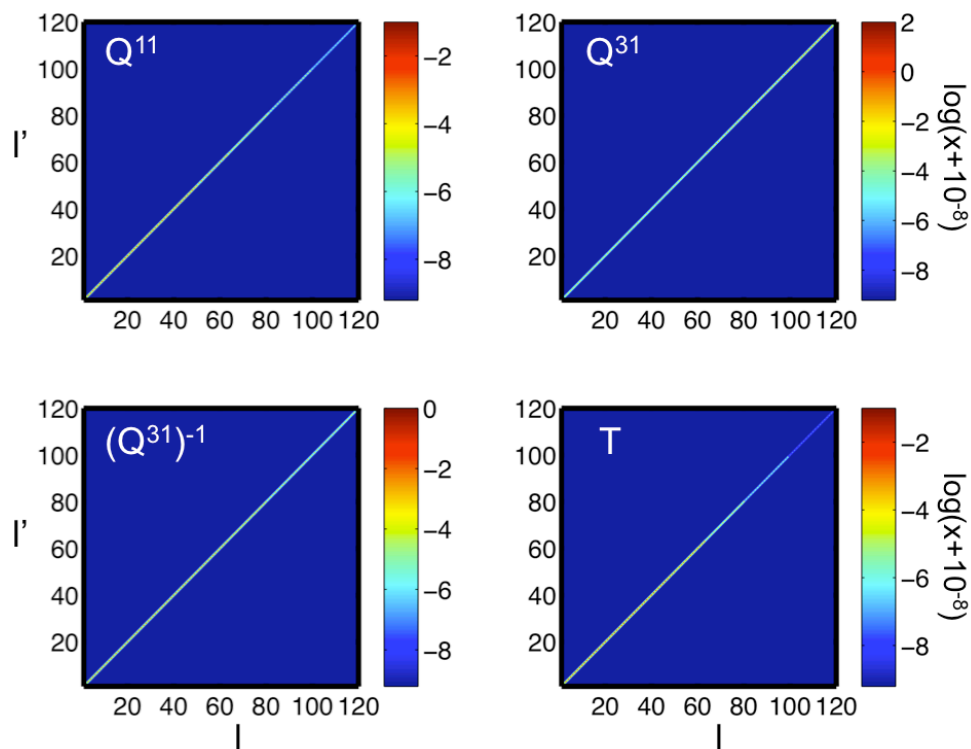
Fig. 10 shows the contour of Q matrices and T-matrix of a spherical particle with size parameter equals to 7.  $N_{\max}$  is selected as 10 in this and the following studies. The x- and y-axis in this contour are set as the combined indices of the matrices. For example,  $T_{ll'}^{(11)}$  is plotted at  $(l, l')$  in the T-matrix contour. In order to make the contour with high contrast, matrix elements are plotted in log-scale with a small displacement. Following the previous discussions, the combined indices of the T-matrix are defined as  $l = n(n+1) + m$ . Therefore there are two systems of indices,  $(l, l')$  and  $(m, n, m', n')$ , to describe the matrix element position. The results in Fig. 8 show that all the matrices involved have non-zero values exist only in their diagonal lines. The results imply that the matrix elements are proportional to the Kronecker's delta function,  $T_{ll'}^{(11)} \propto \delta_{l, l'}$  and  $T_{mm'n'}^{(11)} \propto \delta_{n, n'} \delta_{m, m'}$  consequently. The same rule is also set up for other blocks.

Fig. 11 shows the Q matrices and the T-matrix for a cylinder model. The cylinder's size parameter is 7.0 and its aspect ratio is set as 1.0. The matrices are no longer diagonal for this model. However, it is still “diagonal” in sub-matrices corresponding to indices  $n$  and  $n'$ . The quotation marks imply that those sub-matrices are not square. The fact of “diagonal” suggests that the elements in cylinder's T-matrix are proportional to Kronecker's delta function:  $T_{mm'n'}^{(11)} \propto \delta_{m,m'}$ . This result differs from those of spherical models.

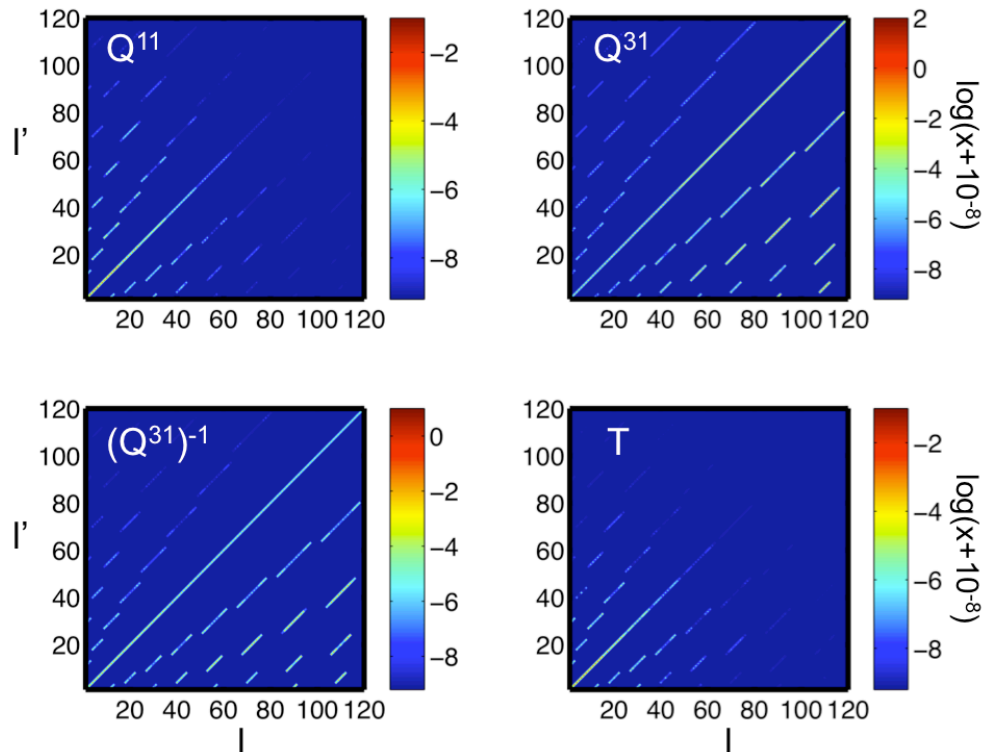
Fig. 12 shows the Q matrices and T-matrix for a hexagonal column. The column has a size parameter equals to 7 and aspect ratio equals to 1.0. The non-zero elements are not restricted on the diagonal lines of the matrices or sub-matrices. Thus matrix elements in this case cannot be expressed in terms of the Kronecker's delta function.

Fig. 13 shows a geometry configuration applied in this study. The aspect ratios for the hexagonal column is set as  $L/2a=1.0$ . Figs. 14 and 15 show the phase matrix of hexagonal columns for this geometry configuration with size parameter  $kL=20$  and 30, respectively.

Fig. 16 shows another geometry configuration. Fig. 16 is different from Fig. 13 due to the different direction of incident beam. Figs. 17 and 18 are similar as Figs. 14 and 15 except for the geometry configuration follow Fig. 16. There are more details shown in the phase matrix for larger particles.



**Fig. 10** Q matrices and T-matrix of a spherical particle with size parameter equals to 7. Only the upper-left sub-matrix ( $T^{11}$ ) is selected to plot.



**Fig. 11** Q matrices and T-matrix of a cylinder particle with size parameter equals to 7. The aspect ratio of the cylinder is set to be 1.0. Only the upper-left sub-matrix ( $T^{11}$ ) is selected to plot.

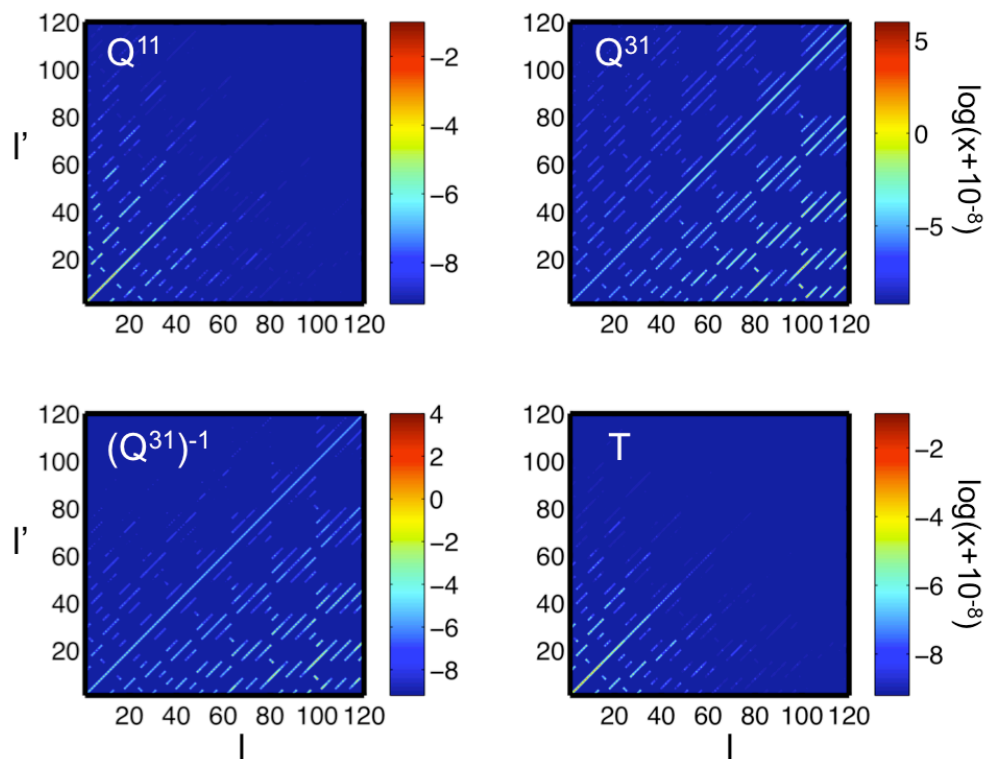


**Fig. 12** Q matrices and T-matrix of a hexagonal column with size parameter equals to 7. The aspect ratio of the cylinder is set to be 1.0. Only the upper-left sub-matrix ( $T^{11}$ ) is selected to plot.

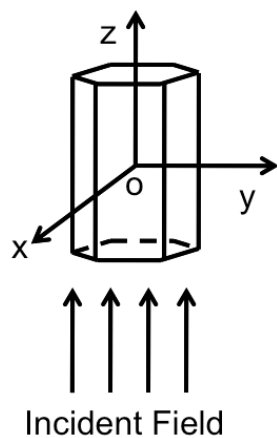


**Fig. 13** Geometry for light scattering problems shown in Fig. 14 and 15. The incident beam has  $\theta_0=0$  and  $\Phi_0=0$ .

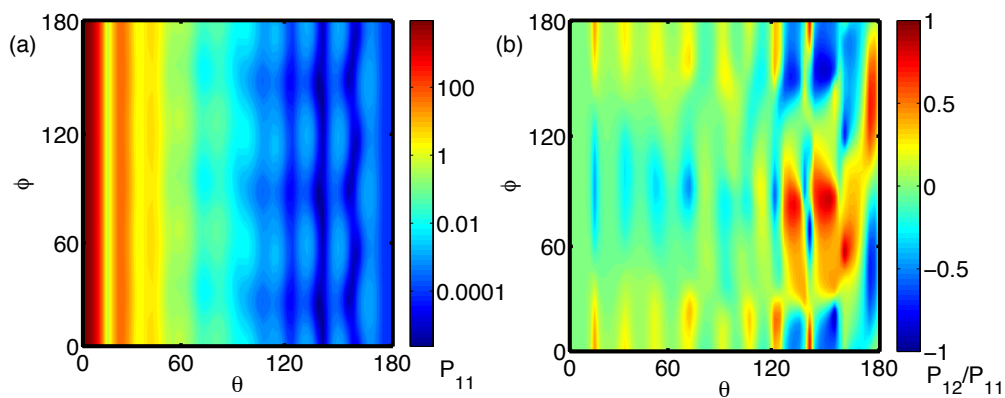


**Fig. 14** Phase function ( $P_{11}$ ) in (a) and  $P_{12}$  in (b) for a hexagonal column with size parameter  $kL=20$  and aspect ratio  $L/2a=1.0$ . The geometry is shown in Fig. 13.

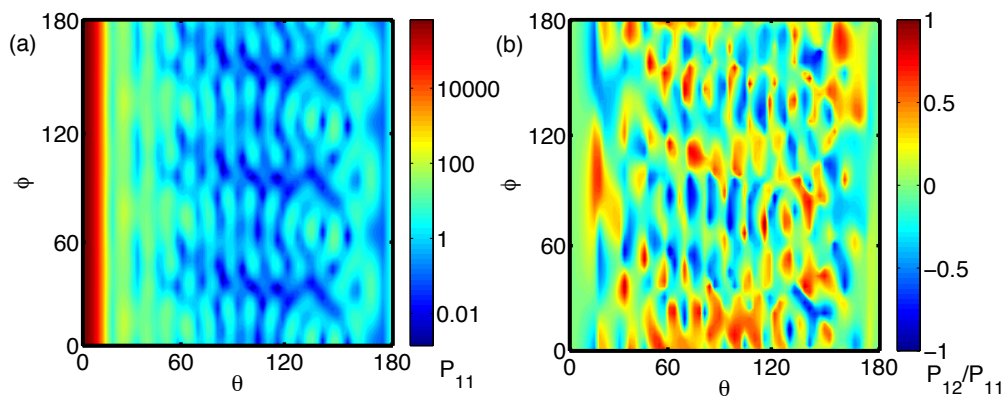


**Fig. 15** Phase function ( $P_{11}$ ) in (a) and  $P_{12}$  in (b) for a hexagonal column with size parameter  $kL=30$  and aspect ratio  $L/2a=1.0$ . The geometry is shown in Fig. 13.

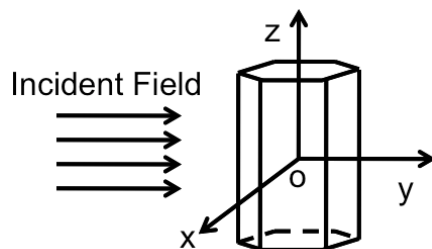


**Fig. 16** Geometry for light scattering problems shown in Fig. 17 and 18. The incident beam has  $\theta_0=90^\circ$  and  $\Phi_0=0$ .

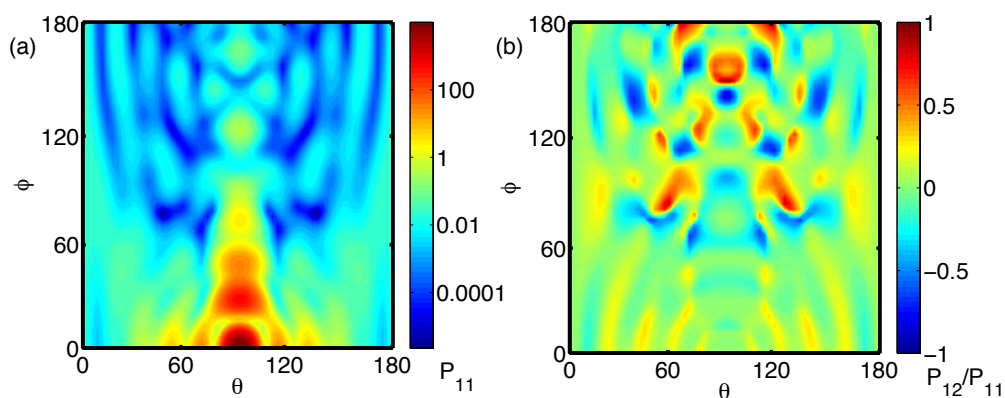


**Fig. 17** Phase function ( $P_{11}$ ) in (a) and  $P_{12}$  in (b) for a hexagonal column with size parameter  $kL=20$  and aspect ratio  $L/2a=1.0$ . The geometry is shown in Fig. 16.

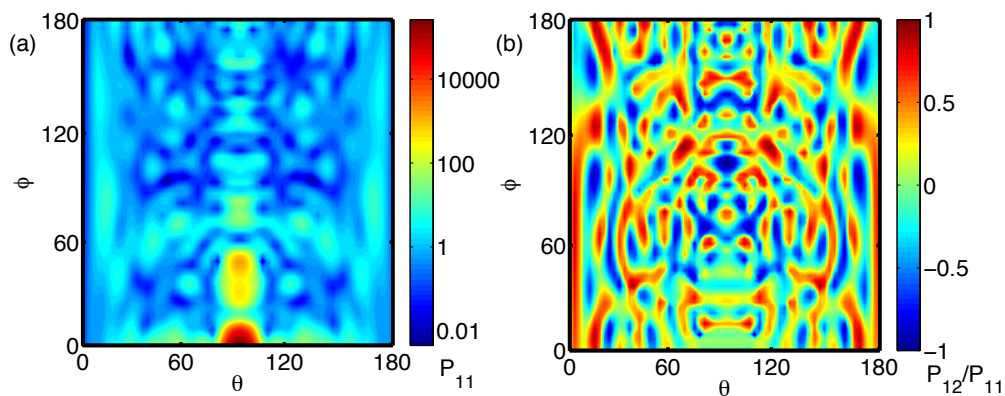


**Fig. 18** Phase function ( $P_{11}$ ) in (a) and  $P_{12}$  in (b) for a hexagonal column with size parameter  $kL=30$  and aspect ratio  $L/2a=1.0$ . The geometry is shown in Fig. 16.



## E. SUMMARY

In this chapter, we have reviewed important concepts and quantities involved in light scattering problems. The single-scattering properties of three types of particle models with arbitrary sizes are derived by the T-matrix method and null-field technique. The applicable size parameter ranges from 0.05 to 30 in this study. Larger particle requires more CPU time and larger memory. The spherical and cylinder models are used to illustrate the basic properties of the T-matrix. The hexagonal columns are selected to mimic the shape of ice crystal. All the models can be equipped to simulate the atmospheric particulates. The results can be applied into actual atmospheric science studies. However, due to long CPU time taken by the calculation, real time simulation is difficult to approach.

## CHAPTER III

### A DATABASE FOR OPTICAL PROPERTIES OF NONSPHERICAL MINERAL DUST AEROSOLS

#### A. INTRODUCTION

Aerosols play an important role in the Earth's climate system through their direct and indirect effects on the energy budget and hydrological cycle of the Earth-atmosphere system (Chylek and Coakley, 1974; Ramanathan et al., 2001; Sokolik et al., 2001; Forster et al., 2007; Shell, 2007). The single-scattering properties of mineral dust are fundamental to quantifying aerosol radiative forcings. For this reason, numerous laboratory studies and theoretical modeling simulations have been carried out (West et al., 1997; Volten et al., 2001, 2006; Muñoz et al., 2004, 2006; Curtis et al., 2008; Sokolik et al., 1998; Tegen and Lacis, 1996; Yang et al., 2007; Bi et al., 2009). Measurements of the scattering and polarization properties of sampled dust aerosols have been very valuable in providing the basic data for verification and improvement of the results determined from theoretical calculations and remote sensing applications. However, due to technical difficulties, experimental determinations of the extinction efficiency, single-scattering albedo and scattering phase matrices around forward and backward scattering directions have been extremely difficult (Volten et al., 2001, 2006; Muñoz et al., 2004, 2006). Furthermore, measurements are restricted to a small number of dust samples and visible wavelengths, which limit the applicability of experimental approaches to the study of the single-scattering properties of dust particles covering the entire solar and thermal

infrared spectra. Thus, a comprehensive modeling study is needed to advance our knowledge and understanding of the optical properties of dust-like aerosols for radiative forcing and remote sensing applications.

Substantial challenges exist in modeling the optical and microphysical properties of dust particles (Nousiainen, 2009), particularly related to their morphology. Electron microscope images (e.g., Reid et al., 2003; Muñoz and Volten, 2006) revealed that mineral dust particles are almost exclusively nonspherical and have irregular shapes without any particular habits. A number of researchers (e.g., Mishchenko et al., 1997, 2003; Kalashnikova and Sokolik, 2004; Yang et al., 2007; Feng et al., 2009) illustrated that modeling of the optical properties of dust particles based on the spherical model, a short-cut to circumvent modeling challenges, leads to large errors in relevant radiative transfer simulations and remote sensing applications. The nonspherical models, such as the spheroidal model, and their corresponding computing techniques, were subsequently developed and applied to the analysis of experimental results involving dust particles (e.g., Mishchenko et al., 1997; Dubovik et al., 2006; Nousiainen, 2009). Based on extensive comparisons between simulated results and experimental data, the spheroidal model representing a geometrical shape with two degrees of morphological freedom (particle size and aspect ratio) (Dubovik et al., 2006) offered a much better solution to the theoretical modeling of optical properties than the spherical counterpart (Hess et al., 1998). Most recently, Bi et al. (2009) investigated the single-scattering properties of the tri-axial ellipsoidal model by introducing an additional degree of morphological freedom to reduce the symmetry of spheroids, which resulted in an improvement to the modeling of dust optical particles.

The objective of the study in this chapter is to develop a database of the single-scattering properties of tri-axial ellipsoids using a combination of four computational methods including the Lorenz-Mie theory (Bohren and Huffman, 1983), the T-matrix method (Waterman 1965; Mishchenko et al., 1997), the discrete dipole approximation (DDA) (Yurkin and Hoekstra, 2009), and an improved geometric optics method (IGOM) (Yang and Liou 1996; Bi et al., 2009). These methods were used to cover various aspect ratios and a size parameter range from Rayleigh to the geometric optics regimes. Specifically, the microphysical properties of the ellipsoidal model were represented in terms of several parameters, including size, two aspect ratios and the refractive index. Following Twomey (1977), King et al. (1978), Dubovik and King (2000), and Dubovik et al. (2004, 2006), we have applied the kernel technique to preserve the accuracy in numerical integrations for various applications associated with this database.

## B. DUST PARTICLE MODEL

A typical tri-axial ellipsoid is shown in Fig. 19, where  $a$  and  $b$  are the two semi-minor and semi-major axes of the equatorial ellipse, and  $c$  is the polar radius. The center of the ellipsoid is set at the origin for simplicity. In principle, the three axes are independent parameters. This database was developed for randomly oriented particles, and it is convenient to assume  $c \geq b \geq a$  without a loss of generality. Two aspect ratios are defined in terms of  $\varepsilon_{a/c}=a/c$  and  $\varepsilon_{b/c}=b/c$ . Note that  $\varepsilon_{a/c}=a/c$  and  $\varepsilon_{b/c}=b/c$  are in the range between 0 and 1, which differ from the conventionally defined aspect ratios that can be larger than unity for spheroidal particles. As illustrated in Fig. 20, employing the present description of the geometric parameters allows various special geometries (spheres, prolate and oblate spheroids) to be determined by specifying the aspect ratio values. The variability of morphology is extended from the cases represented by the two lines to the cases denoted by the triangle area shown in Fig. 20. The range of the two aspect ratios of ellipsoid particles is assumed to be  $0.3 \leq \varepsilon_{a/c} \leq \varepsilon_{b/c} \leq 1$ , which includes the cases for spheres and spheroids (Hess et al., 1998; Dubovik et al., 2006) as a subset of the present data sets.

Considering that the optical properties of individual dust particles are functions of size parameter,  $x$ , the database was developed in terms of  $x$  rather than in the domains of wavelength and size. Size parameter was defined through the maximum dimension (i. e.,  $2c$ ) as  $x=4\pi c/\lambda$ , where  $\lambda$  is the wavelength of the incident plane wave. In line with previous studies (e.g. Henning et al., 1999), the range of size parameter was chosen to be  $0.05 \leq x \leq 2000$ .

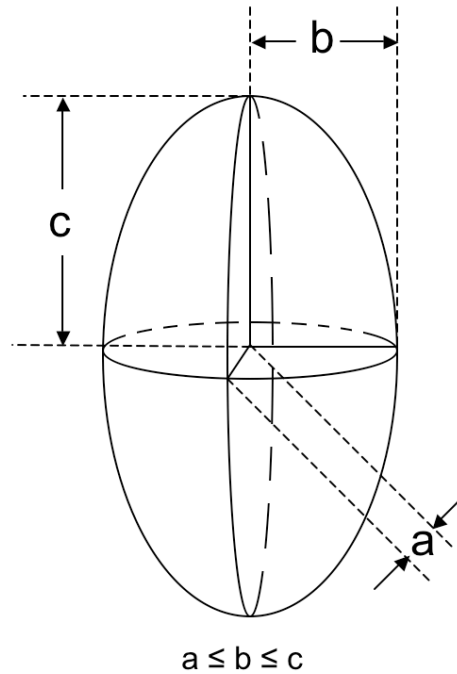


**Fig. 19** The geometry of a tri-axial ellipsoid.

The real and imaginary parts of the complex refractive index of particle models were set as two independent variables. According to the refractive index data compiled by Levoni et al. (1997), the ranges of the dust refractive index from  $0.2 \mu\text{m}$  to  $40 \mu\text{m}$  are as follows:  $1.10 \leq m_r \leq 2.10$  and  $0.005 \leq m_i \leq 0.6$ . In order to cover all the possibilities for the refractive indices of dust in the visible and infrared spectral regions in this database, we have selected the following:  $1.10 \leq m_r \leq 2.10$  and  $0.0005 \leq m_i \leq 0.5$ . For models with large  $m_r$  ( $\geq 1.7$ ),  $m_i$  was assumed to be larger than 0.1. Fig. 21 (a) and Fig. 21 (b), respectively, show the selected region and the data compiled by Levoni et al. (1997) of the real and imaginary parts of the dust complex refractive index. In each panel, the

area between the two dashed lines is the selected region and the solid line is the compiled data for feldspar dust.

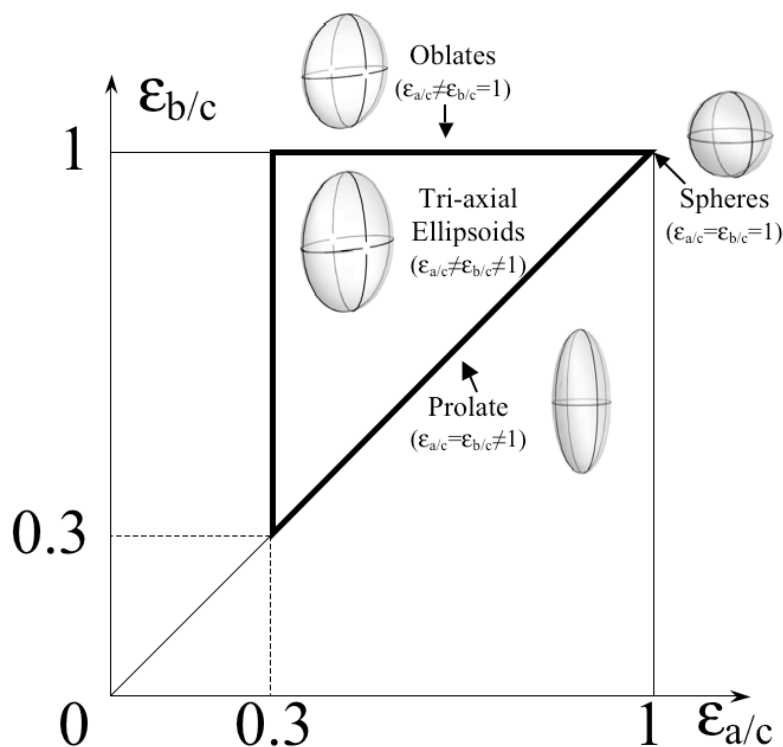


**Fig. 20** The morphology of ellipsoids in 2-D aspect-ratio space. The computation domain is the triangle area including three sides.

The present database has five dimensions including two aspect ratios, a size parameter, and two parts of the complex refractive indices. Due to the substantial computer time required, the optical properties of dust particles were computed at the selected grid points of the microphysical parameters listed in Tables 1 and 2. Higher resolutions of grid points were chosen in the following regions: the small imaginary part of the refractive index, the small size parameters and the shapes close to spheres. These

were chosen because the optical properties are sensitive to variation in the corresponding variables in those regions. The grid points in the size parameter dimension were selected according to a logarithmical scale, as shown in Table. 2. The optical properties at user-defined grid points in the five-dimensional parameter-space can be obtained through the interpolation technique incorporated in the accompanying computer programs.

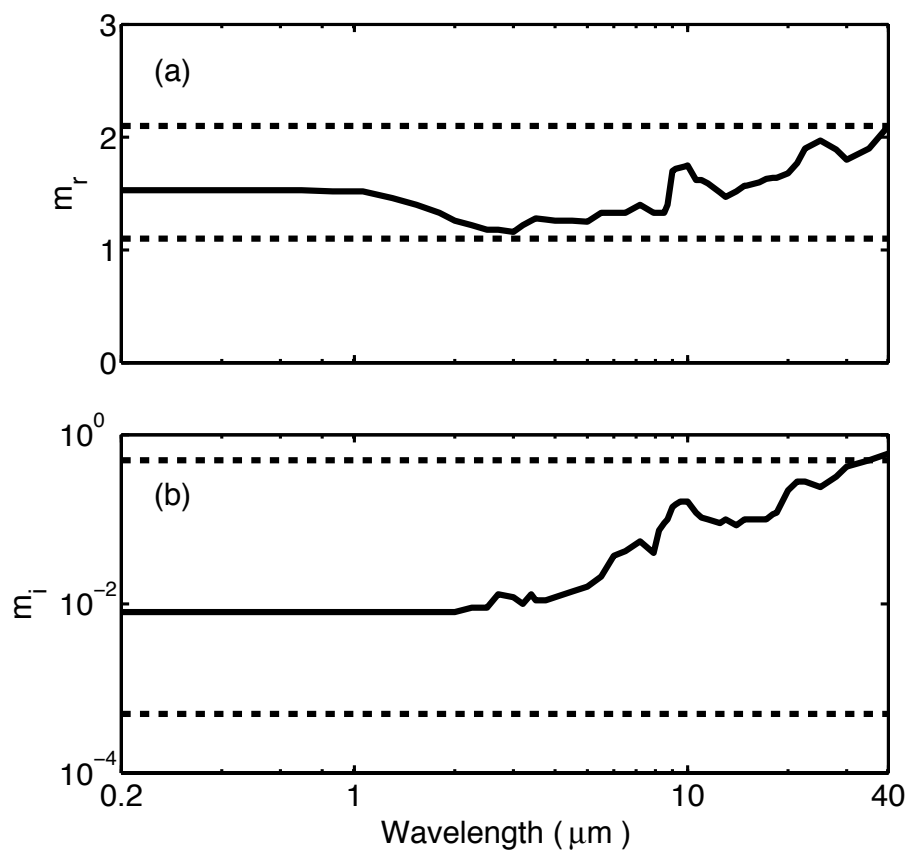


**Fig. 21** Complex refractive indices of dust and the simulation domain (the area between two dashed lines). The data was taken from Levoni et al. (1997).



**Table 1**

The selected aspect ratios and refractive indices for the present scattering simulations

Microphysical Properties	Values
Refractive Index (Real Part)	1.1, 1.2, 1.3, 1.4, 1.5, 1.6, 1.7, 1.9, 2.1
Refractive Index (Imaginary Part)	0.0005, 0.001, 0.005, 0.01, 0.02, 0.05, 0.08, 0.1, 0.2, 0.5
Aspect Ratio ( $\epsilon_{a/c}$ )	1.00, 0.98, 0.95, 0.91, 0.88, 0.86, 0.83
Aspect Ratio ( $\epsilon_{a/c} / \epsilon_{b/c}$ )	0.67, 0.56, 0.48, 0.42, 0.37, 0.30

**Table 2**

The size parameters selected for simulations. Blank cells indicate that simulations were not conducted for the computation method

Technique	Equidistant sampling interval of size parameter							
	0.05-1.00	1.00-5.00	5.00-20.00	20.00-40.00	40.00-80.00	80.00-200.00	250.00-500.00	500.00-2000.00
ADDA	0.05	0.1	1	2	4			
T-matrix	0.05	0.05	0.5	0.5	0.5			
Lorenz-Mie	0.05	0.05	0.05	0.5	0.5	0.5	0.5	0.5
IGOM				2	4	5	10	50

### C. COMPUTATIONAL METHODS

A general tri-axial ellipsoid is a standard quadratic surface in mathematics; however, computing its optical properties over a complete range of size parameters from Rayleigh to the geometric optics domains is a challenging computational endeavor. At present, there are only several computational methods that can be applied to ellipsoidal particles. For small particles, three popular methods have usually been employed, which are the DDA method (Purcell and Pennypacker, 1973, Draine and Flatau, 1994; Yurkin and Hoekstra, 2009), the finite difference time domain (FDTD) method (Yee, 1966, Yang and Liou, 1996a; Sun et al. 1999), and the T-matrix method (Waterman, 1965; Mishchenko et al. 1996). The DDA and the FDTD methods have comparable efficiency and applicability. The T-matrix method lends itself more easily to spheroids than to tri-axial ellipsoids. At present, no single method can efficiently and accurately determine the optical properties of large ellipsoidal particles. For large nonspherical particles, the only approximate methods that are available have been based on the geometric optics approach (e.g., Yang and Liou 1996b; Yang et al., 2007).

Recently, the scattering of light by ellipsoids has been investigated by Bi et al. (2009) using a combination of the DDA and IGOM. The edge effects in the semi-empirical scattering theory (Nussenzveig, 1992) have been incorporated into the efficiency factors in the IGOM. It has been demonstrated that the curvature radius of the profile of the penumbra region (Nussenzveig, 1992) as an essential geometric parameter should be taken into account in merging the extinction efficiency and single-scattering

albedo simulated from the two methods. Accurate single-scattering properties of tri-axial ellipsoids can be obtained for all size parameters.

In this study, for tri-axial ellipsoidal models without any rotational symmetry (i.e.,  $\epsilon_{a/c} \neq 1$ ,  $\epsilon_{b/c} \neq 1$ , and  $\epsilon_{a/c} \neq \epsilon_{b/c}$ ) and for spheroids with extreme aspect ratios, a combination of the DDA and IGOM was employed to calculate their optical properties. The T-matrix method, combined with the IGOM, was applied to the computation of the single-scattering properties of the spheroidal model with small and moderate aspect ratios, whereas the Lorenz-Mie theory was used in the case of spheres. Different scattering methods have different applicable regions in terms of size parameter. The DDA method was applied to determine the single-scattering properties for tri-axial ellipsoidal models with  $x_{eff}$  smaller than 17. The T-matrix method was used for spheroids with  $x_{eff}$  smaller than 30. The Lorenz-Mie theory can provide single-scattering properties covering all size parameters associated with any spherical models. The remaining cases were solved by the IGOM. Computer codes for the four aforementioned scattering methods used in the simulations were: Lorenz-Mie code (Bohren and Huffman, 1983); T-matrix code (Mishchenko et al., 1997); Amsterdam DDA (commonly known as ADDA) code (Yurkin and Hoekstra, 2009); and, IGOM code (Yang and Liou, 1996; Yang et al. 2007; Bi et al., 2009).

To ensure the accuracy of DDA calculations, the criterion,  $dpl=10|m|$ , was applied, where term  $dpl$  stands for ‘dipoles per lambda’ and represents the dipole density. In order to derive the single-scattering properties for randomly oriented particles, we have calculated  $33 \times 9 \times 5$  different orientations within the ranges  $0^\circ \leq \alpha \leq 360^\circ$ , and  $0^\circ \leq \beta \leq 90^\circ$ ,  $0^\circ \leq \gamma \leq 90^\circ$ , which were based on the symmetric properties of ellipsoids, where  $\alpha$ ,

$\beta$  and  $\gamma$  are three Euler angles specifying the particle orientations. Results for different orientations were averaged and saved to represent the optical properties for individual randomly oriented ellipsoids. For the T-matrix and IGOM simulations, the computational parameters in the codes (Mishchenko et al., 1997) were employed without additional modifications.

#### D. DATABASE DESIGN AND USER INTERFACE

The structure of the present database and the logical flow for its application to the determination of the bulk optical properties of dust-like aerosols and the retrieval of dust microphysical properties from remote sensing measurements are illustrated in Fig. 22. The database provides the single-scattering properties of dust particles with pre-defined microphysical and optical parameters, i.e., particle size parameter, aspect ratios and refractive index. The single-scattering properties of an individual dust particle are the extinction efficiency, single-scattering albedo and phase matrix. The notation “Shape X” refers to the selected shapes used for computation. Corresponding with each shape, 69 refractive indices were selected for simulation and noted as “Refr. Index X”. The single-scattering properties for each model were subsequently determined and properly arranged to form the database.

By utilizing the database, the profiles of dust-like aerosols such as size distribution, shape distribution and refractive index can be retrieved from remote sensing measurements by using, for example, a method developed by Dubovik et al. (2006). On the other hand, based on the aerosol profiles, the bulk scattering properties of a mixture

of aerosol particles can be derived from the single-scattering properties stored in the database.

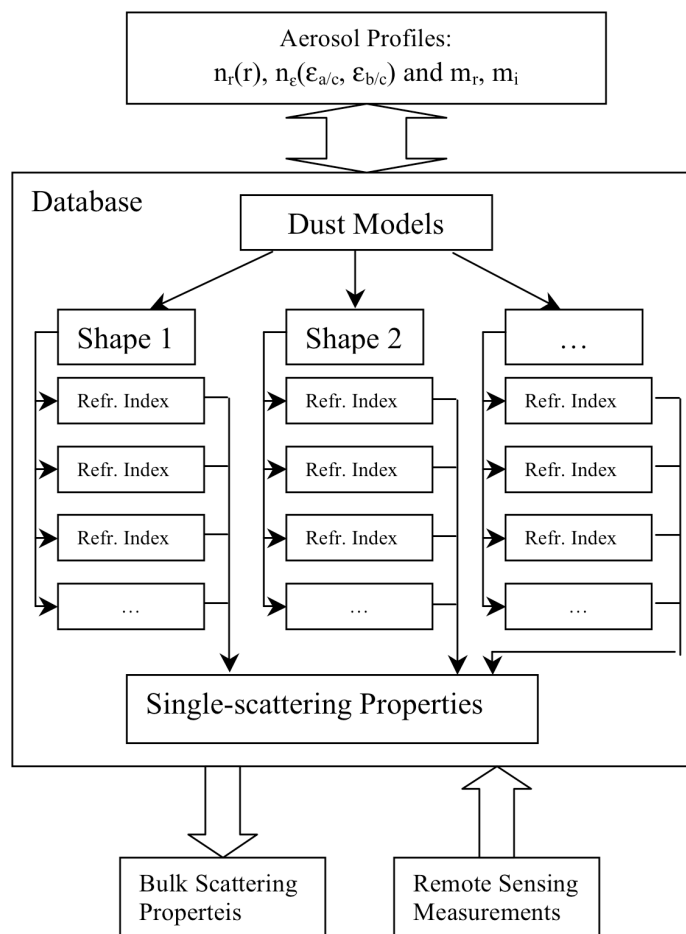


**Fig. 22** The basic logic flow of this database.

In this study, we have applied the kernel technique and formatted the single-scattering properties of particle models in terms of the kernel form. The kernel technique, first introduced by Twomey (1977), has shown to have a number of advantages in recent studies (e.g. Dubovik et al. 2002, 2006; Levy et al., 2007; Verhaege et al., 2009). It has both enhanced the accuracy of results and increased the efficiency of retrieval procedures.

The number distribution,  $dN_x(x)/d\ln x$ , rather than the volume distribution in Dubovik et al. (2006), was applied in building the kernel look-up table of this database. The linear dependence  $dN_x(x)/d\ln x = A\ln x + B$  (when  $x_l \leq x \leq x_{l+1}$ ) was used and coupled with the explicit expression of the kernel function in the form

$$K_{ij}(\dots; x_l) = \int_{\ln(x_l)}^{\ln(x_{l+1})} \frac{\ln(x_{l+1}) - \ln x}{\Delta \ln x} P_{ij}(\dots; x) d\ln x + \int_{\ln(x_{l-1})}^{\ln(x_l)} \frac{\ln x - \ln(x_{l-1})}{\Delta \ln x} P_{ij}(\dots; x) d\ln x, \quad (3.1a)$$

$$K_{sca/ext/abs}(\dots; x_l) = \int_{\ln(x_l)}^{\ln(x_{l+1})} \frac{\ln(x_{l+1}) - \ln x}{\Delta \ln x} c_{sca/ext/abs}(\dots; x) d\ln x + \int_{\ln(x_{l-1})}^{\ln(x_l)} \frac{\ln x - \ln(x_{l-1})}{\Delta \ln x} c_{sca/ext/abs}(\dots; x) d\ln x. \quad (3.1b)$$

Here  $x_l$  ( $0 \leq l \leq 100$ ) indicate the lower and upper limits of size bins. In this study, 100 size-bins were applied in the database. The centers of the size-bins were logarithmically equidistantly spaced; therefore, the bulk scattering properties averaged in terms of a certain size distribution can be expressed as:

$$\bar{c}_{sca}(\dots) \bar{P}_{ij}(\dots; \Theta) = \sum_m \frac{dN_x(x^m)}{d\ln x} c_{sca}(\dots; x^m) K_{ij}(\dots; \Theta; x^m), \quad (3.2)$$

$$\bar{c}_{sca/ext/abs}(\dots) = \sum_m \frac{dN_x(x^m)}{d\ln x} K_{sca/ext/abs}(\dots; x^m). \quad (3.3)$$

Here  $\bar{c}_{sca/ext/abs}(\dots)$  is the averaged scattering/ extinction/ absorption efficiency of a dust particle ensemble,  $\bar{P}_{ij}(\dots; \Theta)$  are the elements of an averaged phase matrix, and  $x^m$  ( $1 \leq m \leq 100$ ) is the center of  $m^{\text{th}}$  size-bin. "...". Eqs. 3.2 and 3.3 denote other parameters of the particle ensemble, such as refractive index and aspect ratio. Further averaging can be established for these two parameters.

NetCDF format (<http://www.unidata.ucar.edu/software/netcdf>) was used to organize the database to make it easily. The database is split into 2898 small files. Each file stores the optical properties of one ellipsoid class having the same aspect ratio and refractive index. It follows that size parameter is the only variable related to the physical properties of dust within each NetCDF file. The structure of the individual NetCDF files is given in Fig. 23. In each file, only one variable named “Database” exists. For each variable, there are three dimensions, which are named “x”, “pos” and “angle”. The first dimension “x” denotes the size parameter  $x$ , which has the sampling points listed in Table 1 and part of Table 2. The second dimension “angle” represents the scattering angle, which has 500 sampling points listed in the corresponding files in the software package. The last dimension “pos” represents the position of an element in the phase matrix. Additionally, the extinction efficiency, the single-scattering albedo and the asymmetry factor can be found in this database.

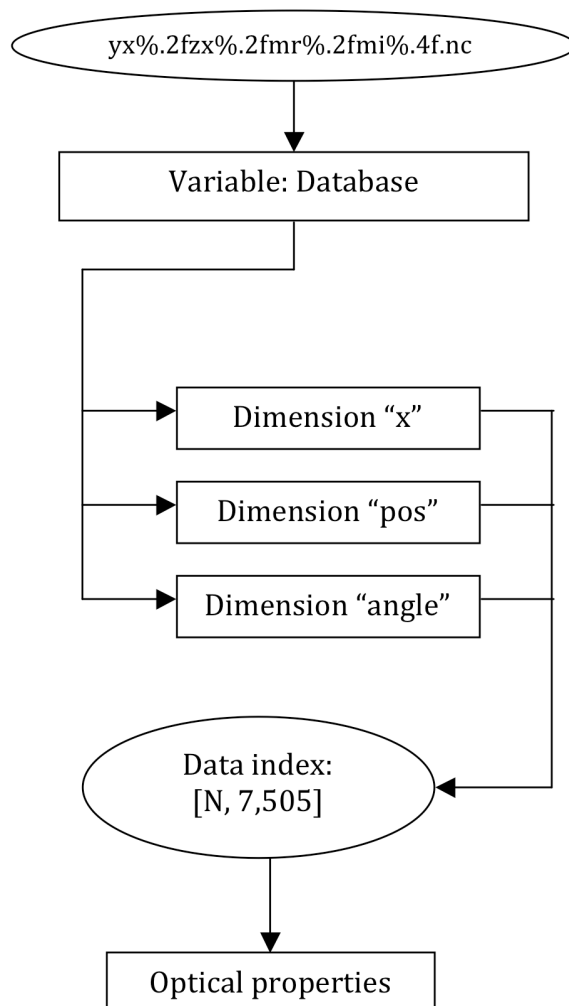


**Fig. 23** The structure of a single NetCDF file. Here ‘N’ denotes the number of the size bins.



## E. RESULTS AND DISCUSSION

Fig. 24 compares the phase matrix of randomly oriented spheroids computed from the ADDA and the T-matrix method in a strongly absorptive case. Results of the two methods agree quite well. Fig. 25 is similar to Fig. 24, except for weakly absorptive particles. Again, the results from the two methods show a close agreement. Since the T-matrix method is a rigorous computational technique for randomly oriented spheroidal particles, the agreement between the ADDA and the T-matrix method indicates that the parameters (e.g., the number of particle orientations) chosen for the ADDA calculations are appropriate.

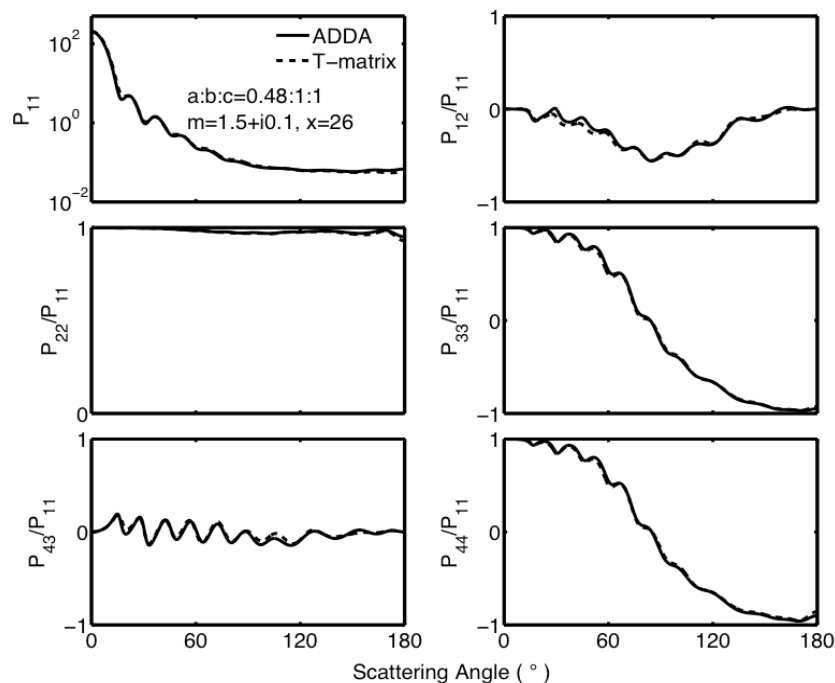


**Fig. 24** Comparison of the six elements of the phase matrix computed from the T-matrix and the ADDA. The size parameter used is  $x=26$ . The axis ratio is given by  $a:b:c=0.48:1:1$ . The complex refractive index  $m$  is  $1.5+i0.1i$ .

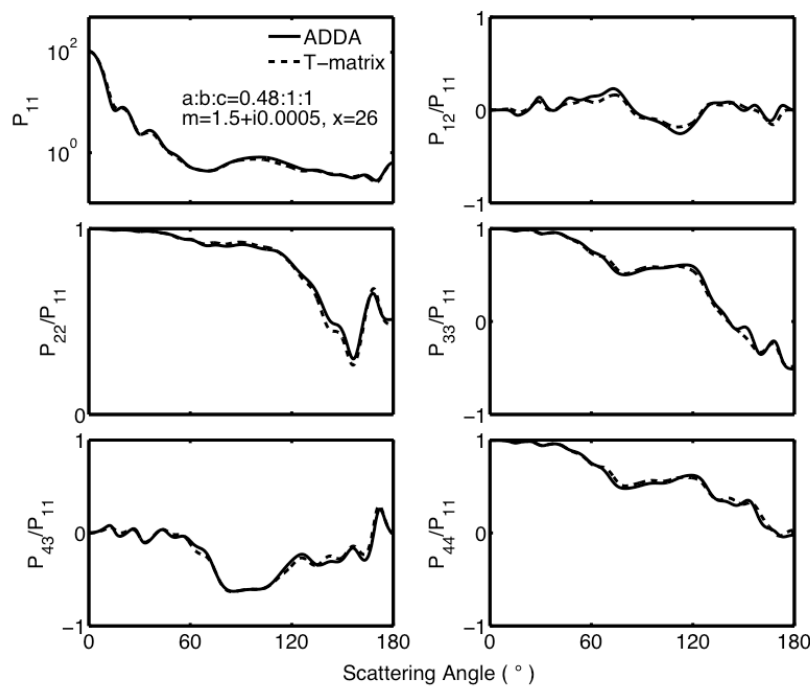
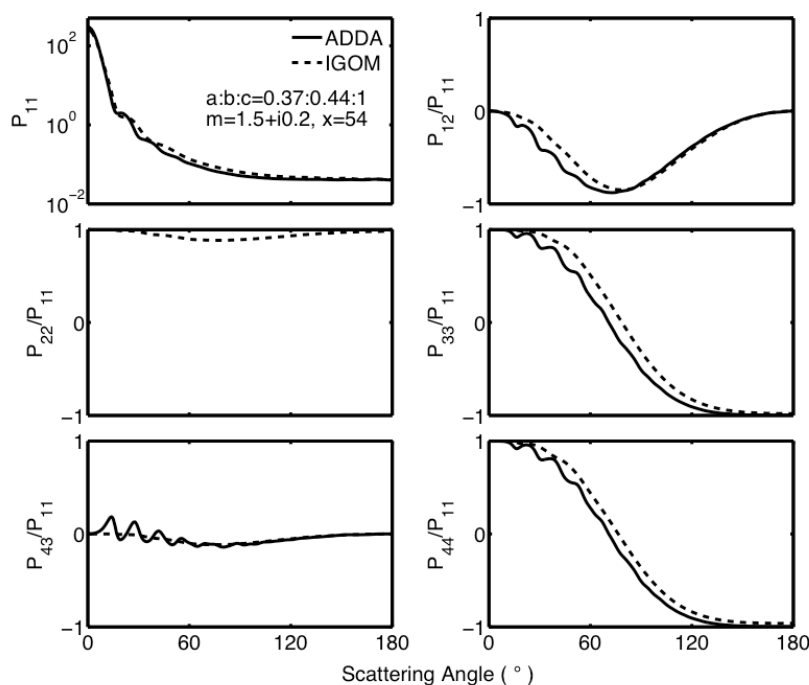


**Fig. 25** Comparison of the six elements of the phase matrix computed from the T-matrix and the ADDA. The size parameter used is  $x=26$ . The axis ratio is given by  $a:b:c=0.48:1:1$ . The complex refractive index  $m$  is  $1.5+i0.0005i$ .

Fig. 26 compares the phase matrices computed by the ADDA and IGOM for a strongly absorptive case. The solid and dashed lines represent the phase matrix results computed by the ADDA and IGOM, respectively, which match well except for some slight oscillations in element  $P_{43}$ . Fig. 27 is similar to Fig. 26, except for a weakly absorptive case. The two methods also show a close agreement. However, the ADDA method displays more oscillations in the phase matrix than the IGOM, partly due to the limitation of accuracy in the IGOM and the number of particle orientations considered in the ADDA calculation.

For ellipsoidal particles whose microphysical parameters do not coincide with the grids, the optical properties can be obtained from an interpolation method. Fig. 28 shows comparison of the interpolated results and the counterparts derived directly from the

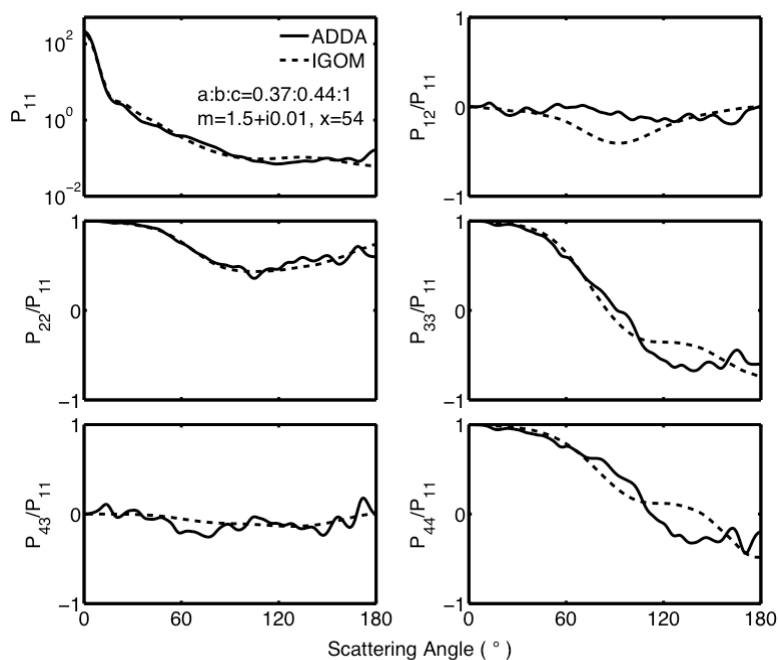
aforementioned computational techniques. In Fig. 28, a strongly absorptive case was chosen in which the aspect ratios were set as  $\epsilon_{a/c}=0.40$  and  $\epsilon_{b/c}=0.64$ , the refractive index was set to be  $1.5502+i0.0916$ , and the size parameter was set at 21. None of these microphysical parameters coincide with the grid points chosen for this database. The interpolation and computed results matched quite well.



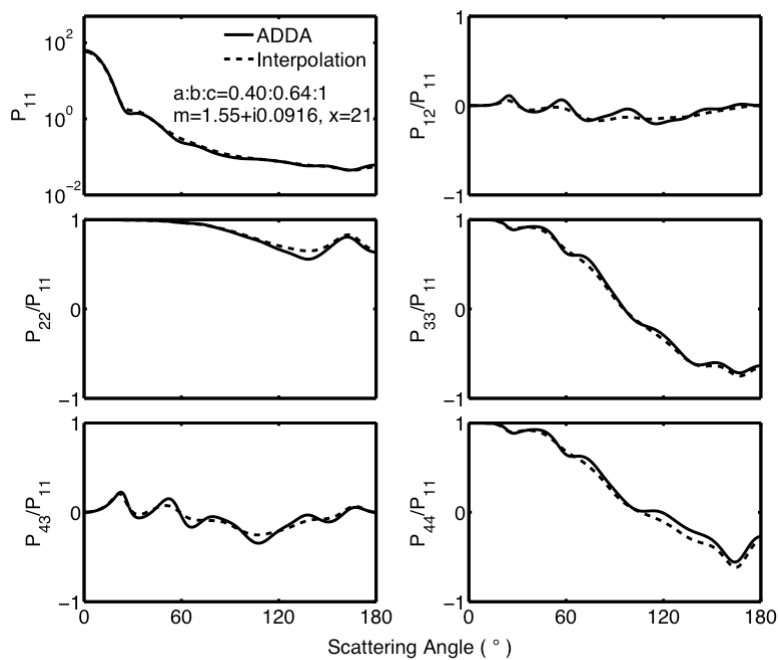
**Fig. 26.** Comparison of the phase matrix computed from the ADDA and the IGOM. The size parameter is 54. The ratio of three radii is  $a:b:c=0.37:0.44:1$ . The refractive index is  $1.5+i0.2$ .

Fig. 29 is similar to Fig. 28, except for weakly absorptive particles. For the phase function, the interpolated results display a close agreement with the computed counterparts. For other elements in the phase matrices, some discrepancies between the two results are shown. Comparison between the interpolated results and those from the direct simulations, shown in Figs. 28 and 29, demonstrates that the resolution of the grid points is reasonable such that interpolations based on this database can be accurate.

Fig. 30 shows the extinction efficiency, single-scattering albedo and asymmetry factor as functions of particle size parameter. Two different complex refractive indices were chosen for this presentation. For the results shown in the left column, the refractive index was set to be  $1.5+i0.005$  with relatively small absorption, while in the right column, the refractive index was selected to be  $1.5+i0.2$  to represent strong absorption. In each column, two different shapes were selected along with ratios of their three semi-axes. The extinction efficiencies increase with size parameter when it is smaller than approximately 9. The single-scattering albedo showed similar behavior to the extinction efficiency but with a maximum located at a size parameter of approximately 5. After reaching their maximums, the extinction efficiency and single-scattering albedo generally decrease with increasing size parameter. The extinction efficiency has several resonance maxima, but their location and magnitude differ for each particle shape, especially for low-absorption cases. The extinction efficiency oscillates and converges to an asymptotic value of 2 as the particle size continues to increase. The single-scattering albedo shows a similar behavior and reaches a value of about 0.53, which coincides with the asymptotic value derived from the geometric optics method. The asymmetry factor, representing the strength of forward scattering, tends to increase with increasing size parameter and converges to 1. Although the optical properties in weak and strong absorptive cases generally show similar features, some differences are apparent. For example, more resonance maxima and oscillations are evident in weakly absorptive cases than their strongly absorptive counterparts.



**Fig. 27** Comparison of the six elements in the phase matrix computed from the ADDA and the IGOM. The size parameter is 54. The ratio of three radii is given by  $a:b:c=0.37:0.44:1$  and the refractive index is  $1.5+i0.01$ .



**Fig. 28** Comparison between interpolated and simulation results. The two aspect ratios are  $\epsilon_{c/a}=0.40$ ,  $\epsilon_{c/b}=0.64$ . The complex refractive index is  $m=1.55+i0.0916$  and size parameter is 21.

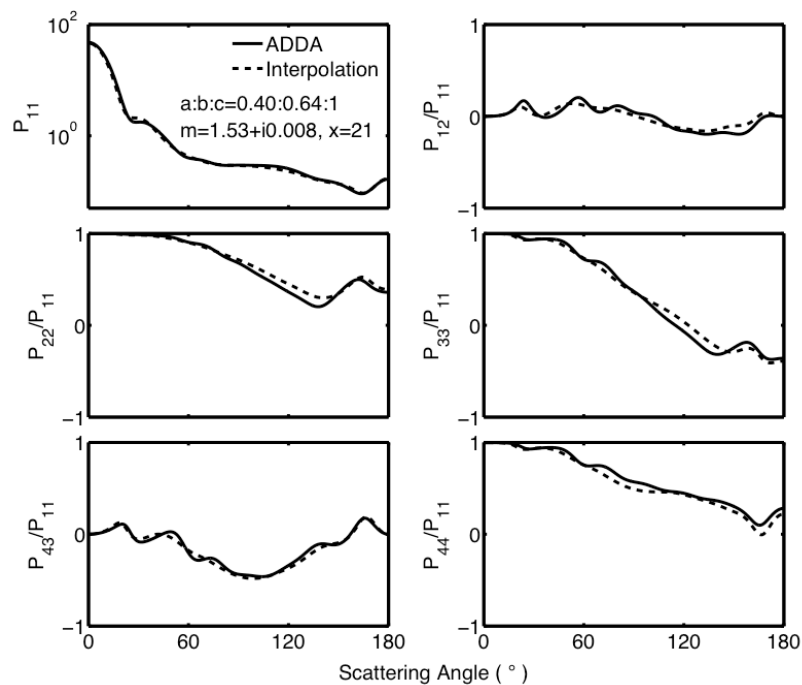


**Fig. 29** Comparison between interpolated and simulation results. The two aspect ratios are  $\epsilon_{c/a}=0.40$  and  $\epsilon_{c/b}=0.64$ . The complex refractive index  $m$  is  $1.53+i0.008$  and size parameter is 21.

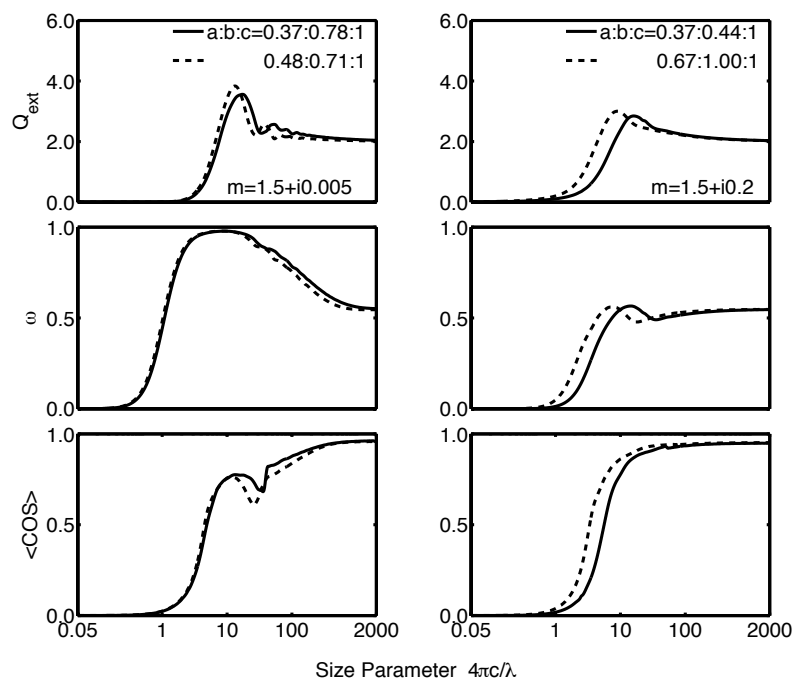


**Fig. 30** Extinction efficiency  $Q_{\text{ext}}$ , single-scattering albedo  $\omega$  and asymmetry factor  $g$  as functions of size parameter for various shapes at two refractive indices. The size parameter is defined in terms of the maximum dimension of ellipsoidal particles.

Fig. 31 shows the extinction efficiency, single-scattering albedo and asymmetry factor of four dust shapes as functions of wavelength for a maximum dimension of 5  $\mu\text{m}$ . The relationship between wavelength and the complex refractive index of dust is the same as that shown in Fig. 21 (Levoni et al. 1997). As shown in Fig. 21, when wavelength increases, the real part of the refractive index of dust has a tendency to increase (valid for wavelengths longer than 2  $\mu\text{m}$ ). The optical properties of dust for cases with refractive indexes within the database region have been obtained by linear interpolation. Because the size parameter of the same particle is inversely proportional to the incident wavelength, the extinction efficiency is approximately equal to 2, and at the same time the single-scattering albedo is about 0.53 for wavelengths shorter than 0.5  $\mu\text{m}$ . When the incident wavelength increases, several maxima appear in both the extinction efficiency and the single-scattering albedo, indicating that scattering events are in the resonance regime. Note that for all morphologies, peaks exist in the extinction efficiency at a wavelength of approximately 10  $\mu\text{m}$ , because the real part of the refractive index reaches its maximum value in this spectral region. The features of the single-scattering albedo are generally similar to those of the extinction efficiency; however, when the incident wavelength is approximately 10  $\mu\text{m}$ , oscillations appear in the single-scattering albedo rather than peaks which are shown in the extinction efficiency. The asymmetric factors for all shapes have a tendency to decrease with increasing wavelength due to a decrease in size parameter.

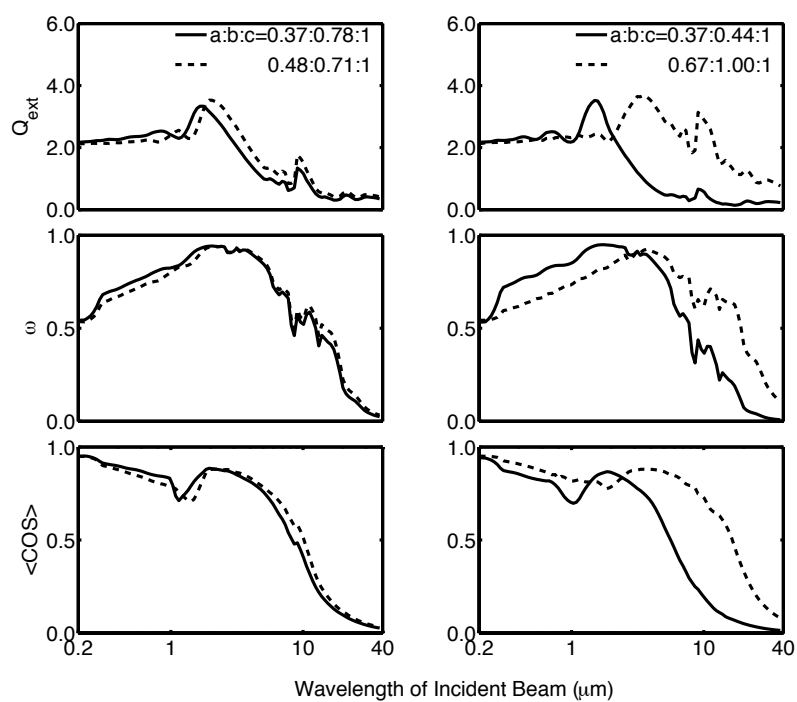


**Fig. 31** Extinction efficiency  $Q_{\text{ext}}$ , single-scattering albedo  $\omega$  and asymmetry factor  $g$  as functions of the incident wavelength. The particles have the same maximum dimension of  $5 \mu\text{m}$ .

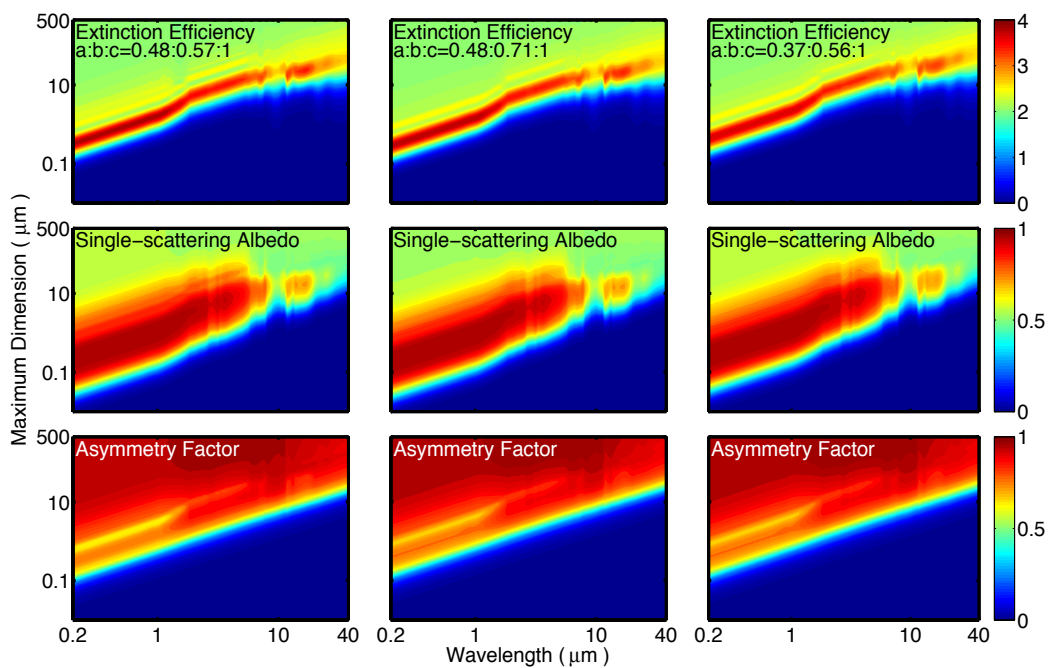


**Fig. 32** Contours of the extinction efficiency, single-scattering albedo and asymmetry factor of three ellipsoidal models as functions of wavelength and maximum particle dimension.



Fig. 32 shows contours for three shapes along with the extinction efficiency, the single-scattering albedo and the asymmetry factor as functions of wavelength and maximum dimension. The upper left corner of each figure corresponds to large size parameters associated with short wavelengths and large particle sizes, revealing that the values approach the geometric asymptotic limit. The lower right corners of the figures correspond to small size parameters with values approaching zero. The diagonal lines (from lower left to upper right) on each figure correspond to moderately sized particles, mostly found in the resonance region. Compared with other regions in the figures, the three quantities vary more rapidly along the diagonal lines.

Fig. 33 shows the bulk scattering properties of a mixture of particle shapes. The size distribution used is based on the Amsterdam light scattering database (Muñoz et al., 2006), in which the weights of different shapes have been chosen to minimize differences in the phase function between the theoretical results and experimental measurements. The dashed lines in Fig. 33 are the results computed from the spherical model according to the size distributions given in the Amsterdam light scattering database. In the theoretical simulation, six sets of aspect ratios,  $a:b:c=0.48:0.71:1$ ,  $0.37:0.56:1$ ,  $0.30:0.45:1$ ,  $0.37:0.78:1$ , and  $0.30:0.64:1$ , were assumed, whose weights were 0.0566, 0.2830, 0.0943, 0.2830, 0.1887, and 0.0943. Comparison of the two models (i.e., the tri-axial ellipsoidal and spherical models) illustrates that the ellipsoidal model provides a much better fit to experimental measurements than the spherical model. The overall features of the optical properties based on the present database closely match the measurements, revealing the advantage of using the tri-axial ellipsoidal model.

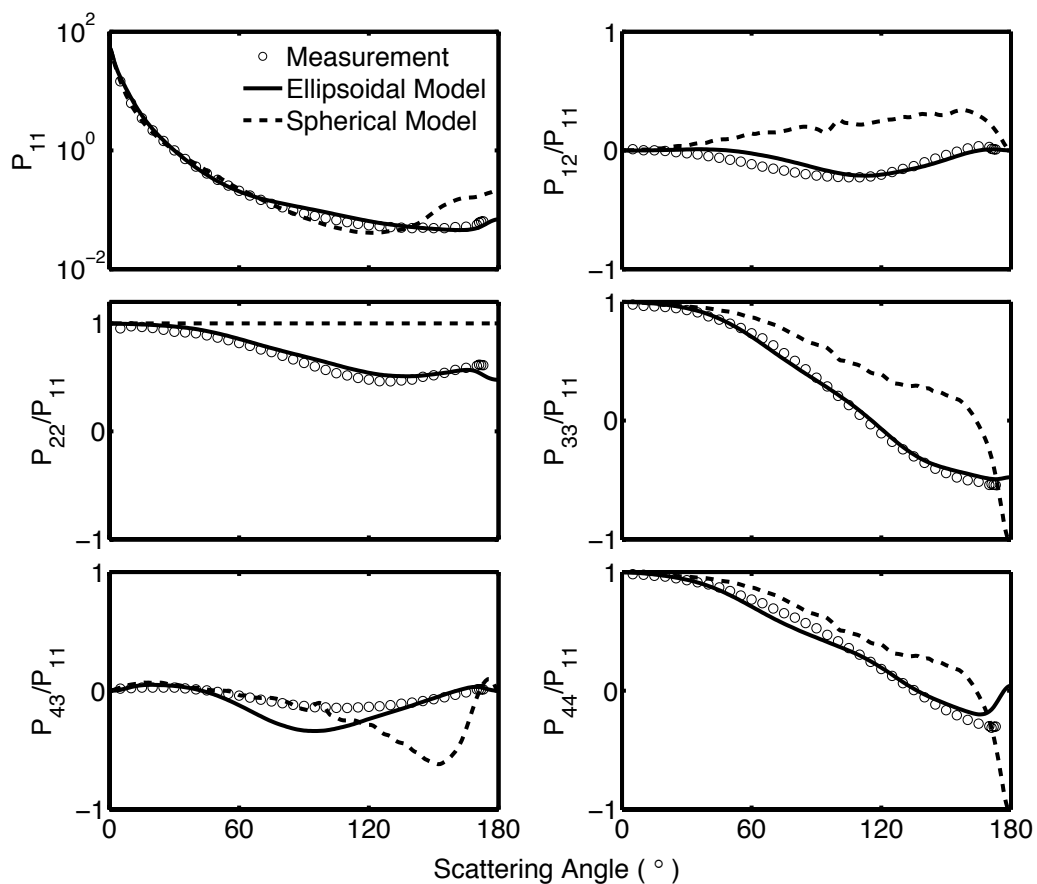


**Fig. 33** Comparison between the measured phase matrix (Volten et al. 2006) and the simulated phase matrix for an ensemble of ellipsoids and for sampled Feldspar aerosols at a wavelength of  $0.6328 \mu\text{m}$ . Six sets of aspect ratios are used in this comparison:  $a:b:c=0.48:0.71:1$ ,  $0.37:0.56:1$ ,  $0.30:0.45:1$ ,  $0.37:0.78:1$ ,  $0.30:0.64:1$  and  $0.30:0.81:1$ . The weights for the six ellipsoids are 0.0566, 0.2830, 0.0943, 0.2830, 0.1887, and 0.0943.

## F. SUMMARY

The single-scattering properties of dust particles are computed from a combination of the Lorenz-Mie theory, the ADDA method, the T-matrix method, and the IGOM method. The tri-axial ellipsoidal model was used to mimic the overall shapes of dust particles with size parameters ranging from 0.025 to 1000 to ensure applicability of the database to most practical cases. For each size parameter, 42 different shapes and 69 different complex refractive indices were selected for simulations. The selection is applicable to simulating the dust optical properties in visible and infrared spectral regions. Utilizing the kernel technique, the optical properties of the ellipsoidal model have been determined and stored as the kernel look-up table. The data is saved in the database files in NetCDF format to ensure that it is available for all major computer languages. A detailed document for the database and accompanying computer programs to extract the data sets are included in the software package.

The database is suitable for analyzing remote sensing measurements based on observations from satellite and ground-base instruments (Holben et al., 1998; King et al., 1999; Deuzé et al., 2000; Kaufman et al., 2002; Marchand et al., 2001). By applying the averaging procedure, the bulk scattering properties can be derived from the database. Comparison between the measured optical properties of dust particles with those computed from the spherical model and a mixture of various ellipsoidal particles demonstrates the advantage of using the tri-axial ellipsoidal model.

## CHAPTER IV

### RADIATIVE TRANSFER (RT) APPLICATION OF NONSPHERICAL AEROSOL MODELS

#### A. INTRODUCTION

The earth's atmosphere contains various types of particulates including aerosols, water droplets, ice crystals and hailstones (Liou, 2002). Those atmospheric particulates, especially aerosols and cloud particles, play an important role in impacting earth's climate system, both directly and indirectly (Chylek & Coakley, 1974; Chuang et al., 2003; Ramanathan et al., 2001). However, the quantitative knowledge of the radiative impact of the particulate is poorly known. This is partly due to their uncertain physical properties. The physical properties, including the morphology and constitution of the particles, are fundamental to quantifying the radiative forcing of the particulates. For this reason, numerous laboratory and *in situ* studies are carried out to study the physical properties of the atmospheric particulates (e.g., Munoz et al., 2004, 2006; Nousiainen et al., 2006; Warren et al., 1994; Volten et al., 2001). Although those studies brought favorable results, they are lack of generality and a global coverage. Recently, remote-sensing techniques are widely applied in atmosphere description. The corresponding retrieval techniques are invented to extract useful information from satellite or ground based observations (e.g., Dubovik et al., 2004, 2006). The remote-sensing observations are aimed to collect the atmospheric radiance that contains the information of the

particulates. Radiative Transfer (RT) models (e.g., Discrete-Ordinates Method (DISORT, Stamnes et al., 1988) and Adding-Doubling Method (de Hann et al., 1987)) play an important role in the retrieval procedure. Previous studies have substantially enriched the knowledge on the optical properties of the various models for dust-like aerosols. Further investigation of their impact on the Radiative Transfer (RT) properties is presented in this chapter. A polarized adding-doubling RT model (de Hann et al., 1987) is applied to simulate the atmospheric radiance and polarization configuration observed by the satellite. Various model size, morphology, composition and inhomogeneity are applied in the RT model.

This study is aimed to present a practical application of the aerosol models and the newly built database. Based on the pre-computed single-scattering properties of the tri-axial ellipsoidal dust-like aerosol models, the polarized radiative transfer profiles can be derived via the adding-doubling RT model. The aerosol models are defined and discussed in detail in Section 2. The corresponding atmosphere layer applied in this study is defined as well. The polarized adding-doubling RT model is equipped to simulate the reflectance and transmittance of the atmosphere layer. The results are presented and discussed in Section 3.

## B. MODEL SELECTION AND METHODOLOGY

A homogeneous atmosphere layer that filled with aerosols is considered in this study. The configuration of the atmosphere layer, incident beam, ground surface and aerosol particles is described in Fig. 34. The atmosphere layer is bounded with a

Lambertian surface at its bottom side with its reflectance albedo  $\omega_0$ . If  $\omega_0 = 0$ , the layer is bounded with a black ground.

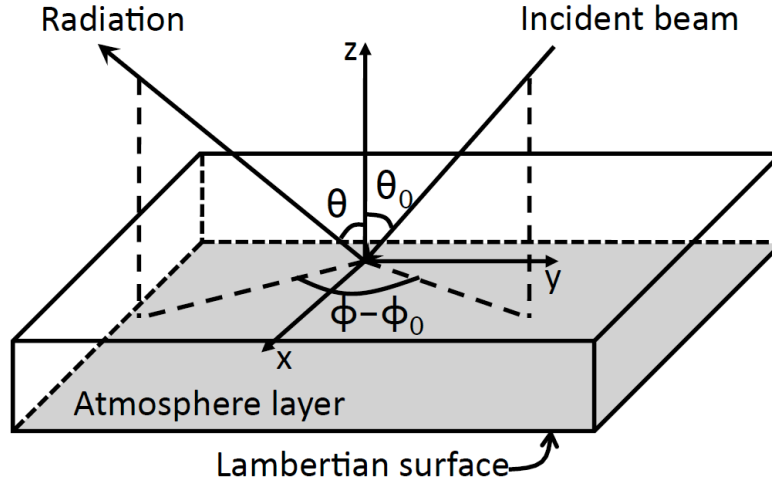


**Fig. 34** The configuration of the atmosphere layer, incident beam, ground surface and aerosol particles considered in this study.

The aerosols that fill up the atmospheric layer are characterized by their optical thickness and physical properties. Following Mishchenko et al. (1997), the optical thickness of the aerosols is set in the range between 0.01 and 1.00. The size distribution, refractive index and morphology are selected to represent the physical properties of the aerosol particles.

Following Hansen et al. (1974), a Gamma distribution of aerosol size is supposed in this study:

$$n(r) = Cf^{\frac{1-3b}{b}} \exp\left(-\frac{r}{ab}\right)$$

with a normalization condition:

$$\int_0^{\infty} n(r) dr = 1$$

For this distribution, the parameter  $a$  and  $b$  coincide with the cross-sectional-area weighted effective radius  $r_{\text{eff}}$  and the effective variance  $v_{\text{eff}}$ , respectively.

$$a \equiv r_{\text{eff}} = \frac{1}{G} \int_0^{\infty} dr \pi r^3 n(r)$$

$$b \equiv v_{\text{eff}} = \frac{1}{G r_{\text{eff}}^2} \int_0^{\infty} dr (r - r_{\text{eff}})^2 \pi r^2 n(r)$$

where

$$G = \int_0^{\infty} dr \pi r^2 n(r)$$

is the average particle geometric cross-sectional area. Following Mishchenko et al (1997), the effective variance of the Gamma distribution is set as  $v_{\text{eff}} = 0.2$  to result a moderately wide size distribution. The effective radius  $r_{\text{eff}}$  ranges from  $0.01\mu\text{m}$  to  $2.00\mu\text{m}$ .

Following the discussions in Chapter II, the typical tri-axial ellipsoidal models are selected in this study. The newly built database allows us to conveniently acquire the single-scattering properties of tri-axial ellipsoids. The aspect ratio considered in this study ranges from 0.45 to 1.00. Different from previous studies, inhomogeneous aerosol particles are considered as well as their homogeneous counterparts in spite that the former optical properties are based on the latter ones. Inhomogeneous models considered in this study is black spherical soot coated by water, as shown in Fig. 35. For homogeneous particle models, the refractive index ranges from 1.3 to 1.6 for the real part, and 0.001 to 0.1 for the imaginary part. For inhomogeneous models, the refractive index is derived by the effective-medium theory.

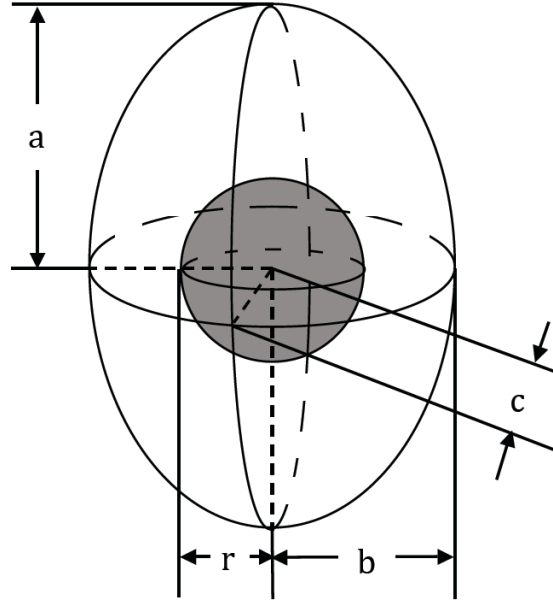


Fig. 35 Geometry of coated tri-axial ellipsoidal particles.

The effective-medium theory builds up a relation between the optical properties of the inhomogeneous and homogeneous particles. It enables us to look up the optical properties (i.e. extinction efficiency, scattering efficiency and phase matrix) of inhomogeneous particles from the existing databases (Meng et al., 2010). For example, according to the Maxwell-Garnett theory (Garnett, 1904, 1906), the effective optical constant is given by:

$$\frac{\epsilon_{eff} - \epsilon_2}{\epsilon_{eff} + 2\epsilon_2} = f_1 \frac{\epsilon_1 - \epsilon_2}{\epsilon_1 + 2\epsilon_2}$$

Here  $\epsilon_1$  and  $\epsilon_2$  are the optical constants of two components, respectively.  $f_1$  is the volumes fraction of the material with optical constant  $\epsilon_1$ .  $\epsilon_{eff}$  is the desired effective optical constant. However, Maxwell-Garnett theory is restricted for small  $f_1$ . Bruggeman solves this problem by giving expression (Bruggeman, 1935):



$$f_1 \frac{\epsilon_1 - \epsilon_{eff}}{\epsilon_{eff} + s(\epsilon_1 - \epsilon_{eff})} = f_2 \frac{\epsilon_2 - \epsilon_{eff}}{\epsilon_{eff} + s(\epsilon_2 - \epsilon_{eff})}$$

Here  $f_1$  and  $f_2$  are the volume fractions of two components, and  $s$  is a geometric factor defined by the shape of the aerosol core. For 3-dimensional composite with compact, the aerosol cores are set as spheres with  $s = \frac{1}{3}$  (Zeng et al., 1988).

The sensitivity study is made subject to the effective size and refractive index (both real part and imaginary part) for homogeneous particles, and the coating thickness for inhomogeneous particles, respectively. The incident wavelength is  $0.875\mu\text{m}$  for all the studies. Following previous studies (Chang and Charalampopoulos, 1990; Bashkatov and Genina, 2002), we set the refractive index as  $m=1.3274+i0.0$  for water, and  $m=1.6327+i0.487$  for soot,  $m=1.53+i0.008$  for dust-like aerosol for all studies not subjected to the refractive index.

The light scattering in the ocean body and Rayleigh scattering in the atmosphere are negligible under the incident wavelength of  $0.875\mu\text{m}$ . Thus this relative long incident wavelength is advantaged to simplify the simulation procedure (Mishchenko et al., 1997). The molecular scattering and absorption optical thickness are both set as 0. All the RT simulations are done for the whole polarization configuration that includes four Stokes parameters. The number of Gauss points is selected as 22 in this study. The Mueller matrices are expanded into 32 terms for models with  $r_{eff} < 0.5\mu\text{m}$ , and 64 terms for the rest models. The background of the layer is set as a Lambert surface with albedo  $\omega_0$ . In most of the studies,  $\omega_0 = 0$ .

### C. RESULTS AND DISCUSSIONS

Fig. 36 shows the Mueller matrix of a spherical model and a tri-axial ellipsoidal model with aspect ratio  $\varepsilon_{a/c} = 0.5, \varepsilon_{b/c} = 0.7$ . The aforementioned Gamma distribution with effective size  $r_{eff} = 1\mu m$  and effective variance  $v_{eff} = 0.2$  is applied. The incident wavelength is  $0.875\mu m$ . The refractive index chosen as  $m=1.53+i0.008$  for typical dust-like aerosols.

Fig. 37 shows the Stokes vector of the reflectance of an atmosphere layer illuminated by a beam. In this study the spherical models shown in Fig. 36 is utilized. The incident direction is  $\mu_0 = 0.8, \phi_0 = 0^\circ$ . The aerosol optical thickness is set as 0.2. The contour is plotted in polar coordinate. The zenith angle  $\theta$  and the polar angle is  $\phi$  of the viewing geometry is set as the radius and polar angle of the contour, respectively. The molecular scattering and absorption optical thickness are negligible as the illumination wavelength is  $0.875\mu m$ . The Stokes parameters Q, U and V are divided by I in this contour. The intensity is relatively weak respect to the incidence, unless the viewing zenith angle is close to  $90^\circ$  and  $\phi$  is close to  $180^\circ$ . For parameters I and Q, a mirror symmetry respect to the incident plane can be found in the contour. The absolute values of parameters U and V obey the same symmetry rule, either. Furthermore, Q and V have zero values once the reflectance plane and the incident plane coincides (i.e.,  $\phi - \phi_0 = 0^\circ$ , or  $\phi = 0^\circ$  in this case).

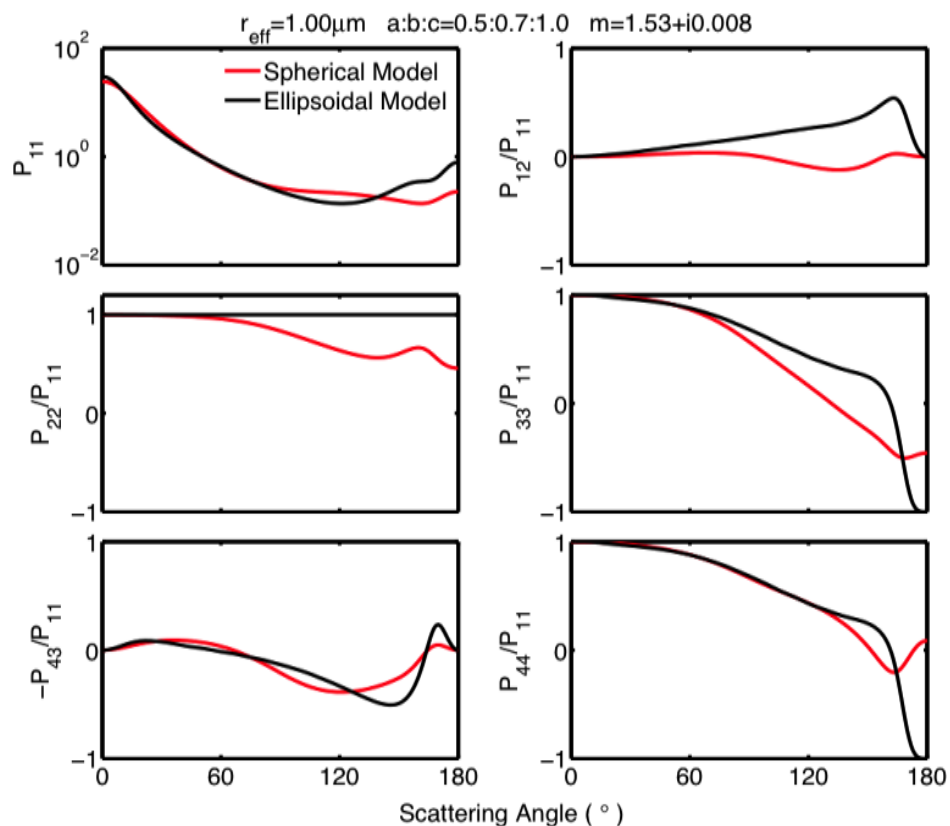
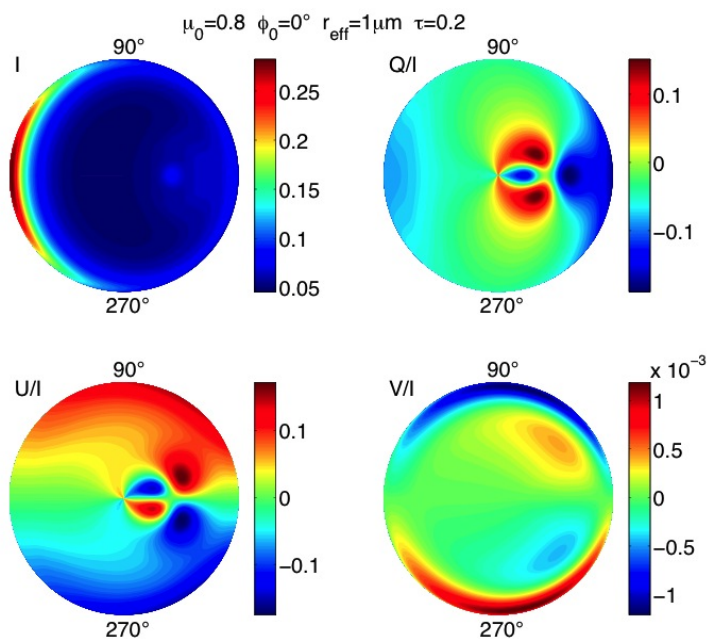


**Fig. 36** The Mueller matrix of a tri-axial ellipsoidal model. A Gamma size distribution with  $r_{\text{eff}}=1\mu\text{m}$  and  $v_{\text{eff}}=0.2$  is applied. The refractive index is set as  $m=1.53+i0.008$ . The aspect ratio is  $\varepsilon_{a/c}=0.5$ ,  $\varepsilon_{b/c}=0.7$ . The incident wavelength is set as  $0.875\mu\text{m}$ .

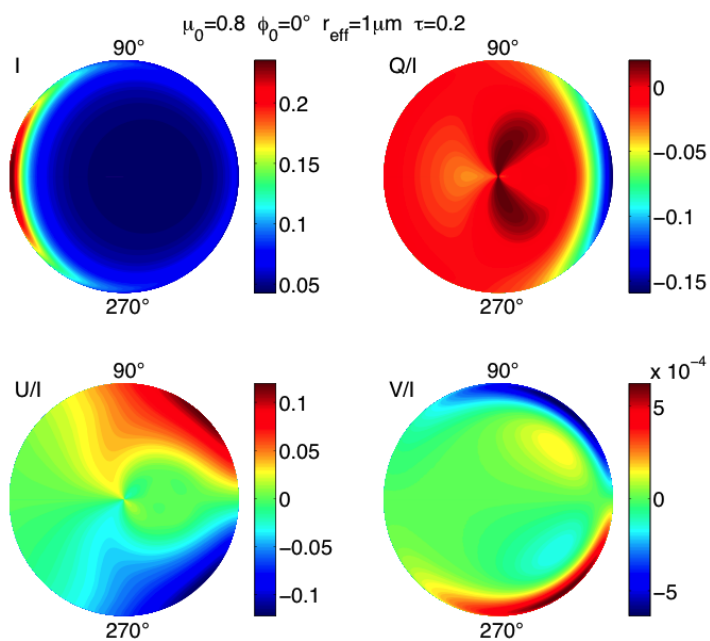
Fig. 38 is similar as Fig. 37, except the spherical model is replaced by the ellipsoidal model with phase matrix shown in Fig. 36. The contours of the ellipsoidal models show less detail than that of the spherical models. Its back-scattering effect is negligible compared with the spherical counterparts.

Fig. 39 is similar as Fig. 37 except the aerosol optical thickness is set as 0.5. The basic properties and symmetries still exist in this contour except the Stokes parameters vary more violating versus the viewing angles. The reflectance of ellipsoidal models with aerosol optical thickness 0.5 is shown in Fig. 40. The varying range is expanded compared with Fig. 37 due to the increase of the aerosol optical thickness.

Fig. 41 plots the reflectance Stokes parameters versus the aerosol optical thickness and the effective radius. The zenith angle of the incident beam is  $\mu_0 = 0.8$ . The reflectance is measured at the viewing angle  $\mu = 0.6$  and  $\phi - \phi_0 = 0^\circ$ . This configuration is analogous to the space based satellite observation. We have supposed the aerosol refractive index is known beforehand and is equal to  $1.53+i0.008$ . The aerosol geometry is modeled by ellipsoidal particles with aspect ratio  $\varepsilon_{a/c} = 0.5, \varepsilon_{b/c} = 0.7$ . Thus only the optical thickness and the effective radius must be retrieved from the measurements. Gamma size distribution is applied in this study. The effective radius of the size distribution ranges from  $0.2\mu\text{m}$  to  $1.0\mu\text{m}$  with step  $0.01\mu\text{m}$ . The aerosol optical thickness ranges from 0.01 to 1.00 with step 0.01. The upper-left contour shows that the reflectance is not very sensitive with the change of the effective radius. Contrarily, the upper-right contour shows Stokes parameter Q of the reflectance is not sensitive with the variance of aerosol optical thickness. The parameters U and V constantly equal to zero under this geometry. They are not plotted in this contour.



**Fig. 37** The reflectance Stokes vector of an atmosphere layer illuminated by a beam. A spherical model is selected. The aerosol thickness is set as 0.2.



**Fig. 38** Similar as Fig. 37 except a tri-axial ellipsoid model is applied.

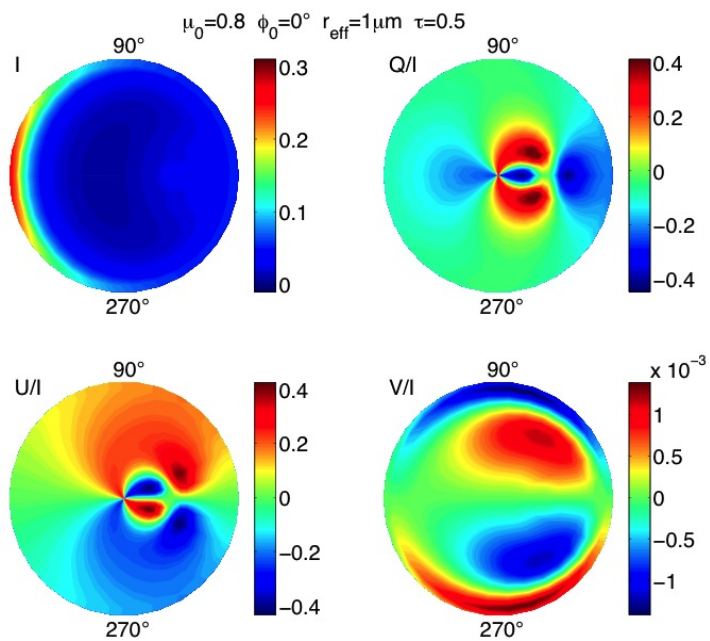


**Fig. 39** Similar as Fig. 37 except the aerosol optical thickness is set as 0.5.

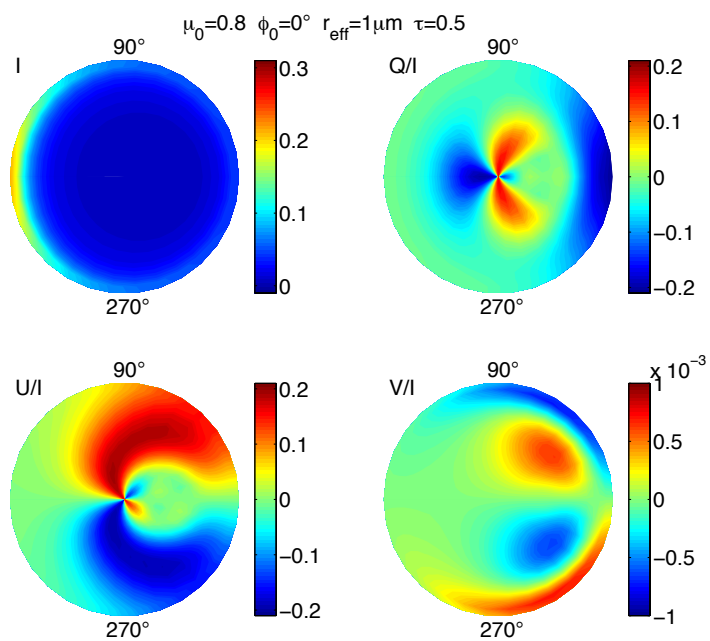


**Fig. 40** Similar as Fig. 38 except the aerosol optical thickness is set as 0.5.

Figs. 42, 43 and 44 are similar as Fig. 41 except the change on viewing geometry. Similarly, different reflectance Stokes parameters show different sensitivity patterns versus the aerosol optical thickness and the effective radius. However, for the case  $\phi - \phi_0 = 120^\circ$ , the reflectance polarization parameters Q and U show less resolution at the upper-right corner (i.e., cases with large effective radius and large aerosol optical thickness).

Based on the remote-sensing results, the unknown physical properties of airborne aerosols can be retrieved. For example, the observation, both intensity and state of polarization, can be made by a space-based satellite at certain viewing angle. By matching the observation with a large pre-computed candidate set, the unknown aerosol properties can be re-constructed. In this study, a combination of both reflectance intensity and polarization are preferred due to their different sensitivity patterns.

The figure which appears on pg. 76 shows the optical thickness and effective radius retrieval results. Since the refractive index and morphology are supposed to be known beforehand, we only need to retrieve the effective size and the aerosol optical thickness. In each retrieval procedure a standard model with definite aerosol optical thickness and effective radius is selected. The retrieval is aimed to re-construct the aerosol optical thickness and effective radius by matching the reflection of the standard and candidate models. The reflectance of candidate models is pre-computed. In the study shown in Fig, 45, four standard models with  $\tau=0.2$  and  $r_{\text{eff}}=$  (a)  $0.3\mu\text{m}$  (b)  $0.5\mu\text{m}$  (c)  $0.7\mu\text{m}$  and (d)  $0.9\mu\text{m}$  are selected in this study. The incident and viewing geometry is set as  $\mu_0=0.8$ ,  $\mu=0.6$  and  $\phi-\phi_0=0^\circ$ . Thus the results in Fig. 41 can be equipped in this study. The candidate models are selected according to the intensity criteria:

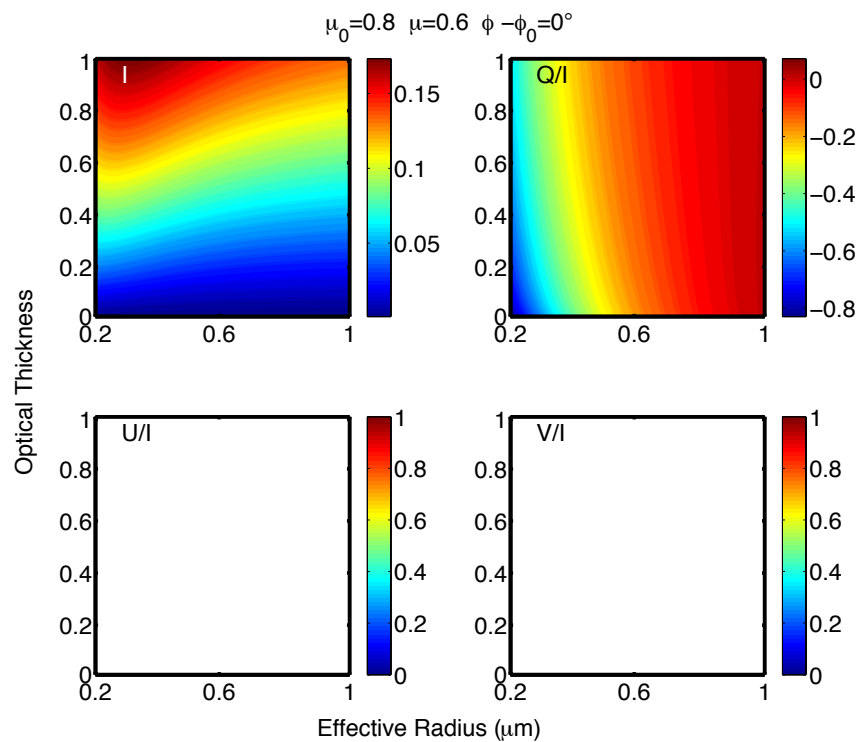


**Fig. 41** The Stokes parameter of the reflectance of an atmosphere layer versus the aerosol optical thickness and the effective radius of the aerosol model. The incident zenith angle is  $\mu_0=0.8$ , the viewing angle is  $\mu=0.6$  and  $\phi-\phi_0=0^\circ$ .

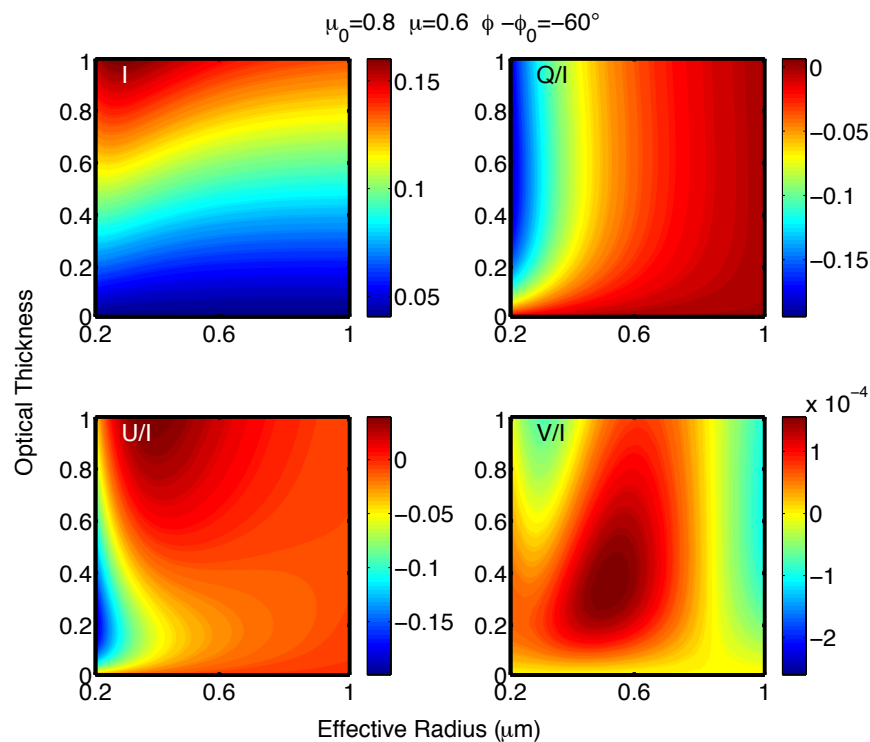


**Fig. 42** Similar as Fig. 40, except the viewing angle has  $\phi-\phi_0=-60^\circ$ .



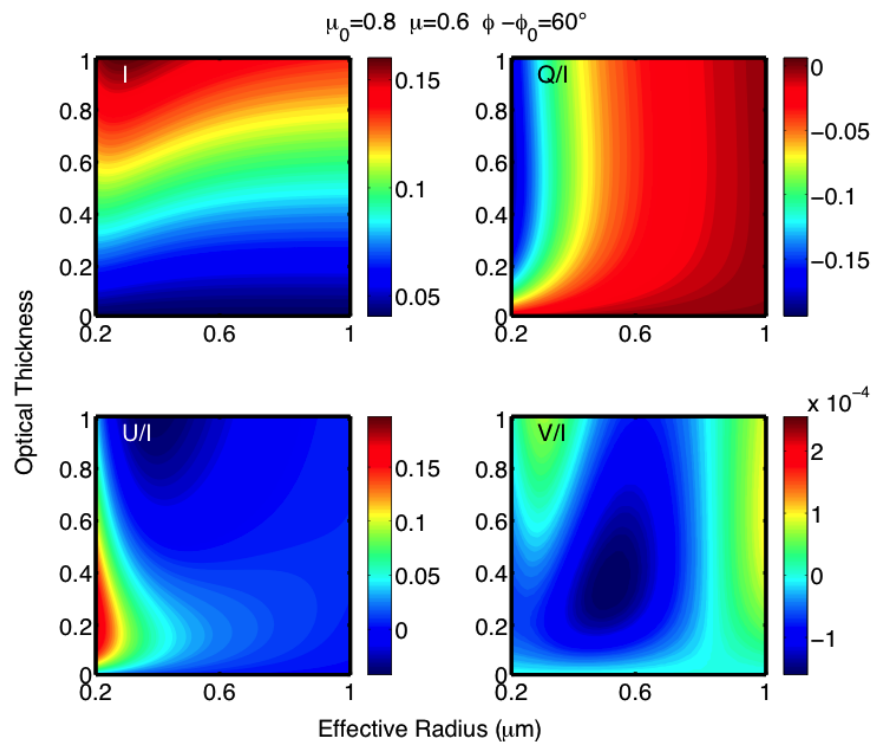


**Fig. 43** Similar as Fig. 40, except the viewing angle has  $\phi-\phi_0=60^\circ$ .

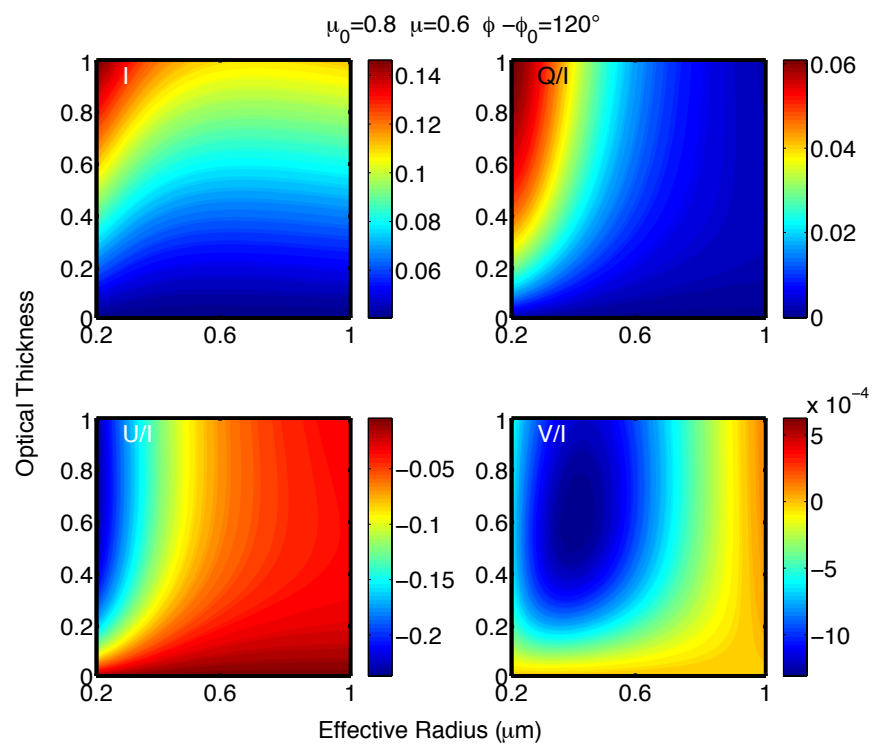


**Fig. 44** Similar as Fig. 40, except the viewing angle has  $\phi-\phi_0=120^\circ$ .

$$\frac{|I_c - I_s|}{I_s} \leq 0.02 \quad (4.1)$$

and the polarization criteria:

$$\frac{1}{2}(|q_c - q_s| + |u_c - u_s|) \leq 0.001 \quad (4.2)$$

Here  $I_s, q_s, u_s$  are Stokes parameters of the standard model where  $q_s = \frac{Q_s}{I_s}$  and  $u_s = \frac{U_s}{I_s}$ .

$I_c, q_c, u_c$  are the corresponding Stokes parameters of candidate models. Both intensity and polarization cannot determine the optical thickness and effective radius over the candidate set. However, due to the different sensitivity patterns of the intensity and polarization, two “unknown” quantities can be determined if criteria 4.1 and 4.2 are applied simultaneously. The aerosol optical thickness and the effective radius are perfectly retrieved in Fig. 45. The absolute error is less than 0.02 for the aerosol optical thickness retrieval results and  $0.02\mu\text{m}$  for effective radius.

Figs. 46 shows similar retrieval results. The same standard models are applied. The viewing angle is modified as  $\phi - \phi_0 = 60^\circ$ . The superposition of the criteria also shows good retrieval results, as both aerosol optical thickness and effective radius can be well determined. However, the error for retrieval result is relatively large for the case  $r_{\text{eff}}=0.9$ .

Fig. 47 plots the reflectance Stokes parameters versus the aerosol optical thickness and the real part of the refractive index. The geometry of illumination and observation is set as the same as previous studies (i.e.,  $\mu = 0.8, \mu_0 = 0.6, \phi - \phi_0 = 0^\circ$ ). For large aerosol optical thickness ( $\tau \geq 0.2$ ), the reflectance polarization is sensitive to the refractive index change. This sensitivity is weakened for small aerosol optical thickness.

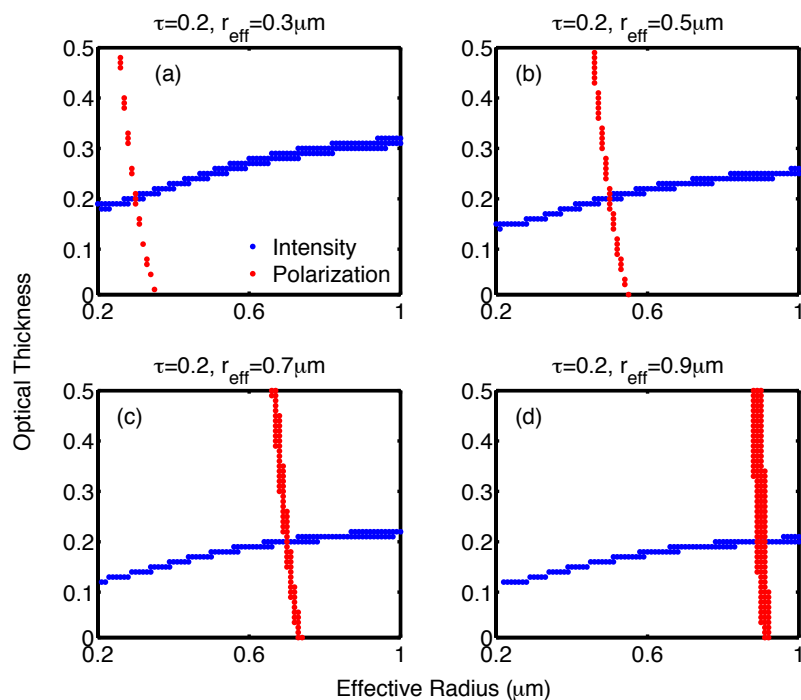
The reflectance intensity is more sensitive to the change of the optical thickness than of the refractive index (real part).

Fig. 48 is similar as Fig. 47 except the change of viewing angle ( $\phi - \phi_0 = 120^\circ$  in this case). The sensitivity pattern of reflectance intensity for this case is similar as the previous case. However, the sensitivity pattern of the polarization is no longer very sensitive to refractive index change when  $\tau \leq 0.4$ . This optical thickness threshold value is larger than the previous case. This fact may affect the retrieval result for low-aerosol optical thickness cases.

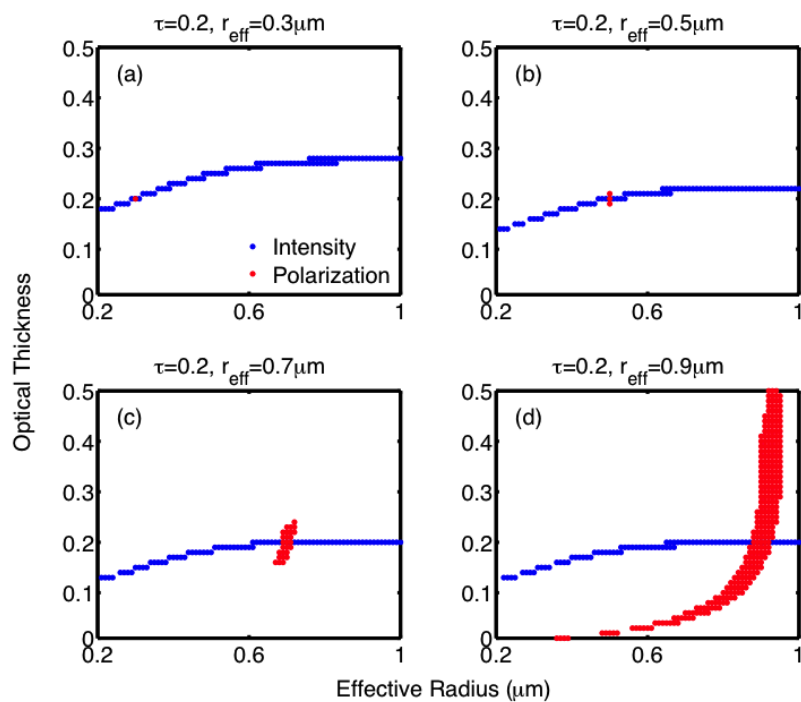
Fig. 49 shows the optical thickness and refractive index (real part) retrieval results for the case shown in Fig. 47. Four standard models with  $\tau=0.2$  and  $m_r=$  (a) 1.35 (b) 1.45 (c) 1.50 and (d) 1.55 are selected in this study. A combination of the intensity criteria 4.1 and polarization criteria 4.2 is applied. The retrievals show good results.

Fig. 50 is similar as Fig. 49 except the viewing angle is modified as  $\phi - \phi_0 = 120^\circ$ . The simulation results shown in Fig. 47 are equipped in this retrieval study as they have the same illumination-observation geometry. Criteria (3.1) and (3.2) are combined. The retrievals well determined both refractive index and aerosol optical thickness except the small  $m_r$  cases (shown in upper-left panel).

Fig. 51 is similar as Fig. 50. Four standard models in this study are selected as  $\tau=0.4$  and  $m_r=$  (a) 1.35 (b) 1.45 (c) 1.50 and (d) 1.55. Compared with Fig. 48, the retrieval procedure provides a better resolution for high aerosol optical thickness cases. This result is predicted in the discussion of Fig. 47.

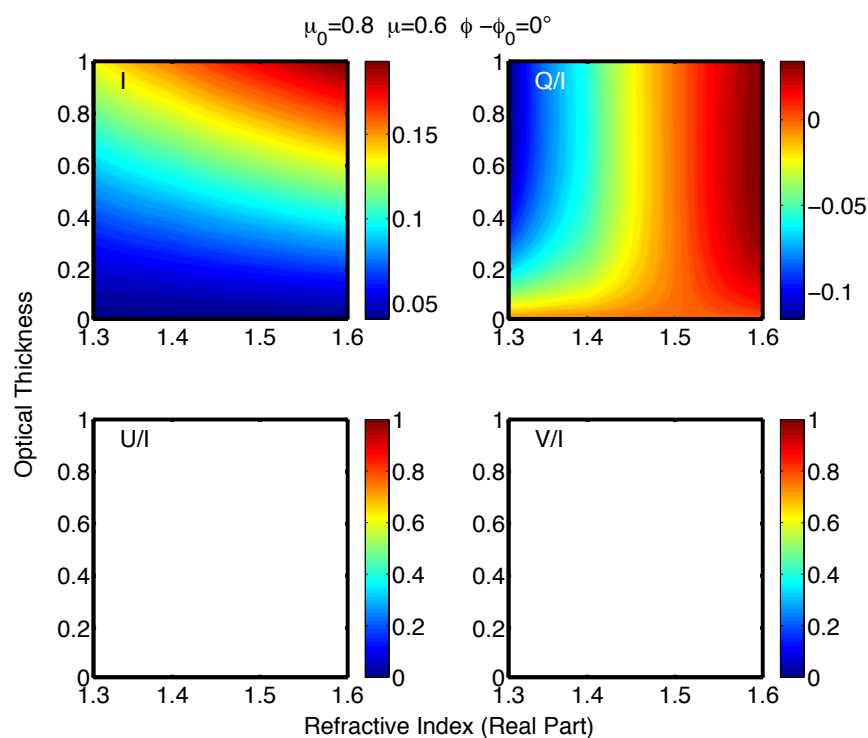


**Fig. 45** Modeling of aerosol optical thickness and effective radius retrievals using both intensity and polarization criteria. Four standard models with  $\tau=0.2$  and  $r_{\text{eff}}=$  (a)  $0.3\mu\text{m}$  (b)  $0.5\mu\text{m}$  (c)  $0.7\mu\text{m}$  and (d)  $0.9\mu\text{m}$ . The aerosol refractive index is assumed to be known beforehand ( $m=1.53+i0.008$ ). The illumination and viewing geometry are specified as  $\mu_0=0.8$ ,  $\mu=0.6$  and  $\phi-\phi_0=0^\circ$ .

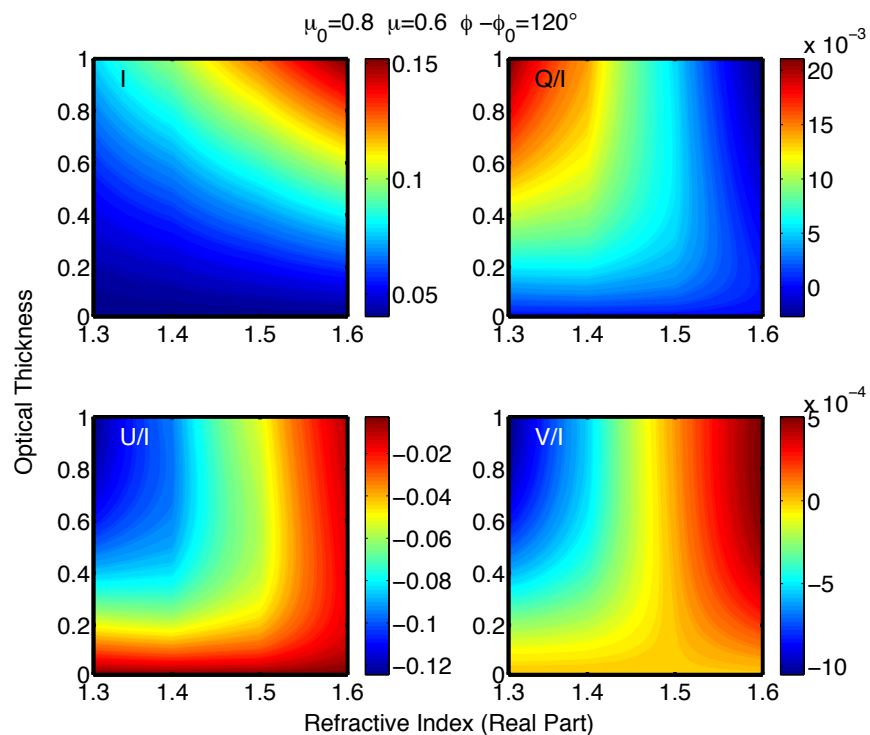


**Fig. 46** Similar as Fig. 44 except for  $\phi-\phi_0=60^\circ$ .

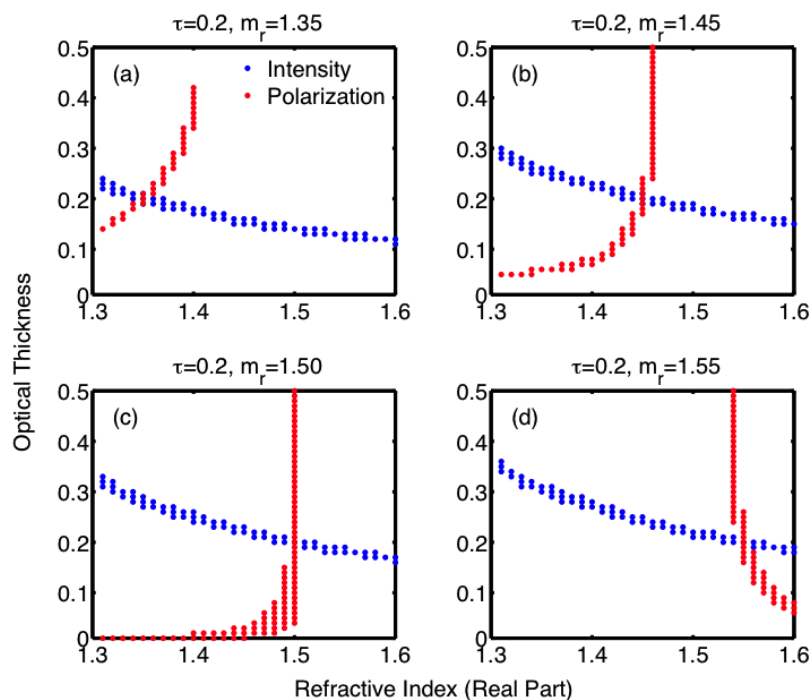
Figs. 52 and 53 tests the sensitivity of the reflectance versus aerosol optical thickness and the refractive index (imaginary part). The illumination and observation geometry is still the same ( $\mu = 0.8, \mu_0 = 0.6, \phi - \phi_0 = 0^\circ$  for Fig. 52 and  $\mu = 0.8, \mu_0 = 0.6, \phi - \phi_0 = 120^\circ$  for Fig. 53). The imaginary part of the refractive index ranges from 0.001 to 0.1 with an equal-logarithmic step. Thus the step between sampling points is larger for larger  $m_i$ . The intensity and polarization again show different sensitivity pattern versus the aerosol optical thickness and the imaginary part of refractive index. This advantage make the retrieval procedure aforementioned available.



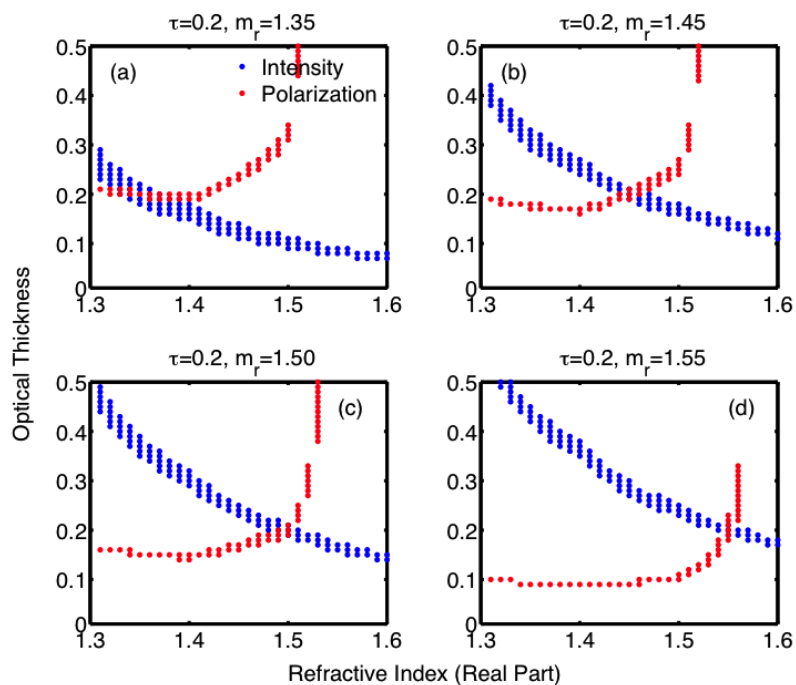
**Fig. 47** The Stokes parameter of the reflectance of an atmosphere layer versus the aerosol optical thickness and refractive index (real part) of the aerosol model. The incident zenith angle is  $\mu_0 = 0.8$ , the viewing angle is  $\mu = 0.6$  and  $\phi - \phi_0 = 0^\circ$ .



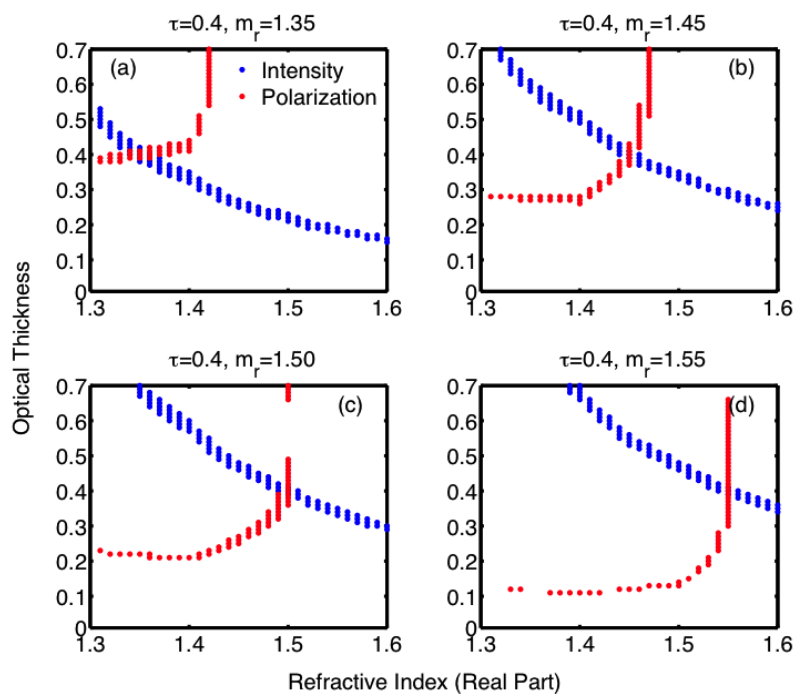
**Fig. 48** Similar as Fig. 46, except the viewing angle has  $\phi - \phi_0 = 120^\circ$ .



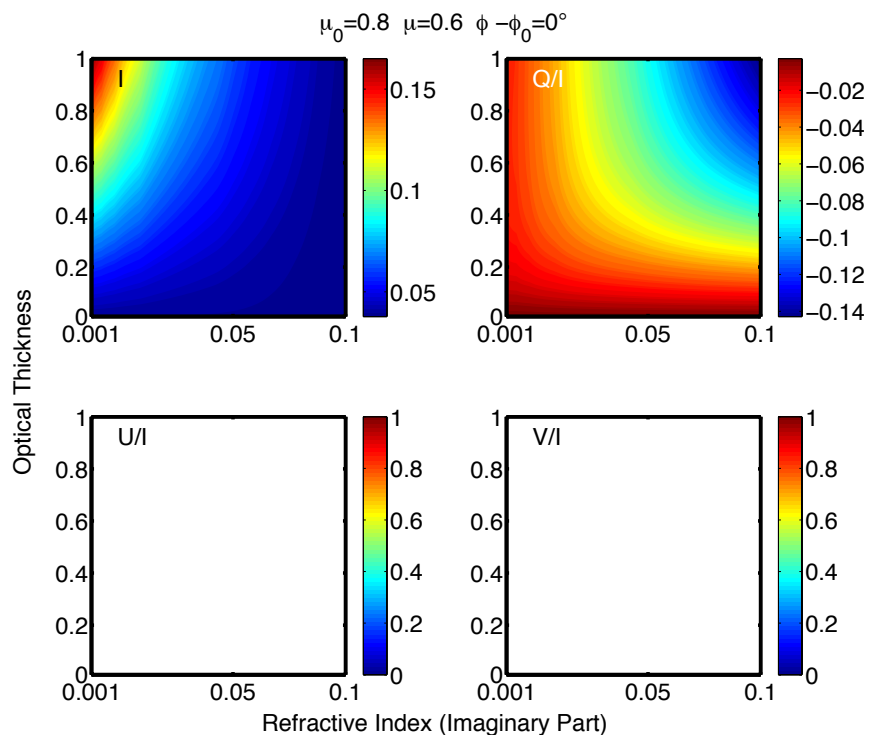
**Fig. 49** Modeling of aerosol optical thickness and refractive index (real part) retrievals using both intensity and polarization criteria. Four standard models with  $\tau=0.2$  and  $m_r=$  (a) 1.35 (b) 1.45 (c) 1.50 and (d) 1.55 are selected. The aerosol refractive index is assumed to be known beforehand ( $m=1.53+i0.008$ ). The illumination and viewing geometry are specified as  $\mu_0=0.8$ ,  $\mu=0.6$  and  $\phi - \phi_0=0^\circ$ .



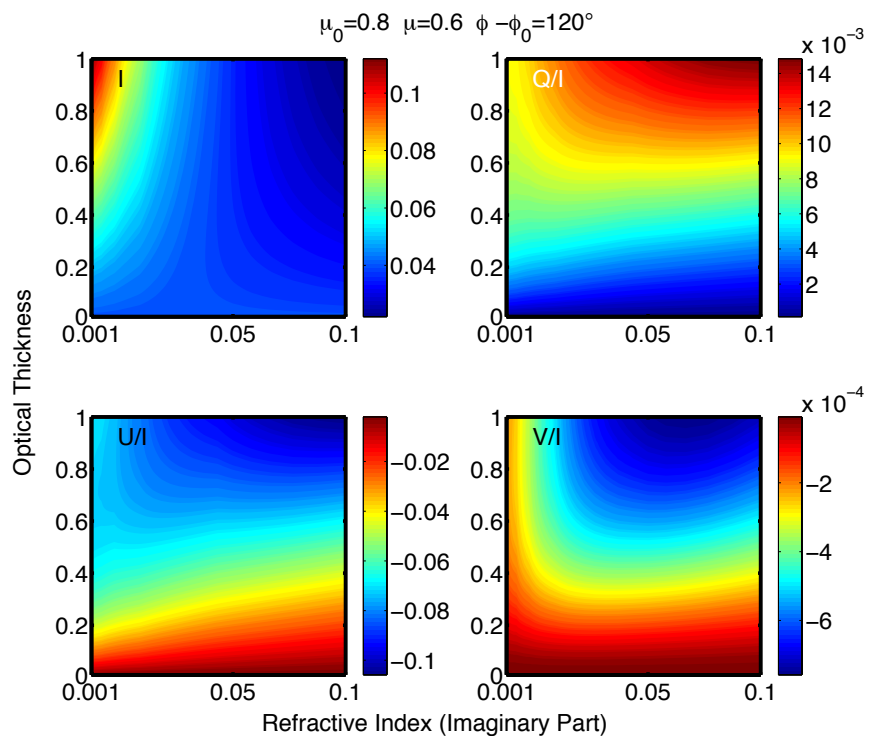
**Fig. 50** Similar as Fig. 48 except for  $\phi-\phi_0=60^\circ$ .



**Fig. 51** Similar as Fig. 48 except for aerosol optical thickness of standard models  $\tau=0.4$ .

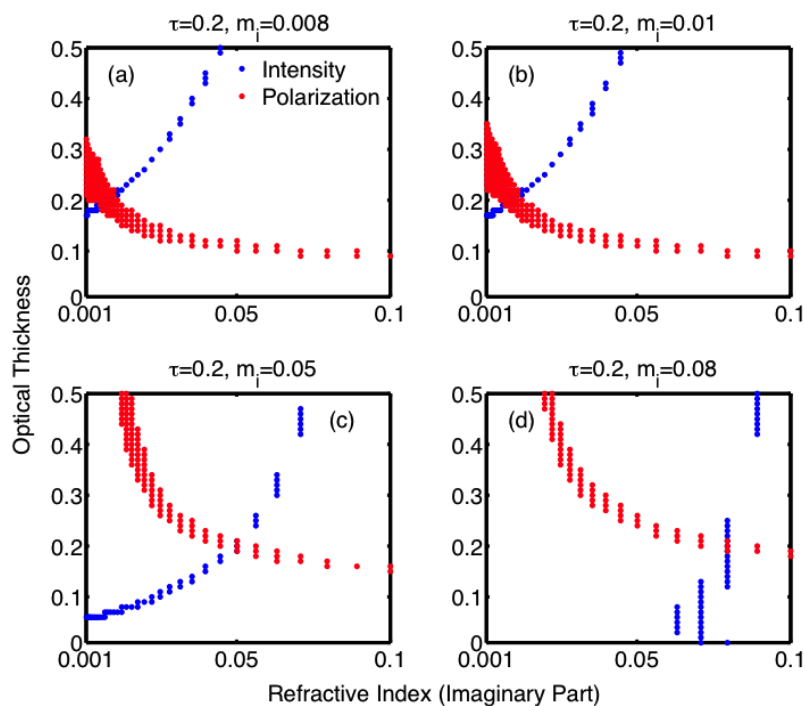


**Fig. 52** The Stokes parameter of the reflectance of an atmosphere layer versus the aerosol optical thickness and refractive index (real part) of the aerosol model. The incident zenith angle is  $\mu_0=0.8$ , the viewing angle is  $\mu=0.6$  and  $\phi-\phi_0=0^\circ$ .

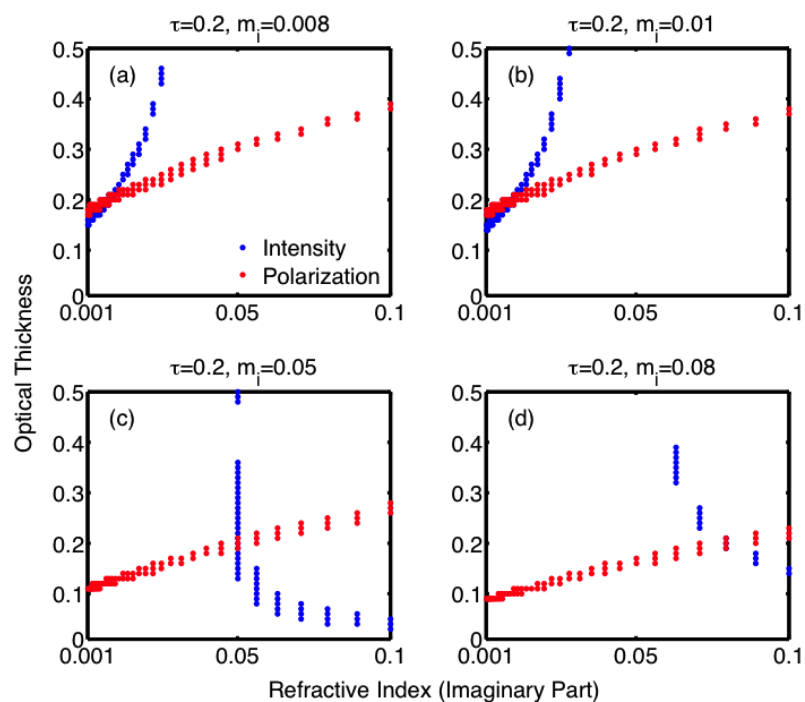


**Fig. 53** Similar as Fig. 51 except for  $\phi-\phi_0=120^\circ$ .





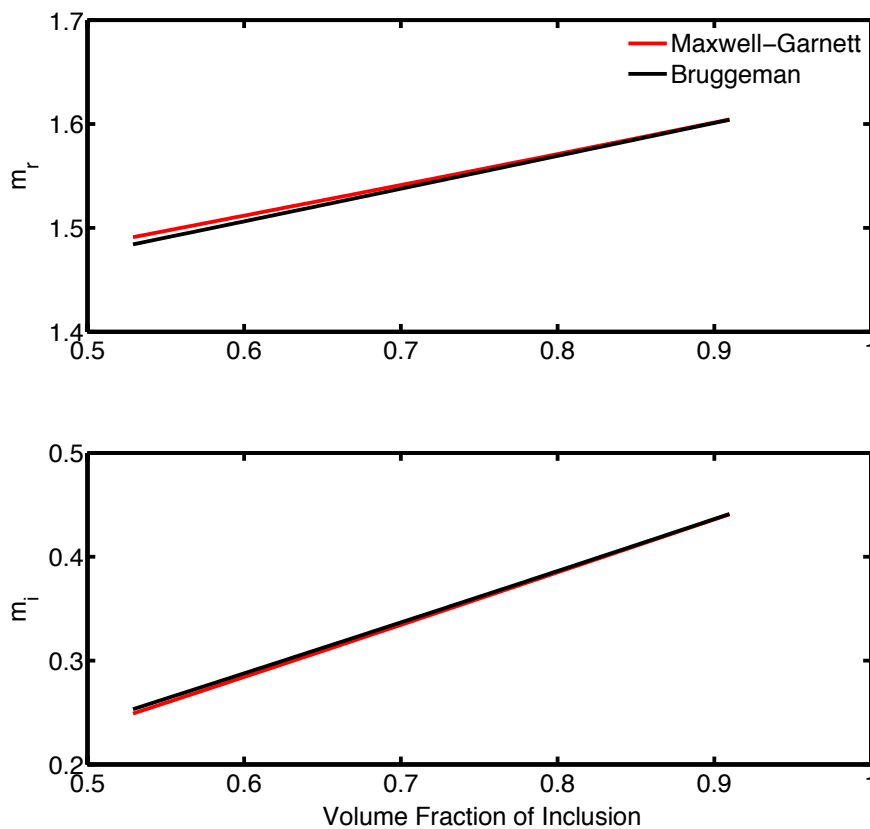
**Fig. 54** Modeling of aerosol optical thickness and refractive index (imaginary part) retrievals using both intensity and polarization criteria. Four standard models with  $\tau=0.2$  and  $m_i$ = (a) 0.008 (b) 0.01 (c) 0.05 and (d) 0.08 are selected. The illumination and observation geometry are specified as  $\mu_0=0.8$ ,  $\mu=0.6$  and  $\phi-\phi_0=0^\circ$ .



**Fig. 55** Similar as Fig. 53 except for  $\phi-\phi_0=120^\circ$ .

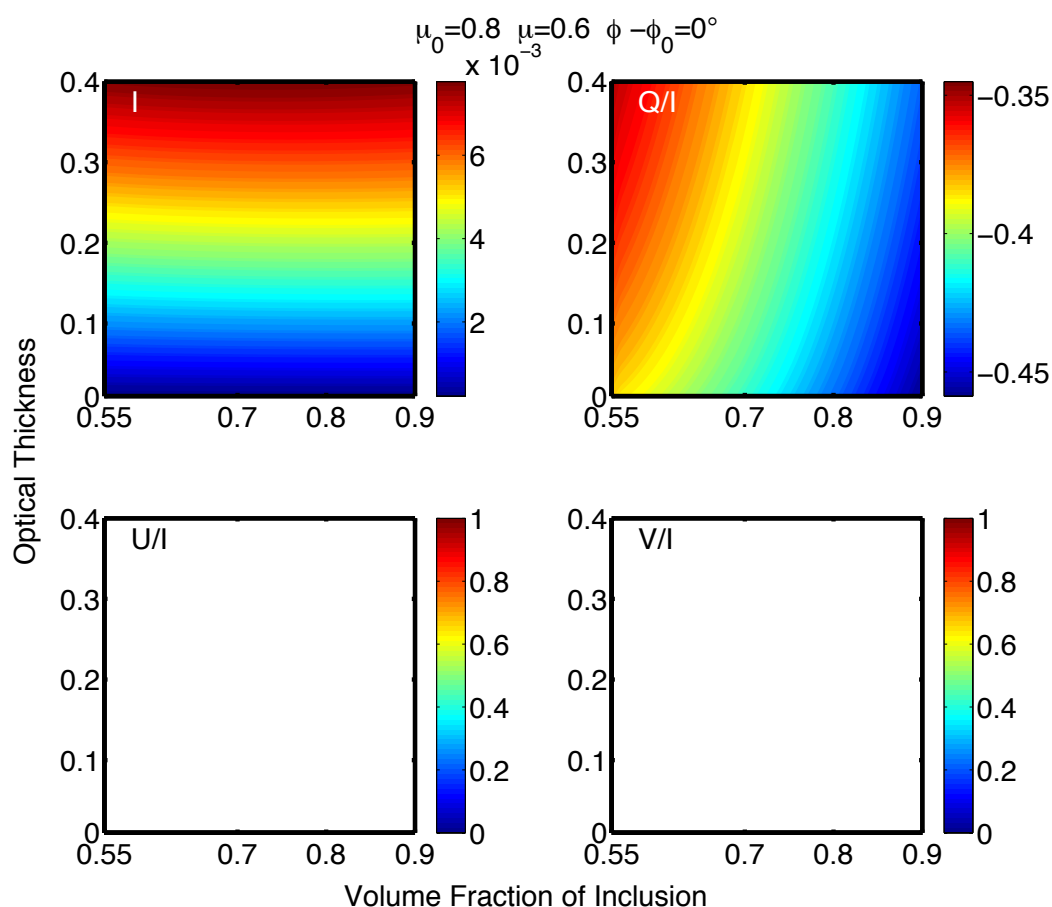
The trial retrieval results are shown in Figs. 54 and 55, respectively. Four standard models with  $\tau=0.2$  and  $m_i=$  (a) 0.008 (b) 0.01 (c) 0.05 and (d) 0.08 are selected. The resolution is relatively higher for large  $m_i$ .

Fig. 56 shows the relation effective refractive index and the volume fraction of the inclusion. The inclusion is supposed to be a spherical soot with refractive index  $m=1.6327+i0.487$ . The refractive index of water coat is set as  $m=1.32+i0$  under wavelength of  $0.875\mu\text{m}$ . The model is shown in Fig. 34. Both Maxwell-Garnett and Bruggeman's theories are used.



**Fig.56** The relation between effective refractive index and the volume fraction of the inclusion. The inclusion is supposed to be a spherical soot with refractive index  $m=1.6327+i0.487$ . The refractive index of water coat is  $m=1.32+i0$ .

Fig. 57 presents the reflection of an atmosphere layer containing water coated aerosol models. In this study, the effective refractive index is defined according to Bruggeman's theory. The illumination and observation geometry is set as  $\mu = 0.8, \mu_0 = 0.6, \phi - \phi_0 = 0^\circ$ . The upper-left panel shows that the intensity of reflection is insensitive to the volume fraction of the soot. Luckily the polarization shows different sensitivity pattern. Therefore the retrieval procedure is again useful in this case.



**Fig. 57** The Stokes parameter of the reflectance of an atmosphere layer versus the aerosol optical thickness and volume fraction of the inclusion in the aerosol model. The incident zenith angle is  $\mu_0 = 0.8$ , the viewing angle is  $\mu = 0.6$  and  $\phi - \phi_0 = 0^\circ$ .

#### D. SUMMARY

In this study, we have used numerically accurate solutions of the vector radiative transfer theory for tri-axial ellipsoidal models to theoretically simulate several types of retrievals over the ocean. The newly derived database for tri-axial ellipsoidal aerosol models is applied and tested. Figs 36-39 compare the radiance effect of spherical and tri-axial ellipsoidal models, which demonstrated that the ellipsoidal models help provide more variability for aerosol retrieval. The reflectance, including the intensity and state of polarization, are derived and shown in the next part of this study. The reflectance sensitivity patterns versus the aerosol optical thickness, effective index and the refractive index are studied. Based on the Stokes parameter of the reflectance, several types of retrieval attempts are done consequently. All the retrieval attempts rely on both intensity and polarization information of the reflectance. The retrieval attempts generally give good results except for a few cases. The retrieval results provide a possibility of utilizing the tri-axial ellipsoidal models to atmospheric studies.

## CHAPTER V

### CONCLUSION

In this thesis, we have studied the light scattering problems for arbitrarily shaped particles. Three models, including spheres, cylinders and hexagonal columns are taken into consideration. The phase matrix and scattering cross sections of those models are derived via a combination of the T-matrix ansatz and the null-field method.

In order to improve the time efficiency for modeling single-scattering properties of aerosol models, we have built a database. The second part in this thesis presents the details of this database, including the model selection, methodology and some demo results. The database is available online. It is ready to be used in radiative transfer applications.

The third part of this thesis puts the database results into radiative transfer models. In this part, a polarized adding-doubling radiative transfer model is applied. The tri-axial ellipsoidal models, as previously discussed, are applied to model the aerosols in atmospheric layer. A further sensitivity study is made on the aerosol optical thickness, effective radius and refractive index. The intensity and polarization state of the reflection show different sensitivity patterns versus the aerosol optical thickness, aerosol effective radius and the refractive index of the models. This property can be applied into the retrieval procedure. Most trial retrieves in this thesis return good results. Furthermore, based on the Bruggeman's theory, the water-coated soot is studied by the end of this thesis. The applicability of the new database is thus verified.

## REFERENCES

- Bashkatov A. N., & Genina E. A. (2002). Water refractive index in dependence on temperature and wavelength: a simple approximation, Saratov Fall Meeting 2002: Optical Technologies in Biophysics and Medicine IV.
- Bates R. H. T. (1968). Modal expansions for electromagnetic scattering from perfectly conducting cylinders of arbitrary cross-sections, *Proc. IEE*, 115, 1443-1445.
- Bi L., Yang P., & Kattawar G. W. (2009). Single-scattering properties of triaxial ellipsoidal particles for a size parameter range from the Rayleigh to geometric-optics regimes, *Applied Optics*, 48(1), 114-126.
- Bohren C.F, & Huffman D.R. (1983). *Absorption and Scattering of Light by Small Particles*. New York: Wiley-Interscience.
- Bruggeman D. A. G. (1935). Berechnung verschiedener physikalischer Konstanten von heterogenen Substanzen, *Annalen der Physik*, 5 Folge, Band 24.
- Chang H., & Charalampopoulos T. (1990). Determination of the wavelength dependence of refractive indices of flame soot, *Proc R. Soc.* 430, 577-591.
- Chuang P. Y., Duvall R. M., & Bae M. S. (2003). Observations of elemental carbon and absorption during ACE-Asia and implications for aerosol radiative properties and climate forcing. *Journal of Geophysical research*, 108, 8634-8646.
- Chylek P., & Coakley J. (1974). Aerosols and climate, *Science* 183, 75.
- Curtis D. B., Meland B., & Aycibin, (2008). A laboratory investigation of light scattering from representative components of mineral dust aerosol at a wavelength of 550 nm, *Journal of Geophysical Research*, 113(D08210), 1-15.
- Deuzé J. L., Gouloub P., & Herman M. (2000). Estimate of the aerosol properties over the ocean with POLDER, *Journal of Geophysical Research*, 105(D12), 15329-15346.
- Draine B. T, & Flatau P. J. (1994). Discrete-dipole approximation for scattering calculations, *Journal of the Optical Society of America A*, 11(4), 1491-1499.

- Dubovik O. (2004). Optimization of numerical inversion in photopolarimetric remote sensing, *Photopolarimetry in Remote Sensing*, 161(1), 65-106.
- Dubovik O., & King M. (2000). A flexible inversion algorithm for retrieval of aerosol optical properties from Sun and sky radiance measurements, *Journal of Geophysical Research-Atmospheres*, 105(D16), 20673-20696.
- Dubovik O., Sinyuk A., & Lapyonok T. (2006). Application of spheroid models to account for aerosol particle nonsphericity in remote sensing of desert dust, *Journal of Geophysical Research*, 111(D11208), 1-34.
- Feng Q., Yang P., & Kattawar G. W. (2009). Effects of particle nonsphericity and radiation polarization on retrieving dust properties from satellite observations, *Journal of Aerosol Science*, 40, 776-789.
- Forster P, Ramaswamy V, & Artaxo P, et al., editors. (2007) Climate change 2007: the physical science basis. *Contribution of Working Group I to the Fourth Assessment Report of the Intergovernmental Panel on Climate Change*, New York: Cambridge University Press.
- Garnett, J. C. M. (1904). Colours in metal glasses and in metallic films. *Philos T R Sco Lond*, 203:385-420.
- Garnett, J. C. M. (1906). Colours in metal glasses, in metallic solutions - II. *Philos T R Sco Lond*, 205:237-288.
- Haywood J, Francis P, & Osborne S. (2003). Radiative properties and direct radiative effect of Saharan dust measured by the C-130 aircraft during SHADE: 1. Solar spectrum, *Journal of Geophysical Research* 108(D18), SAH4.1-16.
- Henning Th., Il'in, V. B, & Krivova, N. A. (1999). WWW database of optical constants for astronomy, *Astronomy & Astrophysics Supplement Series*, 136, 405-406.
- Hess M., Koepke P., & Schult I. (1998). Optical Properties of Aerosols and Clouds: The Software Package OPAC, *Bulletin of the American Meteorological Society*, 79(5), 831-844.

- Heymsfield A. J., & Knollenberg R. G. (1972). "Properties of cirrus generating cells," *J. Atmos. Sci.* 29, 1358–1366.
- Holben B. N., Eck T. F., & Slutsker I. (1998). AERONET - A federated instrument network and data archive for aerosol characterization, *Remote Sensing of Environment*. 66, 1-16.
- Kahn R., West R., & McDonald D. (1997). Sensitivity of multi-angle remote sensing observations to aerosol sphericity, *Journal of Geophysical Research*, 102(D14), 16861-16870.
- Kaufman Y. J., Tanré D., & Boucher O. (2002). A satellite view of aerosols in the climate system, *Nature*, 419(6903), 215-223.
- King M., Byrne D., & Herman B.. (1978). Aerosol Size Distributions Obtained by Inversions of Spectral Optical Depth Measurements, *Journal of the Atmospheric Sciences*, 35(11), 2153-2167.
- King M. D., Kaufman Y. J., & Tanré D. (1999). Remote sensing of tropospheric aerosols from space: Past, present, and future, *Bulletin of the American Meteorological Society*, 80(11), 2229-2259.
- Kokhanovsky A. (2003). Optical properties of irregularly shaped particles, *Journal of Physics D: Applied Physics*, 36, 915-923.
- Levoni C, Cervino M., & Guzzi R. (1997). Atmospheric aerosol optical properties: a database of radiative characteristics for different components and classes, *Applied Optics*, 36(30), 8031-8041.
- Levy R., Remer L., & Mattoo S. (2007). Second-generation operational algorithm: Retrieval of aerosol properties over land from Inversion of Moderate Resolution Imaging Spectroradiometer spectral reflectance, *Journal of Geophysical Research*, 112(D13211), 1-21.
- Liou K. N, *An Introduction to Atmospheric Radiation*, 2<sup>nd</sup> ed., Academic Press, San Diego, 257-347.



- Liu G, (2008). A database of microwave single-scattering properties for nonspherical ice particles, *B Am Meteorol Soc*, 89(10), 1563-1570.
- Marchand A., Nadal F., & Perry G. (2001). Remote sensing of aerosols over land surfaces from POLDER-ADEOS-1 polarized measurements, *Journal of Geophysical Research*, 106(D5), 4913-4926.
- Mie G. (1908). Beitrage zur Optik truber Medien, speziell kolloidaler Metallosungen, *Annalen der Physik*. 330(3), 377-445.
- Mishchenko M.I, Hovenier J.W., & Travis L.D. (2000). *Light Scattering by Nonspherical Particles: Theory, Measurements and Applications*, San Diego: Academic, 197-220.
- Mishchenko, M.I, Travis L.D., & Lacis A. (2003). *Radiative transfer: Scattering*. In *Encyclopedia of Atmospheric Sciences*. Holton J.R., Pyle J., Curry J.A., Eds. Academic Press, 1882-1891.
- Mishchenko M.I, Travis L.D., & Mackowski D.W. (1996). "T-matrix computations of light scattering by nonspherical particles: a review," *Journal of Quantitative Spectroscopy & Radiative Transfer* 55, 535–575.
- Mishchenko, M. I, Travis L. D, & Rossow W. B. (1997). Modeling phase functions for dustlike tropospheric aerosols using a mixture of randomly oriented polydisperse spheroids. *Journal of Geophysical Research*. 102(D14), 16831-16847.
- Morse P.M. & Feshbach H. (1953). *Methods of Theoretical Physics*, New York: McGraw-Hill, 1065.
- Muñoz O., & Volten H. (2006). *Experimental light scattering matrices from the Amsterdam light scattering database*. In: Kokhanovsky A., editor. *Light scattering reviews*. Berlin: Springer.
- Muñoz O., Volten H., & Hovenier J. W. (2006). Experimental and computational study of light scattering by irregular particles with extreme refractive indices: hematite and rutile, *Astronomy and Astrophysics*, 446(2), 525-535.

- Nakajima T. (1996). Use of sky brightness measurements from ground for remote sensing of particulate polydispersions, *Applied Optics*, 35, 2672-2686.
- Nousiainen T. (2009). Optical modeling of mineral dust particles: A review, *Journal of Quantitative Spectroscopy & Radiative Transfer*, 110.
- Nousiainen T, Muinonen K., & Raisanen P. (2003). Scattering of light by large Saharan dust particles in a modified ray optics approximation, *Journal of Geophysical Research*, 108(D1), 4025-4042.
- Nussenzveig H. M. (1992). *Diffraction Effects in Semiclassical Scattering* (Cambridge University)
- Penttila A., Zubko E., & Lumme K. (2007). Comparison between discrete dipole implementations and exact techniques, *Journal of Quantitative Spectroscopy & Radiative Transfer*, 106(1-3), 417-436.
- Peterson B., & Strom S. (1974). T-matrix formulation of electromagnetic scattering from multilayered scatterers, *Physics Review* 10(8), 2670-2684.
- Peterson B., & Strom S. (1975), Matrix formulation of acoustic scattering from multilayered scatterers, *Journal of the Acoustical Society of America*. 57(1), 2-13.
- Purcell E. M., & Pennypacker C. R. (1973). Scattering and adsorption of light by nonspherical dielectric grains, *Astrophysical Journal*. 186, 705-714.
- Ramanathan V, Crutzen P. J., & Kiehl J. T. (2001). Aerosols, climate, and the hydrological cycle, *Science*, 294(5549), 2119-2124.
- Reid E. A., Reid J. S., & Meier M. M. (2003a). Characterization of African dust transported to Puerto Rico by individual particle and size segregated bulk analysis, *Journal of Geophysical Research*, 108(D19), PRD7.1-22.
- Reid J. S, Kinney J. E., & Westphal D. L. (2003b). Analysis of measurements of Saharan dust by airborne and ground-based remote sensing methods during the Puerto Rico Dust Experiment (PRIDE), *Journal of Geophysical Research*, 108(D19), 8586-8612.

- Shell K. M., & Somerville R. C. J. (2007). Direct radiative effect of mineral dust and volcanic aerosols in a simple aerosol climate model. *Journal of Geophysical Research*, 112(D03205), 1-15.
- Sokolik, I. N., & Toon O. B. (1998). Modeling the radiative properties of mineral aerosols for climate studies and remote sensing applications. *Journal of Aerosol Science*. 29, 8813-8826.
- Sokolik I. N., & Toon O. B. (1999). Incorporation of mineralogical composition into models of the radiative properties of mineral aerosol from UV to IR wavelengths, *Journal of Geophysical Research*, 104(D8), 9423-9444.
- Sokolik I, Winker D, & Bergametti G. (2001). Introduction to special section: outstanding problems in quantifying the radiative impacts of mineral dust. *Journal of Geophysical Research*, 106(D16), 18015-18027.
- Sun, W., Fu Q. & Chen Z. (1999). "Finite-difference time-domain solution of light scattering by dielectric particles with perfectly matched layer absorbing boundary conditions," *Applied Optics* 38, 3141-3151.
- Tegen, I., & Lacis A. A. (1996). Modeling of particle size distribution and its influence on the radiative properties of mineral dust aerosol. *Journal of Geophysical Research*, 101(D14), 19237-19244.
- Twomey S. (1977). *Introduction to the Mathematics of Inversion in Remote Sensing and Indirect Measurements*, Elsevier.
- Verhaege C., Shcherbakov V., & Personne P. (2009). Retrieval of complex refractive index and size distribution of spherical particles from Dual-Polarization Polar Nephelometer data, *Journal of Quantitative Spectroscopy and Radiative Transfer*, 110(14-16), 1690-1697.
- Volten H, Muñoz O, & Brucato J. R. (2006). Scattering matrices and reflectance spectra of forsterite particles with different size distributions. *Journal of Quantitative Spectroscopy and Radiative Transfer*, 100(1-3), 429-436.

- Volten H., Muñoz O., & de Haan J. F. (2001). Scattering matrices of mineral aerosol particles at 441.6 nm and 632.8 nm. *Journal of Geophysical Research*, 106(D15), 17375-17401.
- Warren J., Barrett R., Dodson A., Watts L., & Zolensky M., editors. (1994). Cosmic dust catalog, vol. 14. Houston: NASA, Johnson Space Center; 568.
- Waterman P. C. (1965). Matrix formulation of Electromagnetic scattering, *IEEE, Proceedings*, 53(8), 805-812.
- Waterman P.C. (1969a). Scattering by dielectric obstacles, *Alta Freq*, 38, 348-352.
- Waterman P.C.(1969b). New formulation of acoustic scattering, *J. Acoust. Soc. Am.*, 45(6), 1417-1429.
- Waterman P.C. (1973). Numerical solution of electromagnetic scattering problems, in *Computer Techniques for Electromagnetics*, ed. By R. Mittra, Oxford: Pergamon.
- West R. A., Doose L. R., & Eibl A. M. (1997). Laboratory measurements of mineral dust scattering phase function and linear polarization, *Journal of Geophysical Research*, 102(D14), 16871-16881.
- Yang P., Feng Q., & Hong G. (2007). Modeling of the scattering and radiative properties of nonspherical dust-like aerosols. *Journal of Aerosol Science*, 38(10), 995-1014.
- Yang, P., & Liou K. N., (1996a). Finite-difference time domain method for light scattering by small ice crystals in three-dimensional space, *Journal of Optical Society America*, A13(10), 2072-2085
- Yang P., & Liou K. N. (1996b). Geometric-optics integral-equation method for light scattering by nonspherical ice crystals, *Applied Optics*. 35.
- Yang P., & Liou K. N. (2000). Mishchenko M.I. and Gao B. C., Efficient finite-difference time domain scheme for light scattering by dielectric particles: application to aerosols, *Applied Optics*, 39(21), 3727-3737.
- Yee K., (1966). Numerical solution of initial boundary value problems involving Maxwell's equations in isotropic media. *Antennas and Propagation, IEEE Transactions*, A14(8), 302-308.

Yurkin M. A., & Hoekstra A. G. (2009). User Manual for the Discrete Dipole Approximation Code ADDA v. 0.79,

[http://a-dda.googlecode.com/svn/tags/rel\\_0\\_79/doc/manual.pdf](http://a-dda.googlecode.com/svn/tags/rel_0_79/doc/manual.pdf).

Zeng X. C., Bergman D. J., & Hui P. M. (1988), Effective-medium theory for weakly nonlinear composites, *Physical Review B.*, 38(15), 10970-10973.

## VITA

Zhaokai Meng received his Bachelor of Science degree in physics from Wuhan University in 2008. He entered Department of Physics and Astronomy at Texas A&M University in August 2008 and received his Master of Science degree in December 2010. His research interests include light scattering by arbitrarily shaped particles and its application in radiative transfer techniques.

Mr. Meng may be reached at 1501 Holleman Dr. APT 108, College Station, TX, 77840, USA. He may also be reached via his permanent address: Che Cheng Xi Lu #56, Shiyan, Hubei, 442000, China. His email is [zhaokai.meng@gmail.com](mailto:zhaokai.meng@gmail.com).